Doctoral Dissertation

Multiscale Characterization of Geotextile-Reinforced Granular Soil

CHENG HONGYANG

Graduate School for International Development and Cooperation
Hiroshima University

September 2016

Multiscale Characterization of Geotextile-Reinforced Granular Soil

D132535

CHENG HONGYANG

A Dissertation Submitted to
the Graduate School for International Development and Cooperation
of Hiroshima University in Partial Fulfillment
of the Requirement for the Degree of
Doctor of Engineering

September 2016

We hereby recommend that the dissertation by Mr. CHENG HONGYANG entitled "Multiscale Characterization of Geotextile-Reinforced Granular Soil" be accepted in partial fulfillment of the requirements for the degree of DOCTOR OF ENGINEERING).

Committee on Final Examination:

H. Yamamoto.

YAMAMOTO Haruyuki, Professor

Chairperson

Takao Yamashita

YAMASHITA Takao, Professor

Yasushi Higo

HIGO Yasushi, Professor

Koji Ichii

ICHII Koji, Associate Professor

Yukio Fujimoto

FUJIMOTO Yukio, Professor

Date: 22. July 2016

Approved: Takuya Baba

Baba Takuya, Professor
Dean

Date: September 2, 2016

Graduate School for International Development and Cooperation
Hiroshima University

To my beloved parents and grandparents.

To Xinyan Fan.

Acknowledgements

I would like to express my sincerest gratitude to my supervisor Professor Haruyuki Yamamoto for his persistent mentoring and encouragement. I cherish the memories of those countless discussions with him which I believe will continuously influence my future career as a university professor.

I wish to extend my gratitude to Dr Klaus Thonei at the University of Newcastle, who has not only shown me the versatility of the open-source DEM package Yade, but the efficient and joyful ways of doing research as well. I am particularly grateful for his careful revision and instructive suggestions on my papers and presentations. My gratitude also goes to Assistant Professor Takayuki Shuku at Okayama University and Dr Ning Guo at the Hong Kong University of Science and Technology for their generosity in sharing the computer codes and their collaborative efforts in my papers.

I thank Professor Koji Ichii, my external committee member, for his careful examination of the thesis and constructive comments that improved the quality of the thesis. I enjoyed his lectures of geotechnical earthquake engineering and those international seminars he kindly organized, from which I established long-term friendship with talented Japanese researchers. I would like also to express my acknowledgment to my other committee members Professor Takao Yamashita, Professor Yasushi Higo and Professor Yukio Fujimoto for their valuable comments and suggestions on the thesis.

I have my indebtedness to Professor Wei Li at Shenyang Jianzhu University, who taught me soil mechanics and supervised my Bachelor thesis during my undergraduate study and kindly gave me his recommendation which led to the successful application of the Japanese government (MEXT) scholarship.

I'm also indebted to my laboratory colleagues: Dr Lingyu Meng, Dr Yang Wu, Dr He Huang, Dr Shaohong Jin, as well as many exceptional friends in different fields: Associate Professor Biying Yu, Dr Ying Jiang, Dr Zhe Gong, Dr Yubing Xiong, Dr Da Teng and Dr Anqi Huang. It is only through constant communication and discussion with them that this thesis is made possible. I wish to gratefully acknowledge my other friends and colleagues at Hiroshima University who made this journey enjoyable.

Abstract

Geosynthetic-reinforced soils are heterogeneous and discontinuous geomaterials that can be designed with great flexibility. For environmental and economical reasons, the application of geosynthetic reinforcements in the construction of infrastructures is becoming prevalent, along with the increase of the diversity in reinforcement forms, e.g. discrete fiber, planar layer, cellular encasement, to name a few. Despite high improvement on the stiffness and strength, the interactions between granular particles and geosynthetic inclusions complicate the stress history, deformation pattern and fabric characteristics in the reinforced soils, posing formidable challenges to the predictive models of geosynthetic-reinforced soils. Considering the 'discrete' nature of granular soils, this thesis aims to obtain a better understanding of the behavior of geosynthetic-reinforced granular soil via multiscale characterization and modeling of soil–geosynthetic interactions, and thence develop analytical solutions for this complex geomaterial for practical usage.

The Discrete Element Method (DEM) is utilized to provide a cross-scale interpretation of the micromechanics in the granular soil with different forms of geosynthetic reinforcement. The sequential data assimilation based on recursive Bayesian estimation is employed to calibrate the mesoscale response of the DEM models of Toyoura sand. With the assumptions derived from the newly obtained understanding, a close-form elastoplastic solution is proposed for geotextile-wrapped soil under compression. In order to solve general soil–geosynthetic interaction problems, the concurrent multiscale modeling strategy is incorporated into the hierarchical multiscale framework based on a coupled finite element method (FEM)/DEM approach, avoiding both the scale limitation of DEM models and the continuum-based constitutive models of a great complexity for geosynthetic-reinforced soils.

The sequential data assimilation technique, i.e. the particle filter, identifies the true values for the micro parameters with high accuracy in reproducing the experimental measurement. Instead of a single set of parameters, the identification comes in the form of probability density functions, which is deemed more objective than most optimization methods.

The DEM model of geotextile-wrapped soil is fabricated in a assembling–filtering–expanding packing generation process, using the calibrated mesoscale DEM model as the representative volume. The woven geotextile fabrics are discretized as an assembly of particles linked with stretching springs. Linear local and global stress paths are observed with the same slope until the rupture of the geotextile. Under simple shear, the global stress path approaches the critical state line first and then turns to the compression line of the wrapped soil. The representative volumes in the middle undergo some local loading–unloading stress paths, which may account for the high damping of sand-filled geotextile containers during cyclic shear. The reduced fabric anisotropies of the normal and tangential force chains suggest greater confinement from the lateral sides of the geosynthetic container in either loading course.

Having validated the DEM model of geotextile-wrapped granular soil, a comparative study is carried out to examine the influence of reinforcement form and geotextile stiffness on both the macroscale response and the microscale characteristics of the reinforced soil. The simulations show that the stiffness and strength of the wrapped soil are greater than those of the layered soil, and the amount of dilation within the reinforced zone is significantly larger in the latter than in the former. Consistent local and global stress paths are observed, suggesting analogous confinement mechanism in both reinforced soils. Shear deformation is relatively severe in the layered soil with notable localization near the edges, showcasing the ability of the wrapped soil to sustain shearing.

To lay a foundation for the analytical solution for geotextile-wrapped soil, the soil-geotextile interface behavior, principal stress distribution, and stress-strain behaviors of the constituent soil and geotextile are analyzed, considering a wide range of geotextile tensile stiffness in the DEM simulations of uniaxial compression tests on geotextile-wrapped soil. From the DEM analysis, a unique near-failure state line, which predicts the difference

between q/p and q_f/p at failure state, is identified for geotextile-wrapped soil under uniaxial compression. Dilation rates are related with stress ratios via a unique linear correlation regardless of geotextile tensile stiffness. The analytical model is validated by comparing the close-form solutions with the macroscopic responses of the DEM model under uniaxial compression. Though originally developed from uniaxial compression simulation results, the analytical solutions are in good agreement with the DEM solutions in triaxial loading conditions.

The scale of the above mentioned DEM models is largely restricted by the high computational cost. To circumvent this restriction, a multiscale model based on a coupled FEM/DEM approach is employed for general soil–geosynthetic interaction problems. The displacement in the granular soil is solved in the hierarchical multiscale framework, while the geosynthetic inclusion that prescribes the boundary conditions are modeled concurrently by discrete bar elements. The responses of both multiscale domains are communicated and updated in an explicit time integration scheme. The predicative capacity of this model is examined in two numerical examples, i.e., shape-forming and pull-out tests. The multiscale approach is proved to a versatile tool for handling a variety of the soil–geosynthetic interaction problems. The shape-forming multiscale simulation reveals increasing stress level and decreasing anisotropy at the local point near the top boundary where shear strain is larger than the rest of the soil domain. In the pull-out simulation, vortex-like displacement field is observed with the origin close to the left end of the geosynthetic inclusion. Such pattern is further confirmed by the dilative volumetric response at the local Gauss point above the geosynthetic inclusion.

Preface

I hereby declare that except where specific reference is made to the work of others, the contents of this thesis are original. Each chapter has been presented in or submitted to the following peer-reviewed publications.

Journal Papers

1. Cheng, H., Shuku, T., Thoeni, K. & Yamamoto, H., 2016a. Parameter identification for discrete element simulations of granular materials using the particle filter. *Powder Technology*. In preparation. (Chapter 2)

2. Cheng, H., Yamamoto, H. & Thoeni, K., 2016b. Numerical study on stress states and fabric anisotropies in soilbags using the DEM. *Computers and Geotechnics*, 76, pp.170–183. (Chapter 3)

3. Cheng, H. & Yamamoto, H., 2016c. Modeling microscopic behavior of geotextile-wrapped soil by discrete element method. *Japanese Geotechnical Society Special Publication*, 2(65), pp.2215–2220. (Chapter 3)

4. Cheng, H. & Yamamto, H., 2016d. Evaluating the performance of geotextile wrapped/layered Soil: a comparative study using the DEM. *Geotechnical Special Publications Book Series (American Society of Civil Engineering)*. In press. (Chapter 4)

5. Cheng, H., Yamamoto, H., Thoeni, K. & Wu, Y., 2016e. An analytical solution for geotextile-wrapped soil based on insights from DEM analysis. *Geotextiles and Geomembranes*. Submitted. (Chapter 5)

Conference papers in proceedings

1. Cheng, H., Shuku, T. & Yamamoto, H., 2016f. Parameter identification for DEM models of cohesionless granular soil using the particle filter. In *Proceedings of 51th JGS Annual Meeting*. Okayama, Japan. (Chapter 2)

2. Cheng, H. & Yamamoto, H., 2015a. Discrete modeling of geotextile-wrapped soil under simple shear. In *PARTICLE-BASED METHODS IV Fundamentals and Applications*. Barcelona, Spain, pp. 485–496. (Chapter 3)

3. Cheng, H., Yamamoto, H., Guo, N., et al., 2016g. A simple multiscale model for granular soils with geosynthetic inclusion. In *Proceedings of 7th International Conference on Discrete Element Methods (DEM7)*. Dalian, China. Submitted. (Chapter 6)

4. Cheng, H. & Yamamoto, H., 2016h. A multiscale approach for modeling soil-geosynthetic interaction. In *Proceedings of Annual Research Meeting Chugoku Chapter, Architectural Institute of Japan (AIJ)*, 39, pp.365–368. (Chapter 6)

5. Cheng, H. & Yamamoto, H., 2014. Hysteretic behaviours of soil-bag layer under irregular cyclic shear. In *Proceedings of Annual Research Meeting Chugoku Chapter, Architectural Institute of Japan (AIJ)*, 37, pp.61–64.

6. Cheng, H. & Yamamoto, H., 2013a. Dynamic analysis of base isolation with soilbags. In *Proceedings of Annual Research Meeting Chugoku Chapter, Architectural Institute of Japan (AIJ)*, pp. 183–186.

7. Cheng, H., Yamamoto, H., Jin, S. & Okano, S., 2013b. Soil reinforcement using soilbags – A preliminary study on its static and dynamic properties. In *Geotechnics for Sustainable Development*. Hanoi, Vietnam, pp. 569–578.

8. Yamamoto, H. & Cheng, H., 2012. Development study on device to reduce seismic response by using soil-bags assembles. In *Research, Development and Practice in Structural Engineering and Construction*. Perth, Australia, pp. 597–602.

Table of contents

List of figures

List of tables

Chapter 1

Introduction

1.1 Objectives and scope of study

Soil is a heterogeneous granular material that consists of solid particles, voids and pore fluids. The constituent granular particles jostle when subjected to external loads, causing densification and/or disintegration of the granular assembly, squeezing the fluids in/out the voids. Depending on the magnitudes of the interparticle contact forces, the phase regime of the granular assembly varies from gas-like to solid-like. The mechanical behavior of granular media in the jammed state is of primary concern in geotechnical engineering problems. The factors that contributes to the strength of granular geomaterials includes but not limited to interparticle friction, particle shapes, density, confining pressure, and water contents [Guo, 2014]. Unlike crystalline materials such as metal, loading a geomaterial toward failure is a progressive process which is essentially related to shearing on the "spatial mobilized plane" [Matsuoka and Sun, 2006].

Shear-induced granular failure can be catastrophic. Fig. 1.1a shows a landslide that struck Hiroshima city on August 20, 2014, causing 74 casualties and over ten billion JPY for clearing debris and recovery Wikipedia [2016a]. Japan is known for its frequent earthquakes. One of the most notorious ground failure during earthquakes is liquefaction, a solid–flow phase transition, which leads to a complete loss of support for superstructures (Fig. 1.1b Wikipedia

(a)

(b)

(c)

Fig. 1.1 Examples of disasters caused by granular failure (a) landslide in Hiroshima on August 20, 2014, (b) severe loss of bearing capacity due liquefaction occurred in 1964 Niigata earthquake, and (c) breached walls of a samurai-era castle.

[2016b]). A recent spurred by the 2016 Kumamoto earthquakes caused severe damage to invaluable cultural property of Japan (see the Kumamoto Castle in Fig. 1.1c News [2016]).

Among numerous countermeasures against shear failures in geomaterials, geosynthetic reinforcement draws more attention to practicing engineers for its cost-effectiveness, flexibility and easy construction, to name a few. Its reinforcing mechanisms lie in the interactions between geosynthetic fabrics and granular particles. Take the most commonly used geotextile sheets as an example. With sufficient compaction, granular particles are expected to penetrate into the apertures and conform to the undulations of the polymer fabrics. This so-called interlocking improves the shear resistance of granular structures in the vicinity of the geotextile reinforcement by strengthening the contact forces therein. In essence, the interlocking enforces a rough boundary condition onto the reinforced granular media, which results in a number of stiffer wedges/blocks separated by shear bands in a zig-zag pattern. During the formation of

these wedges/blocks, the tensile resistance of geotextile employs lateral confinement on the reinforced soil, sustaining shear failures till the rupture of geotextile fabrics.

Though a general consensus has been formed regarding the reinforcing mechanisms in geosynthetic-reinforced soils, i.e. confinement and interlocking, developing predictive models for this heterogeneous geomaterial is extremely difficult. This is mainly because the diversified forms of geosynthetic reinforcement. Depending on the complexity of geosynthetic-reinforced soils, relative contributions of the confinement and interlocking to the reinforcing effect differ from one form of reinforcement to another. Moreover, it is still unclear how confinement and interlocking behaviors benefit from each other when the reinforced soil is subjected to different loading conditions.

As the geosynthetic-reinforced geostructures (e.g. retaining walls, bridge abutments, subgrades, etc.) become more prevalent, a better understanding of the collective behavior of geosynthetic-reinforced granular soils is needed to optimize their engineering designs. One approach is to characterize the geosynthetic-reinforced soils with realistic representations of microstructures, interparticle forces and kinematics. With a well calibrated model for the micromechanics, this microscale-based approach offers more physically-sound evidence and insights for the analytical/constitutive modeling of geosynthetic-reinforced soils. Alternatively, one can avoid the efforts in developing the macroscale-based phenomenological models with reasonably coupled computational tools suited for different scales. This coupled approach will provide the soil–geosynthetic interaction problems with multiscale solutions which are rooted in the fundamental behaviors of confinement and interlocking between the reinforced granular soils and the geosynthetic inclusions. Accordingly the ***objectives*** of the current research are:

(i) To automatically identify possible values for contact law parameters in microscale-based models of granular soil, giving the associated probability for each value in reproducing the experimental observation;

(ii) To understand the behaviors of confinement and interlocking in geosynthetic-reinforced granular soils by investigating the evolutions of stress state, deformation patterns and

fabric characteristics, and to compare the reinforcing mechanisms and efficiencies of different forms of geosynthetic reinforcements;

(iii) To develop a simple analytical solution for geosynthetic-wrapped soil under compression, with new insights into the stress path and stress-dilatancy relation obtained from the microscale-based investigations on geosynthetic-reinforced granular soils;

(iv) To adapt the existing multiscale frameworks to soil–geosynthetic interaction problems, such that the numerical predictions are self-adaptive to complex loading histories and geometrical configurations of various geosynthetic-reinforced soils.

1.2 Literature review

1.2.1 Geosynthetic reinforcements

Over the past decades, the family of geosynthetics expands from simple flexible geotextile sheets to relatively stiffer geocells. Geosynthetics can be manufactured with great versatility for diverse purposes such as separation, drainage and reinforcement. For geotextiles along, the materials that are synthesized into geotextile fabrics range from common polypropylene (PE) to high-strength polyester (PET). The constituent fabrics may be woven, needle punched or heat bonded, etc. Because of the vast category and diversified forms, geosynthetics are very suitable for innovative designs of geostructures such as retaining walls [Cai and Bathurst, 1995; Juran and Christopher, 1989; Tatsuoka et al., 1997], foundations [Ahmed et al., 2015; Pulko et al., 2011; Zhang et al., 2012] and railway ballasts [Chen and McDowell, 2014; Indraratna and Nimbalkar, 2013; Indraratna et al., 2014]. This thesis focuses on flexible geotextiles included in granular geomaterials like sand and gravel for reinforcement purpose.

Geosynthetic-reinforced granular soils

Latha and Murthy [2007]; Madhavi Latha and Somwanshi [2009]; Tafreshi and Dawson [2010a,b] conducted comprehensive experimental investigations on geosynthetic reinforce-

ments that come in the forms of fibers, sheets and cell. It was confirmed that the cellular reinforcement systems behave much stiffer and sustain greater surcharge loads with less settlements, compared with the equivalent planar layers. Matsuoka and Liu [2006]; Matsuoka et al. [2004, 2003] discovered an astonishing rise of bearing capacity and high damping ratio by wrapping granular soils within geotextile containers (entirely closed cellular form). Geocells and geoencasements are other cellular forms of geosynthetic reinforcements which enclose granular soils circumferentially with additional radial confinement [Almeida et al., 2013; Pulko et al., 2011; Wu and Hong, 2014; Zhang et al., 2012]. These partially closed cellular forms are widely applied to reinforce weakly confined geostructures, like railway ballasts, in order to arrest lateral swelling/spreading [Indraratna et al., 2010, 2014; Ngo et al., 2015; Tafreshi and Dawson, 2010b]. In engineering applications, however, geostructures are seldom designed with only one specific form of geosynthetic-reinforced soil. Lohani et al. [2006]; Tatsuoka [2004]; Tatsuoka et al. [2007, 1997] promoted the geosynthetic-reinforced retaining walls and bridge abutments in which the cellular and planar forms of reinforcements are reasonably combined, considering various design factors including strength, drainage and stability, etc. On the other hand, the difference between the types and forms of geosynthetic-reinforced soils are sometimes vague as geotextile sheets can be wrapped around at the facing of retaining structures and anchored into the upper layer [Bathurst et al., 2006; Chareyre and Villard, 2005; He, 2008; Lajevardi et al., 2015] to replace more rigid sand-filled geotextile containers.

Geosynthetic-reinforced geostructures

Because of the diverse forms of geosynthetic-reinforced soils, innovative geostructures can be designed to fulfill a variety of engineering purposes. To stabilize railway foundations and minimize the maintenance cost, geogrids with large apertures and complex rib profiles are embedded within/beneath the ballast layers [Chen, 2013; Indraratna et al., 2013a,b; Indraratna and Nimbalkar, 2013]. Similarly, geotextile sheets are placed within the base course or at the interface between base and subgrade of unpaved/paved roads to attain more stable mechanical performance under cyclic wheel load [Bhandari and Han, 2010; Indraratna and

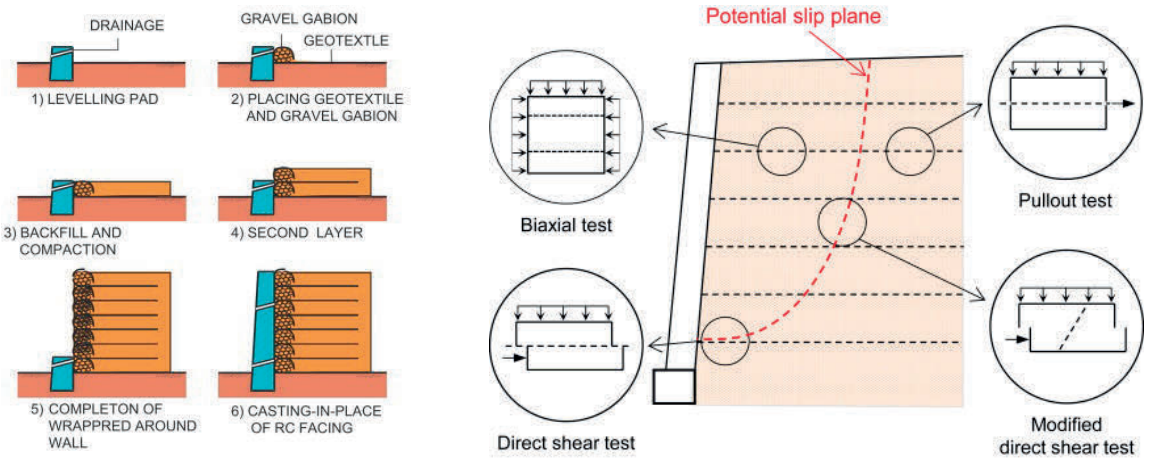

(a) (b)

Fig. 1.2 (a) Construction procedure for a geosynthetic-reinforced retaining wall [Tatsuoka et al., 2007] and (b) laboratory tests that characterize key soil–geosynthetic interaction mechanisms in a geosynthetic-reinforced retaining wall after Wang et al. [2016].

Nimbalkar, 2013]. Recent studies have found the sand-filled geotextile containers to be effective for reducing traffic-induced vibration as well [Liu et al., 2014b; Matsuoka et al., 2010; Muramatsu et al., 2009]. To facilitate the effect of stone columns on the settlement control of soft foundations, geotextile encasements are installed around the columns to contain the spreading of the granular stones towards the surrounding soft soil [Almeida et al., 2013; Pulko et al., 2011; Wu and Hong, 2014; Zhang et al., 2012]. For long-term food/coastal protection, permeable/impermeable geotextile containers or geomembrane tubes are stacked into dykes using the on-site slurry and sands [Alfaro et al., 2007; Chu et al., 2011; Guo et al., 2013; Lee and Douglas, 2012; Liu et al., 2015]. The most common geosynthetic-reinforced geostructures are retaining walls. In Tatsuoka's innovative design [Tatsuoka et al., 2007, 1997], vertically stacked gravel-filled containers serve as drainage paths while horizontal geogrid layers are arranged at optimized vertical spacing to achieve better cost-effectiveness, as shown schematically in Fig. 1.2a.

Experimental studies

For decades, model tests have been conducted to comprehensively evaluate the performance of a geosynthetic-reinforced geostructure, such as bearing capacity of a reinforced foundation [Adams and Collin, 1997; Madhavi Latha and Somwanshi, 2009; Nakai et al., 2016], degrada-

tion of reinforced railroad ballast [Chen, 2013; Indraratna and Nimbalkar, 2013; Indraratna et al., 2006], failure surface in a reinforced retaining wall and stability of stacked geotextile containers/tubes [Alfaro et al., 2007; Martinelli et al., 2011; Shin and Oh, 2007; Wang et al., 2015], among others. As geosynthetic-reinforced geostructures becomes a routine component of modern geotechnical design, more sophisticated laboratory tests are required to investigate the underpinning soil–geosynthetic interaction mechanisms as illustrated in Fig 1.2b.

By altering the arrangements of geosynthetic fabrics, e.g. woven/nonwoven geotextile aperture size [Subaida et al., 2008; Suksiripattanapong et al., 2013] and geogrid rib profile [Chen et al., 2013a; Teixeira et al., 2007] in pullout tests, we have obtained a better understanding of the interface behavior in the anchored zone, and its variation along the geosynthetic longitudinal and transverse directions of the reinforcement. Notably, Dyer [1985] employed photo-elasticity technique to visualize the interaction between grid transverse bearing members and granular soil particles. Ezzein and Bathurst [2014] quantified the displacement fields on the entire geogrid specimen by using advanced digital image processing and transparent granular soils. It was also demonstrated that the deformation pattern in the reinforced soil varies with respect to the distance from the reinforcement layer and the surcharge pressure. The same image processing method, i.e. Digital Image Correlation (DIC) was employed by Jacobs and Ziegler [2016] to provide quantitative insights into the development of shear zones within geogrid-reinforced soils in biaxial compression condition. The shear zones formed in plane-strain biaxial compression appeared to be separated by multiple inclined shear bands which are very close to those in geotextile-wrapped soil under compression [Cheng et al., 2016; Tantono, 2007]. The influence of the complexity of geogrid rib on the reinforcement performance was also investigated, whereas other works on the biaxial response of geosynthetic-reinforced soils focused more on the effect of the placement of geotextile/geogrid layers [Lackner et al., 2013; Latha and Murthy, 2007; Liu et al., 2014a; Morel and Gourc, 1997; Peng et al., 2000]. Recently, similar studies were conducted with triaxial compression apparatus [Madhavi Latha. and Nandhi Varman., 2016; Noorzad and Mirmoradi, 2010] and some extremely complicated reinforcement forms were adopted in

which the soil specimen was partitioned into tiny cells like a 'honeycomb' [Chen et al., 2013b; Rajagopal et al., 1999; Wesseloo et al., 2009].

Despite being capable of quantifying deformation in plane strain condition, even the state-of-the-art apparatus [Ezzein and Bathurst, 2014; Jacobs and Ziegler, 2016] cannot non-intrusively measure the 3D stress and strain distributions within the reinforced granular soil and the geosynthetic inclusion. For a detailed characterization of the stress-strain behavior of reinforced soil and its relation with the geosynthetic reinforcement, some advanced numerical models are needed as reviewed in the following sections. Once calibrated and validated with the laboratory test results, these models can provide precise measurements of stresses, strains and other key variables that are otherwise difficult to obtain in laboratory tests.

1.2.2 Macromechanics of geosynthetic-reinforced granular soils — analytical and continuum-based modeling

Analytical modeling

Due to the heterogeneous nature of geosynthetic-reinforced granular soils, analytical models of the reinforced soils or geostructures are relatively scarce. The existing analytical solutions were proposed exclusively for a handful of types and forms of reinforced soils/geostructures, considering their respective simplifications of soil–geosynthetic interactions. A variety of analytical methods were developed in the last century for the practical design of geosynthetic-reinforced soil walls [Abramento and Whittle, 1993; Ehrlich and Mitchell, 1994; Juran et al., 1990]. It is not until recently that the effect of the soil dilatancy has been taken into account to predict the reinforcement load within the horizontal placed geosynthetic sheets [Liu, 2016b; Liu and Won, 2014]. These works took advantages of existing hyperbolic stress-strain relationship of soil and Rowe's stress-dilatancy theory (elastic deformation neglected) to describe the nonlinear response of soil at the failure surface. The analytical method was proved to be more accurate in predicting the vertical profile of reinforcement strains, which can be used to examine the internal stability of geosynthetic-reinforced soil walls. Among the

analytical solutions for geosynthetic-encased stone columns, Pulko et al. [2011] adopted an elastoplastic approach to characterize soil behavior instead of a hyperbolic equation as in the analytical model of reinforced soil walls. Their solution was largely facilitated by assuming triaxial stress state for the encased stones. Similar assumptions was made in Wu and Hong [2014] which approximated the dilation-deviatoric strain relationship by that of unreinforced sand obtained from triaxial compression tests. Guo et al. Guo [2012b]; Guo et al. [2015, 2014, 2016b] developed a series of plain-strain analytical solutions for slurry/water-inflated geotubes on a rigid/deformable foundation. Assuming constant tensile force along the geotube hoop, both the settlements and shapes of the geotubes (not limited to one-layer stack) were well predicted with known pumping pressures.

Continuum-based modeling

Experimental investigations of granular behavior with novel apparatuses like those in [Ezzein and Bathurst, 2014; Jacobs and Ziegler, 2016] are much more expensive than numerical modeling. The experimental measurements have inherent uncertainty which arises from the randomness in a granular soil specimen. Numerical simulations on the other hand are deterministic. They avail us with quantitative characterization of soil behavior to assist engineering designs and constructions of geostructures. Continuum-based numerical methods like the finite element method (FEM) or the finite difference method (FDM) are extensively used to serve this need. In the continuum-based models of geosynthetic-reinforced retaining walls, different constitutive relations are required to represent the mechanical behavior of the component materials. In early numerical studies, hyperbolic constitutive models were adopted and extended to take into account the hysteretic behavior [Cai and Bathurst, 1995] and the dilative volumetric response [Karpurapu and Bathurst, 1995]. Nonlinear equations and interface slip models were applied to account for the tensile behavior of geosynthetic reinforcement and soil–geosynthetic interaction respectively. Recently, elastoplastic constitutive laws like the Mohr-Coulomb model [Almeida et al., 2013; Indraratna and Nimbalkar, 2013; Mosallanezhad et al., 2016] and modified Cam-Clay model [Chai et al., 2002; Rowe et al., 1996] have been applied for modeling the soil behaviors. Regarding the tensile properties

of geosynthetics, the constitutive modeling of geosynthetics have been largely advanced by Liu et al. [2007] considering the elastoplastic and viscoplastic nature of the material. With the help of recent progress in contact constraints, large deformations, surface separation and reclosure were successfully taken into account for modeling the complex interface behavior of geotextile-wrapped soil [Ansari et al., 2011]. In Tantono and Bauer's innovative work, the mechanical behavior of reinforced granular soil was described by a micro-polar hypoplastic model. The simulation based on a micro-polar continuum approach reproduced interesting strain localization in zig-zag patterns, similar to the shear bands observed in Jacobs and Ziegler [2016]. To date, most numerical studies on geotextile-wrapped soils used relatively simple constitutive models for the behaviors of soil and geosynthetics. Due to the scarceness of experimental data, the true mechanical states of the reinforced soil (excluding the reinforcement) remains unclear, such as the anisotropic properties of soil fabrics caused by the initial compaction [Liu, 2016a]. To meet this need, the current work adopts multiscale approaches, allowing macroscale investigation based on rigorously modeling of interaction between soil particles and geosynthetics at the microscale.

1.2.3 Micromechanics of geosynthetic-reinforced granular soils — microscopic measurement and modeling

Since Roscoe's pioneering work on "the yield of soils", there has been a significant amount of research on the numerical modeling of geomaterials within the critical state soil mechanics (CSSM) framework [Roscoe et al., 1958; Schofield and Wroth, 1968]. However, the original theory is criticized to be phenomenological for considering soils as isotropic elastoplastic materials rather than assemblies of discrete finite size particles. Inspired by micro-observations on confined rods under shearing, Matsuoka [Matsuoka, 1974; Matsuoka and Nakai, 1985; Matsuoka and Sun, 2006] extended the classic Mohr-Coulomb yield criterion to its 3D equivalent (SMP criterion) by conceptualizing a spatial plane where particles are most mobilized at failure. Revising the critical state-based constitutive models by the SMP criterion has resulted in good predictions for the mechanical behavior of clay, sand and cemmented soil,

among others [Matsuoka and Sun, 1995; Sun et al., 2004; Yao et al., 2008]. The anisotropic critical state theory [Li and Dafalias, 2012] is another example of recent development in soil constitutive modeling, motivated by improved micoscale understanding of granular material. With the rapid increase of computational power, the micoscale insights are gained not only from experimental measurements, but numerical simulations of granular assemblies as well.

Microscopic measurement

Over the past decades, experimental studies on granular behavior have been focusing on measuring the fabrics (microstructure [Oda, 1972]) and micromechanics of granular materials under shearing. To trace the location and transnational/rotational velocity of individual particle, sequential images of marked 2D rods assemblies were processed by image processing techniques, e.g. particle image velocimetry (PIV) and DIC, etc. Micro-observations of this type have been reported regarding granular flows induced by trap door condition [Murakami et al., 2000, 1999; Tanaka and Sakai, 1993] and strain localization under shearing [Alshibli and Sture, 1999; Calvetti et al., 1997; Evans, 2005]. As high-resolution tomographic techniques become increasingly viable in geotechnical laboratory tests [Andrade et al., 2011; Lim et al., 2015; Sun et al., 2011], more detailed information of granular assembly can be captured, such as local variation in void ratio, strain field and interparticle contact direction. The other branch of the experimental studies seeks a direct measurement of interparticle contact forces within an idealized 2D granular assembly (photoelastic rods) [Drescher and de Josselin de Jong, 1972; Oda et al., 1985; Zhang et al., 2010]. Nevertheless, an integrated apparatus capable of measuring both contact force chains and particle kinematics would require tremendous effort in both image processing and material science. A true 3D microscopic measurement of real sand particles is even impractical in this regard.

Microscopic modeling of granular particle assembly

An effective alternative to sophisticated experimental testing and measuring is microscopic simulation methods, especially the discrete element method (DEM) [Cundall and Strack,

1979]. With 3D particle shapes characterized by computer tomography imaging [Chang et al., 2003; Matsushima et al., 2009; Tsuchiyama et al., 2011] and well-calibrated contact laws [Thornton et al., 2011, 2013], DEM modeling of granular materials is capable of recovering the exact geometrical and mechanical information, ranging from individual particle kinematics to the stability of microstructure [Guo, 2012a; O'Sullivan, 2011; Xin, 2014]. Even though the existing discrete elements and contact constitutive laws remain highly simplified, extensive granular behaviors such as state-dependent dilatancy [Dafalias et al., 2004; Huang et al., 2014; Li and Dafalias, 2012], non-coaxiality [Guo, 2014; Qian et al., 2011; Yang, 2013], and anisotropy [Gu et al., 2013; Soga and Yimsiri, 2010; Wren and Borja, 1997; Yimsiri and Soga, 2011] have been successfully reproduced in numerous DEM studies. Nevertheless, due to simplified particle shapes and randomness in granular microstructures, no standard parameter identification of contact laws have been proposed to date.

DEM calculates interparticle contact force from small penetration between two adjoining particles. A variety of contact laws have been developed considering elasticity [Ng and Dobry, 1994; Tsuji et al., 1992], plasticity [Thornton, 1997] of the contact and viscous/plastic energy dissipation[Thornton et al., 2011, 2013]. The most popular and simple ones are Cundall's linear contact model and Hertz-Mindlin nonlinear elastic contact model. In the linear model, the overlap and relative tangential displacement are linearly related to normal and tangential force via constant contact stiffnesses, whereas in the Hertz-Mindlin model the stiffnesses are nonlinear functions of the overlap. Both the contact models are enforced by Coulomb's friction criterion to consider mobilization of particles under shearing. For cohesive granular soils, the normal and tangential bond elements [Jiang and Murakami, 2012] can be added at the cohesion surfaces. It has been recognized that approximating a granular packing with spherical particles results in lower peak and residual strengths (stress ratios), compared with those obtained from the laboratory tests. This is because the roundness of natural soil particles mainly ranges from sub-rounded to angular. Assembling a granular packing with perfect spherical particles poses an inherent threshold for the maximum shear strength. To obtain qualitative agreement with experimental response, moment transfer should be enabled at the contact point of two spherical discrete elements, with a plastic limit to account for the rolling

strength [Iwashita and Oda, 1998]. This approach has recently become a common practice in most DEM studies [O'Sullivan, 2011]. Nevertheless, it is still a workaround strategy to avoid a realistic representation of complex 3D particle shapes and textures. Despite being non-physical and conceptual, the rolling resistance is considered in the DEM simulations of this work because of its simplicity and less computational cost.

Microscopic modeling of geosynthetic inclusion

The numerical studies of geosynthetic-reinforced soils fall into two categories. The first is continuum-based modeling of reinforced geostructures, focusing on global characteristics such as failure pattern, stability, etc. The other investigates soil-geosynthetic interaction mechanisms via microscopic modeling of both soil particles and geosynthetic inclusion. Optimized designs of geosynthetic-reinforced soils are pursued in this type of studies, which is mostly accomplished through DEM modeling. The structural mechanics of geosynthetic fabrics can be characterized by orthogonal bars with nodes linked by diagonal and rotational springs. A simplified modeling of the wire mesh was initiated by Thoeni et al. [2014, 2013] in which stretching springs were mounted between remote particles with a stochastically distorted law that accounts for the initial distortion of the hexagonal steel wire meshes. The approach generally suits any woven system. Alternatively, bonded particles [Šmilauer et al., 2015] can be assembled into different forms of the geosynthetic fabrics such as geogrid ribs [Chen et al., 2012, 2013a, 2014; Ngo et al., 2015; Wang et al., 2016]. With properly calibrated parallel bonds, the tensile stress-strain and rotation-moment relationships of a geogrid specimen were accurately reproduced in the DEM simulations [Chen et al., 2013a; Ngo et al., 2015]. An important improvement was made by Chareyre and Villard [2005] in which geosynthetic inclusions were discretized into continuous chains of deformable spar elements. This 2D approach was later extended to the 3D case (cylinder elements) for discrete element modeling of soil-plant root interactions [Bourrier et al., 2013]. Because the constitutive relations for tension, shear, bending and twisting are defined between the nodes, a 3D chained cylinder (representing root in Bourrier et al. [2013]) can behave very similarly to an elastoplastic beam. Based on these previous works [Bourrier et al., 2013; Chareyre and

Villard, 2005; Thoeni et al., 2014, 2013], Effeindzourou et al. [2016] recently expanded the family of deformable discrete elements with a well-defined facet element (referred as PFacet). The PFacet element was proven to be efficient in modeling various deformable structures and their interactions with granular materials. By introducing virtual particles within the elements and tracking duplicate/insufficient contacts at the element connections, smooth contact surfaces are ensured for the structures constructed by 2D spars, 3D cylinders and PFacets. These deformable elements hold great potential for microscopic investigation of soil-geosynthetic interactions problems. More precisely, these smooth-surface deformable elements can separately handle the interlocking contributed by geosynthetic fabrics (aperture and undulation) and the surface friction of the polymer material.

1.2.4 Multiscale characterization and modeling of granular materials

Because granular structures and mechanics are rigorously characterized in DEM, it takes extremely high computational cost to solve large-scale boundary value problems. On the contrary, FEM can handle large-scale problems efficiently, but the continuum-based constitutive models that are derived from elementary tests of one geosynthetic-reinforced soil cannot be adapted to others in diverse forms and loading conditions. To solve large-scale boundary value problems with complex material behavior, the hierarchical multiscale approach which takes the advantages of both FEM and DEM seems to be a promising tool [Guo and Zhao, 2016; Guo et al., 2016a; Li et al., 2010; Liu, 2015; Meier et al., 2008; Shahin et al., 2016; Zhao and Guo, 2015]. Because the constitutive relations and stresses are numerically acquired from the contact mechanics of discrete particles, non-coaxially, anisotropy and non-associated flow are naturally obtained [Guo, 2014], making this approach well suited for modeling geosynthetic-reinforced soils that usually undergo complex stress history and localized deformation.

The so-called concurrent multiscale approach takes a different modeling strategy. DEM is exclusively used for the domains subjected to large deformation or located at interfaces, whereas FEM is employed exclusively for the homogeneous part. Regardless of the bridging

schemes adopted, the FE and DE domains coexist and are modeled separately, except for a small overlap of volume/surface where the kinematics and forces are shared [Breugnot et al., 2016; Dettmar, 2006; Indraratna et al., 2015; Wellmann and Wriggers, 2012; Xiao and Belytschko, 2004]. Applications of the concurrent approach have been successfully applied for the soil-structure interactions problems, such as near-tunnel soil loss [Dang and Meguid, 2013], pile penetration [Elmekati and Shamy, 2010; Wellmann and Wriggers, 2012], and soil–geosynthetic interaction [Tran et al., 2013; Villard et al., 2009] problems. In recent coupled FEM/DEM modeling of geosynthetic-reinforced soil, the geosynthetic inclusions were considered as continuous bodies by FEM, whereas the reinforced soil was modeled as an assembly of DEM particles concurrently. The simulation scale was therefore still limited to laboratory experiment size. Coupling the concurrent and hierarchical multiscale approaches could be a promising solution to remove the scale limitation: the displacement field of the reinforced soil is solved as a boundary value problem in the hierarchical multiscale framework, while the interactions between soil and geosynthetic inclusions are updated concurrently and applied as boundary conditions for the reinforced soil. In doing this, the high predictive capacity of DEM models can be preserved with improved computational deficiency achieved by parallelization. Most importantly, this coupled approach would not only predict the local and global response of soil-geosynthetic soils, but lead to multiscale interpretation of soil-geosynthetic interaction problems as well.

1.3 Thesis organization

This thesis investigates the multiscale mechanical behavior of geosynthetic-reinforced granular soils with two different modeling philosophies. The first method is based on pure DEM simulations of geosynthetic-reinforced soils in different forms, extracting the macroscale responses by computational homogenization. An analytical solution for geotextile-wrapped granular soil is facilitated by the macroscale insights obtained from the DEM simulations. In the second method, parallel DEM simulations of granular packings are managed hierarchically within the continuum description of a boundary value problem. The boundary condition

and material response are updated respectively from soil–geosynthetic interactions and local granular packings in a concurrent manner. The thesis is organized as below:

- Chapter 1: The objectives and scope of the study with a comprehensive literature review on recent progress in the mechanics of geosynthetic-reinforced granular soils.
- Chapter 2: Parameter identification process for DEM models of granular soil using the particle filter, considering a variety of contact laws, confining pressures and numbers of particles.
- Chapter 3: Discrete element modeling of geosynthetic-wrapped granular soil in uniaxial compression and simple shear loading conditions, with particular attention paid on the evolution of stress paths, interface friction and fabric anisotropies.
- Chapter 4: Evaluation of the relative performance of geotextile-wrapped and -layered granular soil, including the relative improvements of bearing capacity, difference in stress paths and strain localization.
- Chapter 5: Analytical modeling of geotextile-wrapped soil based on new assumptions of stress path and stress-dilatancy relationship developed from the findings in DEM simulations.
- Chapter 6: Multiscale characterization of granular soils with geosynthetic inclusion by integrating the concurrent multiscale approach within the hierarchical multiscale frameworks; two numerical examples: shape forming and pullout multiscale simulations.
- Chapter 7: Concluding remarks on major findings and contributions.

References

Abramento, M. and Whittle, A. J. (1993). Shear-lag analysis of planar soil reinforcement in planer strain compression. *Journal of Engineering Mechanics*, 119(2):270–291. pages 8

Adams, M. T. and Collin, J. G. (1997). Large model spread footing load tests on geosynthetic reinforced soil foundations. *Journal of Geotechnical and Geoenvironmental Engineering*, 123(1):66–72. pages 6

Ahmed, M., Tran, V., and Meguid, M. (2015). On the role of geogrid reinforcement in reducing earth pressure on buried pipes: experimental and numerical investigations. *Soils and Foundations*, 55(3):588–599. pages 4

Alfaro, M., Krahn, T., Bathurst, R. J., and Blatz, J. (2007). Large-scale interface shear testing of sandbag dyke materials. *Geosynthetics International*, 14(2):119–126. pages 6, 7

Almeida, M., Riccio, M., and Hosseinpour, I. (2013). Performance of a geosynthetic-encased column (GEC) in soft ground: numerical and analytical studies. *Geosynthetics International*, 20(4):252–262. pages 5, 6, 9

Alshibli, K. A. and Sture, S. (1999). Sand shear band thickness measurements by digital imaging techniques. *Journal of Computing in Civil Engineering*, 13(2):103–109. pages 11

Andrade, J., Avila, C., Hall, S., Lenoir, N., and Viggiani, G. (2011). Multiscale modeling and characterization of granular matter: From grain kinematics to continuum mechanics. *Journal of the Mechanics and Physics of Solids*, 59(2):237–250. pages 11

Ansari, Y., Merifield, R., Yamamoto, H., and Sheng, D. (2011). Numerical analysis of soilbags under compression and cyclic shear. *Computers and Geotechnics*, 38(5):659–668. pages 10

Bathurst, R. J., Vlachopoulos, N., Walters, D. L., Burgess, P. G., and Allen, T. M. (2006). The influence of facing stiffness on the performance of two geosynthetic reinforced soil retaining walls. *Canadian Geotechnical Journal*, 43(12):1225–1237. pages 5

Bhandari, A. and Han, J. (2010). Investigation of geotextile–soil interaction under a cyclic vertical load using the discrete element method. *Geotextiles and Geomembranes*, 28(1):33–43. pages 5

Bourrier, F., Kneib, F., Chareyre, B., and Fourcaud, T. (2013). Discrete modeling of granular soils reinforcement by plant roots. *Ecological Engineering*, 61:646–657. pages 13

Breugnot, A., Lambert, S., Villard, P., and Gotteland, P. (2016). A Discrete/continuous coupled approach for modeling impacts on cellular geostructures. *Rock Mechanics and Rock Engineering*, 49(5):1831–1848. pages 15

Cai, Z. and Bathurst, R. J. (1995). Seismic response analysis of geosynthetic reinforced soil segmental retaining walls by finite element method. *Computers and Geotechnics*, 17(4):523–546. pages 4, 9

Calvetti, F., Combe, G., and Lanier, J. (1997). Experimental micromechanical analysis of a 2D granular material: relation between structure evolution and loading path. *Mechanics of Cohesive-Frictional Materials*, 2:121–163. pages 11

Chai, J.-C., Miura, N., and Shen, S.-L. (2002). Performance of embankments with and without reinforcement on soft subsoil. *Canadian Geotechnical Journal*, 39(4):838–848. pages 9

Chang, C. S., Matsushima, T., and Lee, X. (2003). Heterogeneous strain and bonded ganular structure change in triaxial specimen studied by computer tomography. *Journal of Engineering Mechanics*, 129(11):1295–1307. pages 12

Chareyre, B. and Villard, P. (2005). Dynamic spar elements and discrete element methods in two dimensions for the modeling of soil-inclusion problems. *Journal of Engineering Mechanics*, 131(7):689–698. pages 5, 13

Chen, C. (2013). *Discrete element modelling of geogrid-reinforced railway ballast and track transition zones*. PhD thesis, The University of Nottingham. pages 5, 7

Chen, C., McDowell, G., and Thom, N. (2012). Discrete element modelling of cyclic loads of geogrid-reinforced ballast under confined and unconfined conditions. *Geotextiles and Geomembranes*, 35:76–86. pages 13

Chen, C. and McDowell, G. R. (2014). An investigation of the dynamic behaviour of track transition zones using discrete element modelling. *Proceedings of the Institution of Mechanical Engineers, Part F: Journal of Rail and Rapid Transit*, 0(0):0954409714528892–. pages 4

Chen, C., McDowell, G. R., and Thom, N. H. (2013a). A study of geogrid-reinforced ballast using laboratory pull-out tests and discrete element modelling. *Geomechanics and Geoengineering*, 8(4):244–253. pages 7, 13

Chen, C., McDowell, G. R., and Thom, N. H. (2014). Investigating geogrid-reinforced ballast: Experimental pull-out tests and discrete element modelling. *Soils and Foundations*, 54(1):1–11. pages 13

Chen, R.-H., Huang, Y.-W., and Huang, F.-C. (2013b). Confinement effect of geocells on sand samples under triaxial compression. *Geotextiles and Geomembranes*, 37:35–44. pages 8

Cheng, H., Yamamoto, H., and Thoeni, K. (2016). Numerical study on stress states and fabric anisotropies in soilbags using the DEM. *Computers and Geotechnics*, 76:170–183. pages 7

Chu, J., Guo, W., and Yan, S. W. (2011). Geosynthetic tubes and geosynthetic mats: Analyses and applications. *Geotechnical Engineering*, 42(1):56–65. pages 6

Cundall, P. A. and Strack, O. D. L. (1979). A discrete numerical model for granular assemblies. *Géotechnique*, 29(1):47–65. pages 11

Dafalias, Y. F., Papadimitriou, A. G., and Li, X. S. (2004). Sand plasticity model accounting for inherent fabric anisotropy. *Journal of Engineering Mechanics*, 130(11):1319–1333. pages 12

Dang, H. K. and Meguid, M. A. (2013). An efficient finite–discrete element method for quasi-static nonlinear soil–structure interaction problems. *International Journal for Numerical and Analytical Methods in Geomechanics*, 37. pages 15

Dettmar, J. P. (2006). *Static and dynamic homogenization analyses of discrete granular and atomistic structures on different time and length scales*. PhD thesis, der Universitat Stuttgart. pages 15

Drescher, A. and de Josselin de Jong, G. (1972). Photoelastic verification of a mechanical model for the flow of a granular material. *Journal of the Mechanics and Physics of Solids*, 20(5):337–340. pages 11

Dyer, M. R. (1985). *Observation of the stress distribution in crushed glass with applications to soil reinforcement*. PhD thesis, Unversity of Oxford. pages 7

Effeindzourou, A., Chareyre, B., Thoeni, K., Giacomini, A., and Kneib, F. (2016). Modelling of deformable structures in the general framework of the discrete element method. *Geotextiles and Geomembranes*, 44(2):143–156. pages 14

Ehrlich, M. and Mitchell, J. K. (1994). Working stress design method for reinforced soil walls. *Journal of Geotechnical Engineering*. pages 8

Elmekati, A. and Shamy, U. E. (2010). A practical co-simulation approach for multiscale analysis of geotechnical systems. *Computers and Geotechnics*, 37(4):494–503. pages 15

Evans, T. M. (2005). *Microscale physical and numerical investigations of shear banding in granular soils*. PhD thesis, Georgia Institute of Technology. pages 11

Ezzein, F. M. and Bathurst, R. J. (2014). A new approach to evaluate soil-geosynthetic interaction using a novel pullout test apparatus and transparent granular soil. *Geotextiles and Geomembranes*, 42(3):246–255. pages 7, 8, 9

Gu, X., Yang, J., and Huang, M. (2013). DEM simulations of the small strain stiffness of granular soils: effect of stress ratio. *Granular Matter*, 15(3):287–298. pages 12

Guo, N. (2014). *Multiscale characterization of the shear behavior of granulr media*. PhD thesis, Hong Kong University of Science and Technology. pages 1, 12, 14

Guo, N. and Zhao, J. (2016). 3D multiscale modeling of strain localization in granular media. *Computers and Geotechnics*. pages 14

Guo, N., Zhao, J., and Sun, W. (2016a). Multiscale analysis of shear failure of thick-walled hollow cylinder in dry sand. *Géotechnique Letters*, 6:1–18. pages 14

Guo, P. (2012a). Critical length of force chains and shear band thickness in dense granular materials. *Acta Geotechnica*, 7(1):41–55. pages 12

Guo, W. (2012b). *Geosynthetic tubes and mats: experimental and analytical studies*. PhD thesis, Nanyang Technological University. pages 9

Guo, W., Chu, J., and Yan, S. (2013). Recent studies of geosynthetic tubes and matterres: a overview. *Geotechnical Engineering Journal of the SEAGS & AGSSEA*, 44(4):115–124. pages 6

Guo, W., Chu, J., and Yan, S. (2015). Simplified analytical solution for geosynthetic tube resting on deformable foundation soil. *Geotextiles and Geomembranes*, 43(5):432–439. pages 9

Guo, W., Chu, J., Yan, S., and Nie, W. (2014). Analytical solutions for geosynthetic tube resting on rigid foundation. *Guo, Wei; Chu, Jian; Yan, Shuwang; Nie, Wen*, 6(1):65–77. pages 9

Guo, W., Kou, H., Zhou, B., Nie, W., and Chu, J. (2016b). Simplified methods to analyze geosynthetic mattress resting on deformable foundation soil. *Marine Georesources & Geotechnology*, page 1064119X.2016.1168499. pages 9

He, Z. (2008). *Geosynthetics rienforced structures subjected to blast load*. PhD thesis, National University of Singapore. pages 5

Huang, X., O'sullivan, C., Hanley, K. J., and Kwok, C. Y. (2014). Discrete-element method analysis of the state parameter. *Géotechnique*, 64(12):954–965. pages 12

Indraratna, B., Hussaini, S. K. K., and Vinod, J. (2013a). The lateral displacement response of geogrid-reinforced ballast under cyclic loading. *Geotextiles and Geomembranes*, 39:20–29. pages 5

Indraratna, B., Ngo, N. T., and Rujikiatkamjorn, C. (2013b). Deformation of coal fouled ballast stabilized with geogrid under cyclic load. *Journal of Geotechnical and Geoenvironmental Engineering*, 139(8):1275–1289. pages 5

Indraratna, B., Ngo, N. T., Rujikiatkamjorn, C., and Sloan, S. W. (2015). Coupled discrete element–finite difference method for analysing the load-deformation behaviour of a single stone column in soft soil. *Computers and Geotechnics*, 63:267–278. pages 15

Indraratna, B. and Nimbalkar, S. (2013). Stress-strain degradation response of railway ballast stabilized with geosynthetics. *Journal of Geotechnical and Geoenvironmental Engineering*, 139(5):684–700. pages 4, 5, 7, 9

Indraratna, B., Nimbalkar, S., Christie, D., Rujikiatkamjorn, C., and Vinod, J. (2010). Field assessment of the performance of a ballasted rail track with and without geosynthetics. *Journal of Geotechnical and Geoenvironmental Engineering*, 136(7):907–917. pages 5

Indraratna, B., Nimbalkar, S., and Rujikiatkamjorn, C. (2014). From theory to practice in track geomechanics – Australian perspective for synthetic inclusions. *Transportation Geotechnics*, 1(4):171–187. pages 4, 5

Indraratna, B., Salim, W., Christie, D., Indraratna, B., Khabbaz, H., and Salim, W. (2006). Geotechnical properties of ballast and the role of geosynthetics in rail track stabilisation Geotechnical properties of ballast and the role of geosynthetics in rail track stabilisation. *Ground Improvement*, 10(3):91–102. pages 7

Iwashita, K. and Oda, M. (1998). Rolling resistance at contacts in simulation of shear band development by DEM. *Journal of Engineering Mechanics*, 124(3):285–292. pages 13

Jacobs, F. and Ziegler, M. (2016). Investigation of global stress-strain and interaction behavior of geogrid reinforced soil with biaxial compression tests. *Japanese Geotechnical Society Special Publication*, 2(65):2209–2214. pages 7, 8, 9, 10

Jiang, M. and Murakami, A. (2012). Distinct element method analyses of idealized bonded-granulate cut slope. *Granular Matter*, 14(3):393–410. pages 12

Juran, I. and Christopher, B. (1989). Laboratory model study on geosynthetic reinforced soil retaining walls. *Journal of Geotechnical Engineering*. pages 4

Juran, I., Ider, H. M., and Farrag, K. (1990). Strain compatibility analysis for geosynthetics reinforced soil walls. *Journal of Geotechnical Engineering*, 116(2):312–329. pages 8

Karpurapu, R. and Bathurst, R. J. (1995). Behaviour of geosynthetic reinforced soil retaining walls using the finite element method. *Computers and Geotechnics*, 17(3):279–299. pages 9

Lackner, C., Bergado, D., and Semprich, S. (2013). Prestressed reinforced soil by geosynthetics – Concept and experimental investigations. *Geotextiles and Geomembranes*, 37:109–123. pages 7

Lajevardi, S. H., Dias, D., and Briançon, L. (2015). Experimental studies of the behaviour of geosynthetic wrap around anchorage. *Geosynthetics International*, 22(3):249–256. pages 5

Latha, G. M. and Murthy, V. S. (2007). Effects of reinforcement form on the behavior of geosynthetic reinforced sand. *Geotextiles and Geomembranes*, 25(1):23–32. pages 4, 7

Lee, E. and Douglas, R. (2012). Geotextile tubes as submerged dykes for shoreline management in Malaysia. *Geotextiles and Geomembranes*, 30:8–15. pages 6

Li, X., Zhang, X., and Zhang, J. (2010). A generalized Hill's lemma and micromechanically based macroscopic constitutive model for heterogeneous granular materials. *Computer Methods in Applied Mechanics and Engineering*, 199(49-52):3137–3152. pages 14

Li, X. S. and Dafalias, Y. F. (2012). Anisotropic critical state theory: role of fabric. *Journal of Engineering Mechanics*, 138(3):263–275. pages 11, 12

Lim, K.-W., Kawamoto, R., Andò, E., Viggiani, G., and Andrade, J. E. (2015). Multiscale characterization and modeling of granular materials through a computational mechanics avatar: a case study with experiment. *Acta Geotechnica*. pages 11

Liu, C.-N., Yang, K.-H., and Nguyen, M. D. (2014a). Behavior of geogrid–reinforced sand and effect of reinforcement anchorage in large-scale plane strain compression. *Geotextiles and Geomembranes*, 42(5):479–493. pages 7

Liu, H. (2016a). Nonlinear elastic analysis of reinforcement loads for vertical reinforced soil composites without facing restriction. *Journal of Geotechnical and Geoenvironmental Engineering*, page 04016013. pages 10

Liu, H. (2016b). Required reinforcement stiffness for vertical geosynthetic-reinforced-soil walls at strength limit state. *Géotechnique*, 66(5):424–434. pages 8

Liu, H., Ling, H. I., and Asce, M. (2007). Unified elastoplastic–viscoplastic bounding surface model of geosynthetics and its applications to geosynthetic reinforced soil-retaining wall analysis. *Journal of Engineering Mechanics*, 133(7):801–815. pages 10

Liu, H. and Won, M.-S. (2014). Stress dilatancy and reinforcement load of vertical-reinforced soil composite: analytical method. *Journal of Engineering Mechanics*, 140(3):630–639. pages 8

Liu, S., Gao, J., Wang, Y., and Weng, L. (2014b). Experimental study on vibration reduction by using soilbags. *Geotextiles and Geomembranes*, 42(1):52–62. pages 6

Liu, S., Lu, Y., Weng, L., and Bai, F. (2015). Field study of treatment for expansive soil/rock channel slope with soilbags. *Geotextiles and Geomembranes*, 43(4):283–292. pages 6

Liu, Y. (2015). *Multiscale modeling of granular materials*. PhD thesis, Columbia University. pages 14

Lohani, T., Matsushima, K., Aqil, U., Mohri, Y., and Tatsuoka, F. (2006). Evaluating the strength and deformation characteristics of a soil bag pile from full-scale laboratory tests. *Geosynthetics International*, 13(6):246–264. pages 5

Madhavi Latha., G. and Nandhi Varman., A. (2016). Static and cyclic load response of reinforced sand through large triaxial tests. *Japanese Geotechnical Society Special Publication*, 2(68):2342–2346. pages 7

Madhavi Latha, G. and Somwanshi, A. (2009). Effect of reinforcement form on the bearing capacity of square footings on sand. *Geotextiles and Geomembranes*, 27(6):409–422. pages 4, 6

Martinelli, L., Zanuttigh, B., De Nigris, N., and Preti, M. (2011). Sand bag barriers for coastal protection along the Emilia Romagna littoral, Northern Adriatic Sea, Italy. *Geotextiles and Geomembranes*, 29(4):370–380. pages 7

Matsuoka, H. (1974). Stress-strain relationships of sands based on the mobilized plane. *Soils and Foundations*, 14(2):47–61. pages 10

Matsuoka, H. and Liu, S. (2006). *A new earth reinforcement method using soilbags*. Taylor & Francis/Balkema, The Netherlands (2006). pages 5

Matsuoka, H., Liu, S., Hasebe, T., and Shimao, R. (2004). Deformation-strength properties and design methods of soilbag assembly. *Doboku Gakkai Ronbunshu*, 764(III-67):169–181. pages 5

Matsuoka, H. and Nakai, T. (1985). Relationship among Tresca, Mises, Mohr-Coulomb and Matsuoka-Nakai failure criteria. *Soils and Foundations*, 25(4):123–128. pages 10

Matsuoka, H. and Sun, D. (1995). Extension of spatially mobilized plane (SMP) to frictional and cohesive materials and its application to cemented sands. *Soils and Foundations*, 35(4):63–72. pages 11

Matsuoka, H. and Sun, D. (2006). *The SMP concept-based 3D constitutive models for geomaterials*. CRC Press. pages 1, 10

Matsuoka, H., Yamamoto, H., Matsuoka, H., and Yamamoto, H. (2003). Cyclic shearing property and damping ratio of soilbag assembly. In *the 38th Japan national conference on geotechnical engineering*, pages 757–758. pages 5

Matsuoka, H., Yamamoto, H., and Nomoto, F. (2010). D·Box method as modern soilbag technology and its local consolidation and vibration reduction effects. *Geosynthetics Engineering Journal*, 25:19–26. pages 6

Matsushima, T., Katagiri, J., Uesugi, K., Tsuchiyama, A., and Nakano, T. (2009). 3D shape characterization and image-based DEM simulation of the lunar soil simulant FJS-1. *Journal of Aerospace Engineering*, 22(1):15–23. pages 12

Meier, H., Steinmann, P., and Kuhl, E. (2008). Towards multiscale computation of confined granular media: contact forces, stresses and tangent operators. *Technische Mechanik*. pages 14

Morel, J. and Gourc, J. (1997). Mechanical behavior of sand reinforced with mesh elements. *Geosynthetics International*, 4(5):481–508. pages 7

Mosallanezhad, M., Taghavi, S. S., Hataf, N., and Alfaro, M. (2016). Experimental and numerical studies of the performance of the new reinforcement system under pull-out conditions. *Geotextiles and Geomembranes*, 44(1):70–80. pages 9

Murakami, A., Matsuoka, A., Aoyama, S., and Sakaguchi, H. (2000). Analysis of granular behavior and contact force distribution of granules by CL-CA. *Transactions of The Japanese Society of Irrigation, Drainage and Reclamation Engineering*, 208:561–567. pages 11

Murakami, A., Sakaguchi, H., Takao, T., and Hasegawa, T. (1999). Formation of shear bands and vortices in granular media. *Transactions of the Japanese Society of Irrigation, Drainage and Reclamation Engineering*. pages 11

Muramatsu, D., Bin, Y., and Zhang, F. (2009). Numerical simulation of vibration damping effect of soilbag. *Japanese Geotechnical Journal*, 4(1):71–80. pages 6

Nakai, T., Shahin, H. M., Morikawa, Y., Masuda, S., and Mio, S. (2016). Effective reinforcing method for increasing bearing capacity with geosynthetics. *Japanese Geotechnical Society Special Publication*, 2(67):2268–2273. pages 6

News (2016). Quake-damaged Kumamoto Castle to take decades to restore. *The Japan Times Online*. pages 2

Ng, T.-t. and Dobry, R. (1994). Numerical simulations of monotonic and cyclic loading of granular soil. *Journal of Geotechnical Engineering*, 120(2):388–403. pages 12

Ngo, N. T., Indraratna, B., Rujikiatkamjorn, C., Biabani, M. M., and Mahdi Biabani, M. (2015). Experimental and discrete element modeling of geocell-stabilized subballast subjected to cyclic loading. *Journal of Geotechnical and Geoenvironmental Engineering*, page 04015100. pages 5, 13

Noorzad, R. and Mirmoradi, S. (2010). Laboratory evaluation of the behavior of a geotextile reinforced clay. *Geotextiles and Geomembranes*, 28(4):386–392. pages 7

Oda, M. (1972). Initial fabrics and their relations to mechanical properties of granular material. *Soils and Foundations*, 12(1)(1):17–36. pages 11

Oda, M., Nemat-Nasser, S., and Konishi, J. (1985). Stress-induced anisotropy in granular masses. *Soils and foundations*, 25(3):85–97. pages 11

O'Sullivan, C. (2011). *Particulate discrete element modelling: a geomechanics perspective*. Taylor & Francis, Hoboken, NJ. pages 12, 13

Peng, F., Kotake, N., Tatsuoka, F., Hirakawa, D., and Tanaka, T. (2000). Plane strain compression behaviour of geogrid-reinforced sand and its numerical analysis. *Soils and Foundations*, 40(3):55–74. pages 7

Pulko, B., Majes, B., and Logar, J. (2011). Geosynthetic-encased stone columns: Analytical calculation model. *Geotextiles and Geomembranes*, 29(1):29–39. pages 4, 5, 6, 9

Qian, J., Huang, M., and Sun, H. (2011). Macro-micromechanical approaches for non-coaxiality of coarse grained soils. *Science China Technological Sciences*, 54(S1):147–153. pages 12

Rajagopal, K., Krishnaswamy, N., and Madhavi Latha, G. (1999). Behaviour of sand confined with single and multiple geocells. *Geotextiles and Geomembranes*, 17(3):171–184. pages 8

Roscoe, K. H., Schofield, A. N., and Wroth, C. P. (1958). On the yielding of soils. *Géotechnique*, 8(1):22–53. pages 10

Rowe, R. K., Gnanendran, C. T., Landva, A. O., and Valsangkar, A. J. (1996). Calculated and observed behaviour of a reinforced embankment over soft compressible soil. *Canadian Geotechnical Journal*, 33(2):324–338. pages 9

Schofield, A. N. and Wroth, P. (1968). *Critical state soil mechanics*. McGraw-Hill, New York. pages 10

Shahin, G., Desrues, J., Dal Pont, S., Combe, G., and Argilaga, A. (2016). A study of the influence of REV variability in double scale FEM×DEM analysis. *International Journal for Numerical Methods in Engineering*, pages n/a–n/a. pages 14

Shin, E. C. and Oh, Y. I. (2007). Coastal erosion prevention by geotextile tube technology. *Geotextiles and Geomembranes*, 25(4–5):264–277. pages 7

Šmilauer, V., Chareyre, B., Duriez, J., Eulitz, A., Gladky, A., Guo, N., Jakob, C., and Kozicki, J. (2015). Using and Programming. In Project, T. Y., editor, *Yade Documentation*. 2 edition. pages 13

Soga, K. and Yimsiri, S. (2010). DEM analysis of soil fabric effects on behaviour of sand. *Géotechnique*, 60(6):483–495. pages 12

Subaida, E. A., Chandrakaran, S., and Sankar, N. (2008). Experimental investigations on tensile and pullout behaviour of woven coir geotextiles. *Geotextiles and Geomembranes*, 26(5):384–392. pages 7

Suksiripattanapong, C., Horpibulsuk, S., Chinkulkijniwat, A., and Chai, J. C. (2013). Pullout resistance of bearing reinforcement embedded in coarse-grained soils. *Geotextiles and Geomembranes*, 36:44–54. pages 7

Sun, D., Matsuoka, H., Yao, Y., and Ishii, H. (2004). An anisotropic hardening elastoplastic model for clays and sands and its application to FE analysis. *Computers and Geotechnics*, 31(1):37–46. pages 11

Sun, W., Andrade, J. E., Rudnicki, J. W., and Eichhubl, P. (2011). Connecting microstructural attributes and permeability from 3D tomographic images of in situ shear-enhanced com-

paction bands using multiscale computations. *Geophysical Research Letters*, 38(10):n/a–n/a. pages 11

Tafreshi, S. M. and Dawson, A. (2010a). Behaviour of footings on reinforced sand subjected to repeated loading – Comparing use of 3D and planar geotextile. *Geotextiles and Geomembranes*, 28(5):434–447. pages 4

Tafreshi, S. M. and Dawson, A. (2010b). Comparison of bearing capacity of a strip footing on sand with geocell and with planar forms of geotextile reinforcement. *Geotextiles and Geomembranes*, 28(1):72–84. pages 4, 5

Tanaka, T. and Sakai, T. (1993). Progressive failure and scale effect of trap-door problems with granular materials. *Soils and Foundations*, 33(1):11–22. pages 11

Tantono, S. F. (2007). *The mechanical behavior of a soilbag under vertical Compression*. PhD thesis, Graz University of Technology. pages 7

Tatsuoka, F. (2004). An approximate isotropic perfectly plastic solution for compressive strength of geosynthetic-reinforced soil. *Geosynthetics International*, 11(5):390–405. pages 5

Tatsuoka, F., Tateyama, M., Mohri, Y., and Matsushima, K. (2007). Remedial treatment of soil structures using geosynthetic-reinforcing technology. *Geotextiles and Geomembranes*, 25(4-5):204–220. pages xv, 5, 6

Tatsuoka, F., Tateyama, M., Uchimura, T., and Koseki, J. (1997). Geosynthetic-reinforced soil retaining walls as important permanent structures. *Geosynthetics International*, 4(2):81–136. pages 4, 5, 6

Teixeira, S. H. C., Bueno, B. S., and Zornberg, J. G. (2007). Pullout resistance of individual longitudinal and transverse geogrid ribs. *Journal of Geotechnical and Geoenvironmental Engineering*, 133(1):37–50. pages 7

Thoeni, K., Giacomini, A., Lambert, C., Sloan, S. W., and Carter, J. P. (2014). A 3D discrete element modelling approach for rockfall analysis with drapery systems. *International Journal of Rock Mechanics and Mining Sciences*, 68:107–119. pages 13, 14

Thoeni, K., Lambert, C., Giacomini, A., and Sloan, S. W. (2013). Discrete modelling of hexagonal wire meshes with a stochastically distorted contact model. *Computers and Geotechnics*, 49:158–169. pages 13, 14

Thornton, C. (1997). Coefficient of restitution for collinear collisions of elastic-perfectly plastic spheres. *Journal of Applied Mechanics*. pages 12

Thornton, C., Cummins, S. J., and Cleary, P. W. (2011). An investigation of the comparative behaviour of alternative contact force models during elastic collisions. *Powder Technology*, 210(3):189–197. pages 12

Thornton, C., Cummins, S. J., and Cleary, P. W. (2013). An investigation of the comparative behaviour of alternative contact force models during inelastic collisions. *Powder Technology*, 233:30–46. pages 12

Tran, V., Meguid, M., and Chouinard, L. (2013). A finite–discrete element framework for the 3D modeling of geogrid–soil interaction under pullout loading conditions. *Geotextiles and Geomembranes*, 37:1–9. pages 15

Tsuchiyama, A., Uesugi, M., Matsushima, T., Michikami, T., Kadono, T., Nakamura, T., Uesugi, K., Nakano, T., Sandford, S. A., Noguchi, R., Matsumoto, T., Matsuno, J., Nagano, T., Imai, Y., Takeuchi, A., Suzuki, Y., Ogami, T., Katagiri, J., Ebihara, M., Ireland, T. R., Kitajima, F., Nagao, K., Naraoka, H., Noguchi, T., Okazaki, R., Yurimoto, H., Zolensky, M. E., Mukai, T., Abe, M., Yada, T., Fujimura, A., Yoshikawa, M., and Kawaguchi, J. (2011). Three-dimensional structure of Hayabusa samples: origin and evolution of Itokawa regolith. *Science (New York, N.Y.)*, 333(6046):1125–8. pages 12

Tsuji, Y., Tanaka, T., and Ishida, T. (1992). Lagrangian numerical simulation of plug flow of cohesionless particles in a horizontal pipe. *Powder Technology*, 71(3):239–250. pages 12

Villard, P., Chevalier, B., Le Hello, B., and Combe, G. (2009). Coupling between finite and discrete element methods for the modelling of earth structures reinforced by geosynthetic. *Computers and Geotechnics*, 36(5):709–717. pages 15

Wang, L.-J., Liu, S.-H., and Zhou, B. (2015). Experimental study on the inclusion of soilbags in retaining walls constructed in expansive soils. *Geotextiles and Geomembranes*, 43(1):89–96. pages 7

Wang, Z., Jacobs, F., and Ziegler, M. (2016). Experimental and DEM investigation of geogrid–soil interaction under pullout loads. *Geotextiles and Geomembranes*, 44(3):230–246. pages xv, 6, 13

Wellmann, C. and Wriggers, P. (2012). A two-scale model of granular materials. *Computer Methods in Applied Mechanics and Engineering*, 205-208:46–58. pages 15

Wesseloo, J., Visser, A., and Rust, E. (2009). The stress–strain behaviour of multiple cell geocell packs. *Geotextiles and Geomembranes*, 27(1):31–38. pages 8

Wikipedia (2016a). 2014 Hiroshima landslides. pages 1

Wikipedia (2016b). Soil liquefaction. pages 1

Wren, J. R. and Borja, R. I. (1997). Micromechanics of granular media Part II: Overall tangential moduli and localization model for periodic assemblies of circular disks. *Computer Methods in Applied Mechanics and Engineering*, 141(3-4):221–246. pages 12

Wu, C.-S. and Hong, Y.-S. (2014). A simplified approach for evaluating the bearing performance of encased granular columns. *Geotextiles and Geomembranes*, 42(4):339–347. pages 5, 6, 9

Xiao, S. and Belytschko, T. (2004). A bridging domain method for coupling continua with molecular dynamics. *Computer Methods in Applied Mechanics and Engineering*, 193(17-20):1645–1669. pages 15

Xin, H. (2014). *Exploring critical-state behaviour using DEM*. PhD thesis, The University of Hong Kong. pages 12

Yang, D. (2013). *Microscopic study of granular material behaviours under general stress paths*. PhD thesis, University of Nottingham. pages 12

Yao, Y., Sun, D., and Matsuoka, H. (2008). A unified constitutive model for both clay and sand with hardening parameter independent on stress path. *Computers and Geotechnics*, 35(2):210–222. pages 11

Yimsiri, S. and Soga, K. (2011). Effects of soil fabric on behaviors of granular soils: Microscopic modeling. *Computers and Geotechnics*, 38(7):861–874. pages 12

Zhang, J., Majmudar, T. S., Tordesillas, A., and Behringer, R. P. (2010). Statistical properties of a 2D granular material subjected to cyclic shear. *Granular Matter*, 12(2):159–172. pages 11

Zhang, Y., Chan, D., and Wang, Y. (2012). Consolidation of composite foundation improved by geosynthetic-encased stone columns. *Geotextiles and Geomembranes*, 32:10–17. pages 4, 5, 6

Zhao, J. and Guo, N. (2015). The interplay between anisotropy and strain localisation in granular soils: a multiscale insight. *Géotechnique*, 65(8):642–656. pages 14

Chapter 2

Parameter Identification for DEM models of Granular Soil Using the Particle Filter

2.1 Introduction

Discrete element modeling is capable of capturing the collective behaviors of granular media with a relatively small number of parameters [Cundall and Strack, 1979; Kawaguchi et al., 1998; O'Sullivan, 2011]. The Discrete Element Method (DEM) often brings forth innovative cross-scale insights [Breugnot et al., 2016; Guo and Zhao, 2016; Shahin et al., 2016] that are difficult to acquire from either sophisticated experiments or complex continuum-based numerical simulations. Notwithstanding the versatility, a DEM model with parameters having the micromechanical origins requires 'calibration' against the macroscopic experimental responses of the granular material in order to reproduce meaningful numerical results. The analytical formulas of micro-macro transition can provide some guidelines for the calibration of DEM models [Misra and Yang, 2010; Stransky and Jirasek, 2011; Wang and Mora, 2008], but they are only available for ideal granular assemblies within the elastic range. Unlike the bulk material properties, the micromechanical behaviors are difficult to characterize compre-

hensively even with state-of-the-art experimental apparatuses. Although a few initial attempts were made to measure experimentally the microscopic responses of granular materials, such as the force-displacement relationships of two contacting balls or grains [Barrios et al., 2013; Paulick et al., 2014], most widely applied contact laws, i.e. the classical linear (CL) [Cundall and Strack, 1979] and Hertz-Mindlin (HM) contact laws [Johnson, 1985] in commercial DEM codes [EDEM 2.4, 2011; Itasca Consulting Group, 2014], cannot make exact predictions for the measured experimental data. This is mainly because the roles of the micromechanical parameters in governing the contact behaviors are still unclear. Additional parameters or further development of the formulations are needed to achieve better agreement [Luding, 1998, 2008; Thornton et al., 2011, 2013]. However, for practical applications of the DEM in a cost-effective manner [Bonilla-Sierra et al., 2015; Cheng et al., 2016; Huang et al., 2014; Thoeni et al., 2014], the simplified contact laws are usually adopted and are often coupled with fictitious non-physical parameters, e.g., rolling and bending stiffnesses [Iwashita and Oda, 1998; Jiang et al., 2005]. Over the past decades, an extensive range of DEM simulations have been carried out with these simplified laws to advance our understanding of granular materials in flow and/or jammed states. The majority of these works has successfully contributed to the development of microstructure-related investigations [Guo and Zhao, 2013; Matsushima and Blumenfeld, 2014; Yimsiri and Soga, 2011] and theories [Li and Yu, 2013; Wan and Guo, 2014; Zhao and Guo, 2013], but the importance in the matter of parameter identification for discrete element simulations is usually overlooked.

The conventional calibration procedure for DEM models employs a ‘one at a time’ analysis of the parameters. A number of initial works were carried out to derive the micro-macro interpolation charts via sensitivity analyses using the ‘one at a time’ approach. Depending on the contact laws applied and granular materials considered, various relationships between micromechanical parameters and measured macroscopic characteristics were obtained. For DEM models governed by linear contact laws, linear relations between Young’s modulus and normal contact stiffness were identified for rocks [Coetzee, 2016; Kulatilake et al., 2001; Wang and Tonon, 2010], whereas others found the relations to be nonlinear in the case of sands [Plassiard et al., 2009]. Some concluded that shear contact stiffness is linearly related

to both Young's modulus and Poisson's ratio from the 'one at a time' sensitivity analyses [Belheine et al., 2009; Plassiard et al., 2009], despite the fact that coupled effects may exist between normal and shear contact stiffnesses. The parameters that characterize deformability (e.g., contact stiffnesses) and strength (e.g., interparticle friction angle), however, are generally believed to be uncoupled in the literature. This has led to a number of parametric studies on the internal friction angle which showed nonlinear relationships between the shear strength of granular media and interparticle friction angle [Coetzee, 2016; Soga and Yimsiri, 2010; Thornton, 2000], without reference to contact stiffnesses.

Because of the coupled effects, an identified parameter set for a given DEM model is merely one of the numerous solutions to the multi-modal parameter identification problem. Among a handful of systematic approaches for the calibration of DEM models, the design of experiments (DOE) methods are efficient in searching possible solutions in the multi-dimensional parameter space with a manageable number of DEM simulations and optimized outcomes [Hanley et al., 2011; Johnstone, 2010; Yoon, 2007]. Hanley et al. [2011] applied the DOE for calibrating the DEM models of crushable agglomerate. The interaction between key parameters were taken into account by the orthogonal arrays designed with the Taguchi methods. Yoon [2007] developed a two-step optimization process in which a DOE method (Plackett–Burman design) was first applied to select the parameters with largest impacts on the macroscopic characteristics and the statistical micro-macro correlations were then estimated with additional DEM simulations. Despite of good predictions for the macroscopic characteristics (e.g., compressive strength), the predicted temporal responses (e.g., stress-strain curves) did not agree well with the experimental results. Furthermore, the DOE methods require the knowledge of interaction between parameters which is neither usually available nor well understood for a wide variety of granular materials.

Both the aforementioned approaches aim to portray the variation of one macroscopic characteristic as a function of one or multiple micromechanical parameters. One significant limitation of these approaches is that the calibration can only be conducted against the bulk material properties (e.g., Young's modulus, peak and critical friction angle of sand specimen in drained triaxial compression (DTC) tests) that characterize the instantaneous elastoplastic

behaviors of granular materials, which inevitably leads to insufficient agreement between the simulated and measured stress-strain responses [Yoon, 2007]. Furthermore, it is known that stress history plays a vital role in the elastoplastic constitutive relations of granular soils [Schofield and Wroth, 1968], i.e. the current deformation depends on the stress paths from the beginning up to the current stress state. Therefore, considering the complete observation data of mechanical behaviors throughout the full history of changes in loading and boundary conditions is pivotal to the parameter identification for the DEM simulations of granular materials.

The parameter identification process is essentially an inverse problem. The sequential data assimilation techniques [Evensen, 1994; Nakano et al., 2007] are suitable for solving the inversion problems with the above-mentioned difficulties in the system models. The particle filter[1] (PF) and sequential importance sampling (SIS), which can jointly deal with the elastoplasticity of granular materials [Murakami et al., 2013; Shuku et al., 2012], are selected for the current problem. The PF applies the recursive formula of the sequential Bayesian estimation and approximates the posterior PDF with the SIS particle filtering algorithm. The proposed calibration approach for DEM simulations is expedient, because the PF is well-justified for nonlinear and non-Gaussian problems as demonstrated by [Murakami et al., 2013; Shuku et al., 2012] in their applications of the PF to the continuum-based simulations of geotechnical problems. Moreover, both the PF and SIS can be easily implemented for the open-source DEM package YADE [Šmilauer et al., 2015] which can conveniently run DEM simulations in parallel as the model trajectories for Monte Carlo sampling. Zhang [Zhang et al., 2011] and Hadjidoukas [Hadjidoukas et al., 2014] employed the Markov Chain Monte Carlo methods alternatively to generate samples from the posterior PDF of the micromechanical parameters. Nevertheless, they either enforced assumptions on the prior distributions [Zhang et al., 2011] or considered the DEM simulations of very simple granular systems [Hadjidoukas et al., 2014]. To the author's knowledge, the present work is the first attempt to develop a systematic parameter identification procedure with the PF and SIS algorithms for DEM model calibration against the full history of the physical mechanical responses of granular materials.

[1]The word 'particle' is referred as a 'sample' for approximating posterior probability distribution functions (PDF) and should not be comprehended as a DEM particle.

2.2 Fundamentals of the particle filter

The PF is a sequential data assimilation method, known to be preferable for nonlinear and non-Gaussian problems. It uses the recursive formula of the sequential Bayesian framework with the posterior probability distributions approximated by appropriate weight on each particle (a parameter set). When applied with the sequential importance sampling (SIS) algorithm, the PF can keep tracking the complete trajectories of the initially generated particles during the whole loading history instead of regenerating new particles based on the observation data at different loading stages as in the classical particle filtering algorithm (sampling importance resampling). Because the micromechanical parameters of each particle stay the same during the filtering process and only the associated weights are updated from the distances between sequentially measured and predicted time-dependent mechanical responses, the PF together with the SIS can take into account the effects of stress history and strain-dependency as appeared in the measured mechanical behaviors which are also known as the distinctive natures of soil.

Considering a Toyoura sand specimen ($e_0 = 0.68$) modeled by a DEM granular assembly with the same void ratio, the states of the specimen and its DEM counterpart are described in a nonlinear and non-Gaussian state space model:

$$x_t = f_t(x_{t-1}) + \upsilon_t \tag{2.1}$$

$$y_t = h_t(x_t) + \omega_t \tag{2.2}$$

where the state vector x_t consists of three variables that characterize the triaxial behavior of the DEM granular model, namely, stress ratio σ_a/σ_r, radial strain ε_r and volumetric strain ε_v at a discrete time step t, whereas the observation vector y_t is directly measured in the triaxial tests [Sun et al., 2007]; υ_t and ω_t are the system error and the observation error whose probability tensity functions (PDFs) follow normal distribution with zero averages. In this study, system error was assumed to be zero not to destroy the dynamical balance of the DEM simulation. The operator f_t represents the current state change of the DEM model, resulted

from its preceding states. In the current simple problem, the nonlinear function h_t is reduced to an identity matrix of size three.

The PF approximates PDFs via a set of particles with a total number of N called an ensemble $x_{t-1|t-1}$ and the associated weights w_{t-1}. Given the filtered distribution $p(x_{t-1}|y_{1:t-1})$ approximated at time $t-1$,

$$p(x_{t-1}|y_{1:t-1}) \approx \frac{1}{N}\sum_{i=1}^{N} w_{t-1}^{(i)} \delta(x_{t-1} - x_{t-1|t-1}^{(i)}) \tag{2.3}$$

The predicted distribution $p(x_t|y_{1:t-1})$ at a discrete time step t is computed with the prediction ensemble $x_{t|t-1}$, directly generated from the state model $f_t(x_{t-1|t-1}, \upsilon_t)$ using Eq. 2.4. δ is the Dirac delta function.

$$\begin{aligned} p(x_t|y_{1:t-1}) &= \int_{-\infty}^{\infty} p(x_t|x_{t-1}) p(x_{t-1}|y_{1:t-1}) dx_{t-1} \\ &\approx \sum_{i=1}^{N} w_{t-1}^{(i)} \delta(x_t - x_{t|t-1}^{(i)}) \end{aligned} \tag{2.4}$$

At last, the filtered distribution $p(x_t|y_{1:t})$ is obtaited from the predicted one $p(x_t|y_{1:t-1})$and y_t using the Bayes' theorem,

$$\begin{aligned} p(x_t|y_{1:t}) &= \frac{p(y_t|x_t) p(x_t|y_{1:t-1})}{p(y_t|y_{1:t-1})} \\ &= \sum_{i=1}^{N} \tilde{w}_t^{(i)} w_{t-1}^{(i)} \delta(x_t - x_{t|t-1}^{(i)}) \\ &= \sum_{i=1}^{N} w_t^{(i)} \delta(x_t - x_{t|t-1}^{(i)}) \end{aligned} \tag{2.5}$$

where $\tilde{w}_t^{(i)}$ is defined as

$$\tilde{w}_t^{(i)} = \frac{p(y_t|x_{t|t-1}^{(i)})}{\sum_j p(y_t|x_{t|t-1}^{(j)}) w_{t-1}^{(j)}} \tag{2.6}$$

If the observation system is linear, $p(y_t|x_{t|t-1})$ reads

$$p(y_t|x_{t|t-1}) = \frac{1}{(2\pi)^{m/2}|R_t|} \times \exp\{-\frac{[y_t - H_t(x_{t|t-1}^{(i)})]^T R_t^{-1}[y_t - H_t(x_{t|t-1}^{(i)})]}{2}\} \tag{2.7}$$

where m is the dimension of state vector, R_t is a predetermined covariance matrix for the observation error, and H_t is the matrix form of h_t. Each weight is updated with its previous value as follows.

$$w_t^{(i)} = \tilde{w}_t^{(i)} w_{t-1}^{(i)} \tag{2.8}$$

2.3 Parameter identification for DEM granular model

Because void ratio plays a significant role in the behavior of granular soil, a granular assembly with 0.68 void ratio is adopted for all simulations (N = 2000) in the Monte Carlo experiments. Nevertheless, the simulation results may still be affected by the number of elements even if same void ratio is ensured, because the fabrics in granular soil is better reproduced with large element number. Above all, the responses of the DEM model can be altered fundamentally by contact constitutive laws, which is also worth investigating for the PF. It is known that soil behavior is stress dependent, and thus sensitive to confining stress. Therefore, the ability of the PF in finding suitable parameters for different confining pressures is examined. All the scenarios considered are summarized in Table 2.1 where CL and HM stand for Cundall's linear (CL) and Hertz-Mindlin non-slip (HM) laws respectively. Both contacts have five micro parameters: (a) Young's modulus E, (b) Poisson's ratio υ, (c) rolling stiffness η, (d) rolling plastic limit ξ, and (e) contact friction angle μ Parameters that enable cohesion are not considered. Interested readers may refer to Šmilauer et al. [2015] for more details on contact laws and DEM background.

Table 2.1 Triaxial loading scenarios considered in the PF parameter identification

Confining pressure (MPa)	0.2		0.5, 1.0, 2.0, 4.0 and 8.0	
Number of spheres	CL	HM	CL	HM
1000	✓	✓	✓	✓
2000 and 5000	✓	✓		

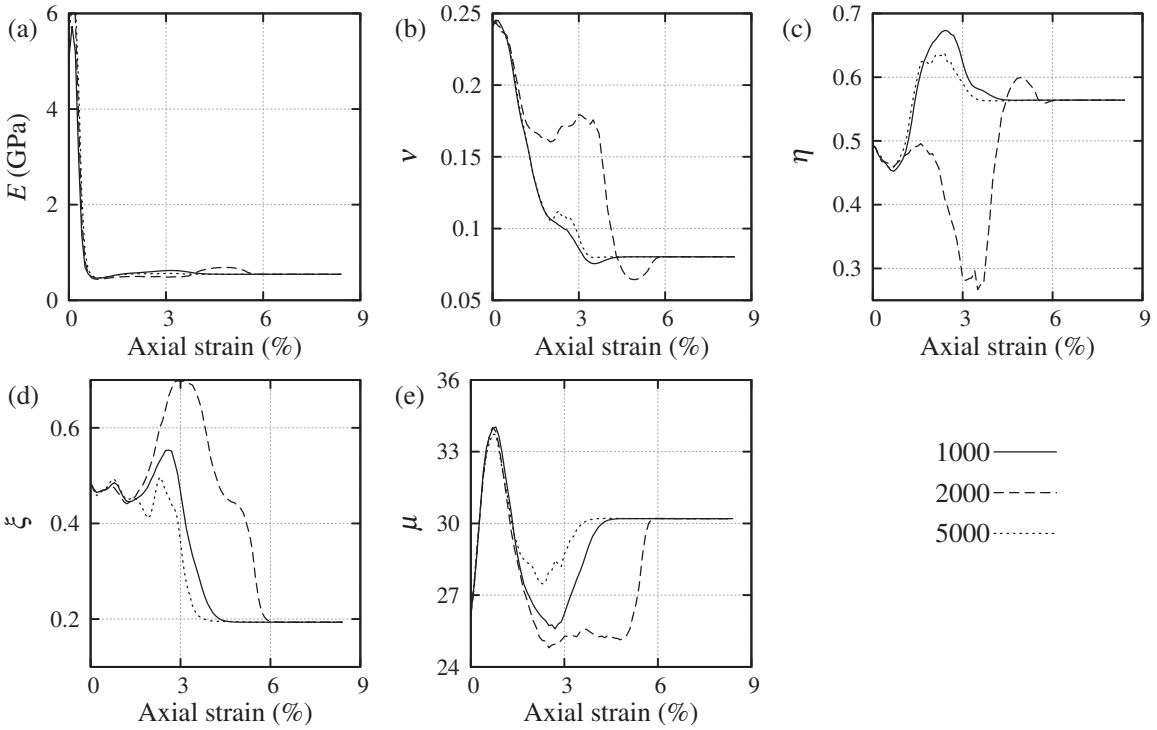

Fig. 2.1 Evolutions of weighted averages of parameters for Cundall's linear law identified by the particle filter.

2.4 Results and discussion

Fig. 2.1a–e show the evolutions of weighted parameters for the Cundall's linear law governed DEM model in axial strain-controlled triaxial compression. Solid, dashed and dotted lines represent the results reproduced by 1000, 2000 and 5000 numbers of elements. The weighted averages fluctuate at the small strain ranges, because the estimated posterior PDFs are updated very frequently from one simulation step to another. These initial fluctuations can be attributed to insignificant stress-strain responses at small deformation that are insufficient to differentiate for different particles in the data assimilation process. As the deformation increases until passing the characteristic mechanical states (e.g., volumetric strains changing from compressive to dilative, principal stress ratios reaching the peak), the weighted averages

and the posterior PDFs converge and the PF identifies a range of reasonable candidates for the micromechanical parameters of the DEM models with relatively large weights. It can also be understood from Fig. 2.1 that as long as the initial void ratio is ensured, the same weighted means are attained in the end, regardless of the number of discrete elements.

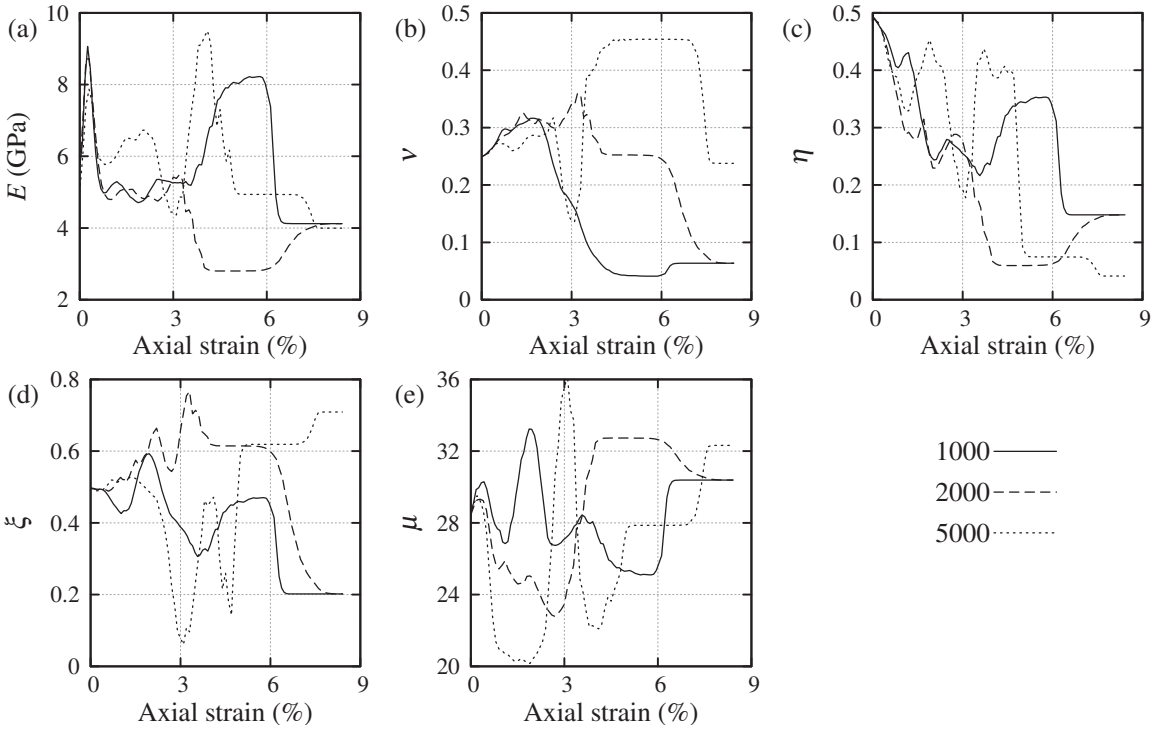

Fig. 2.2 Evolutions of weighted averages of parameters for Hertz-Mindlin non-slip law identified by the particle filter.

In the case of Hertz-Mindlin non-slip law as shown in Fig. 2.2, the weighted values converge similar to the case of the linear contact law, except for the 5000-element case. This could be attributed to the so-called degeneracy problem which results in a large weight upon a single particle. However, such difference has a negligible effect on the DEM simulations, because same weighted averages for E and μ are identified eventually. The initial fluctuations in Fig. 2.2 abide longer in comparison with those in Fig. 2.1, due to a complex force-displacement formulation of the Hertz-Mindlin non-slip law than that of the classical linear law.

The difference in identified parameters caused by confining pressure is studied with the 1000-element DEM model governed by Hertz-Mindlin non-slip law. As the confining pressure increases, the weighted mean of μ converged at 3–6% axial strain decreases as shown in

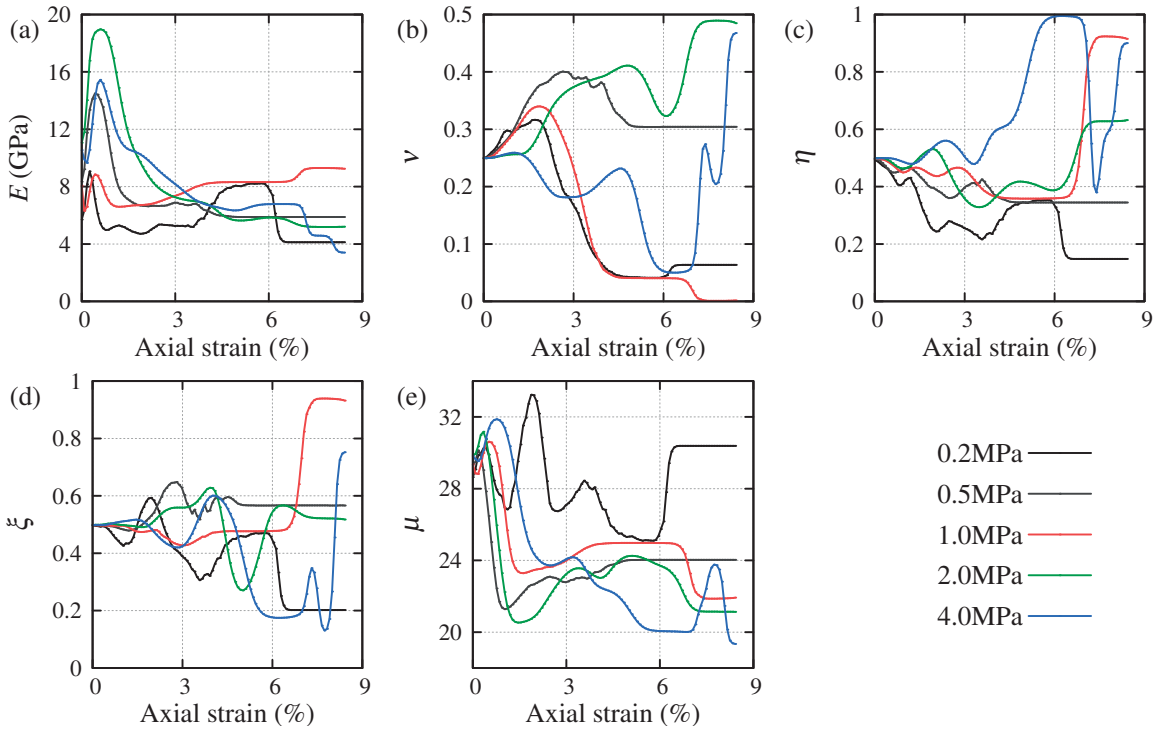

Fig. 2.3 Evolutions of weight parameters for different confining pressure cases.

Fig. 2.3. Whereas the tendencies are quite the opposite in the case of the converged means of E and η. Comparing the above findings with Fig. 2.4, one may find the trends of the micromechanical parameters μ, E and η very much resemble those of the dilatancy angle, macro Young's modulus and stress ratio. The predicted stress-strain responses in Fig. 2.4 are produced with the parameters identified at the stages where the weighted average and posterior PDFs become stagnant and have considered the previous loading history in the data assimilation. It can be observed the the predicted and measured stress-strain behaviors agree very well, except for that obtained under 4 MPa confining pressure. In this particular case, the Toyoura sand specimen in this triaxial compression test contracted monotonically, which can be explained by sand crushing under high confining pressures. In the current work, the crushability of discrete elements is not taken into account. Nevertheless, crushed granular soils can be easily simulated using bonded discrete elements like the agglomerate in Hanley et al. [2011].

Though this knowledge can be obtained by changing the values for one parameter while keeping the others constant. In this work it is acquired from a large set of numerical trials with the PF, which is both objective and efficient. In addition, the PF produces the PDFs of

the ensemble in the meantime, providing more information regarding possible values for the parameters.

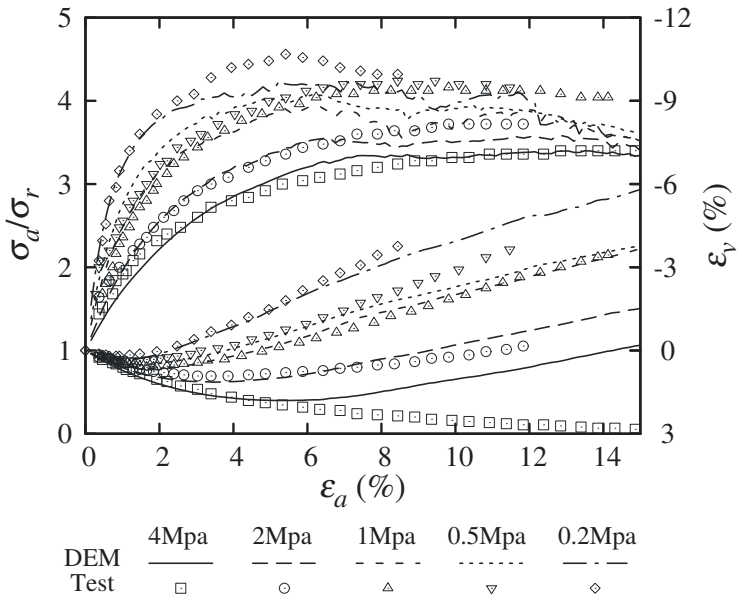

Fig. 2.4 DEM triaxial response using identified parameters.

2.5 Conclusions

This work employs a sequential data assimilation technique, i.e. the particle filter, in conjunction with Monte Carlo simulation of DEM sand specimens in triaxial compression conditions. True values for the micro parameters of Cundall's linear and Hertz-Mindlin contact laws are identified with high accuracy compared with experimental observation. Different confining stresses and numbers of discrete elements are considered to fully examine the capability of this approach. The variation of micro parameters with confining stress are found to be consistent with the macro ones. Because of the physical validity, the Hertz-Mindlin non-slip contact law and its relevant identified parameters are applied in the model validation against the experimental responses of geotextile-wrapped soil (Chapter 3) and in the DEM analyses of other geotextile-reinforced soils (Chapter 4 and 5). In order to reduce the computational cost in the coupled FEM/DEM methods (Chapter 6), the classical linear contact law is selected to govern the contact behaviors within the local representative volume elements and between soil and geosynthetic inclusions at the soil–geosynthetic interfaces.

References

Barrios, G. K. P., de Carvalho, R. M., Kwade, A., and Tavares, L. M. (2013). Contact parameter estimation for DEM simulation of iron ore pellet handling. *Powder Technology*, 248:84–93. pages 34

Belheine, N., Plassiard, J. P., Donzé, F. V., Darve, F., and Seridi, A. (2009). Numerical simulation of drained triaxial test using 3D discrete element modeling. *Computers and Geotechnics*, 36(1–2):320–331. pages 35

Bonilla-Sierra, V., Scholtès, L., Donzé, F. V., and Elmouttie, M. K. (2015). Rock slope stability analysis using photogrammetric data and DFN–DEM modelling. *Acta Geotechnica*, 10(4):497–511. pages 34

Breugnot, A., Lambert, S., Villard, P., and Gotteland, P. (2016). A Discrete/continuous coupled approach for modeling impacts on cellular geostructures. *Rock Mechanics and Rock Engineering*, 49(5):1831–1848. pages 33

Cheng, H., Yamamoto, H., and Thoeni, K. (2016). Numerical study on stress states and fabric anisotropies in soilbags using the DEM. *Computers and Geotechnics*, 76:170–183. pages 34

Coetzee, C. J. (2016). Calibration of the discrete element method and the effect of particle shape. *Powder Technology*, 297:50–70. pages 34, 35

Cundall, P. A. and Strack, O. D. L. (1979). A discrete numerical model for granular assemblies. *Géotechnique*, 29(1):47–65. pages 33, 34

EDEM 2.4 (2011). *Theory reference guide*. DEM Solutions, Edinburgh. pages 34

Evensen, G. (1994). Sequential data assimilation with a nonlinear quasi-geostrophic model using Monte Carlo methods to forecast error statistics. *Journal of Geophysical Research*, 99(C5):10143–10162. pages 36

Guo, N. and Zhao, J. (2013). The signature of shear-induced anisotropy in granular media. *Computers and Geotechnics*, 47:1–15. pages 34

Guo, N. and Zhao, J. (2016). 3D multiscale modeling of strain localization in granular media. *Computers and Geotechnics*. pages 33

Hadjidoukas, P. E., Angelikopoulos, P., Rossinelli, D., Alexeev, D., Papadimitriou, C., and Koumoutsakos, P. (2014). Bayesian uncertainty quantification and propagation for discrete element simulations of granular materials. *Computer Methods in Applied Mechanics and Engineering*, 282:218–238. pages 36

Hanley, K. J., O'Sullivan, C., Oliveira, J. C., Cronin, K., and Byrne, E. P. (2011). Application of Taguchi methods to DEM calibration of bonded agglomerates. *Powder Technology*, 210(3):230–240. pages 35, 42

Huang, W., Huang, L., Sheng, D., and Sloan, S. W. (2014). DEM modelling of shear localization in a plane Couette shear test of granular materials. *Acta Geotechnica*. pages 34

Itasca Consulting Group, I. (2014). PFC — Particle Flow Code. pages 34

Iwashita, K. and Oda, M. (1998). Rolling resistance at contacts in simulation of shear band development by DEM. *Journal of Engineering Mechanics*, 124(3):285–292. pages 34

Jiang, M. J., Yu, H.-S., and Harris, D. (2005). A novel discrete model for granular material incorporating rolling resistance. *Computers and Geotechnics*, 32(5):340–357. pages 34

Johnson, K. L. (1985). *Contact Mechanics*. pages 34

Johnstone, M. W. (2010). *Calibration of DEM models for granular materials using bulk physical tests*. PhD thesis. pages 35

Kawaguchi, T., Tanaka, T., and Tsuji, Y. (1998). Numerical simulation of two-dimensional fluidized beds using the discrete element method (comparison between the two- and three-dimensional models). *Powder Technology*, 96(2):129–138. pages 33

Kulatilake, P., Malama, B., and Wang, J. (2001). Physical and particle flow modeling of jointed rock block behavior under uniaxial loading. *International Journal of Rock Mechanics and Mining Sciences*, 38(5):641–657. pages 34

Li, X. and Yu, H.-S. (2013). On the stress–force–fabric relationship for granular materials. *International Journal of Solids and Structures*, 50(9):1285–1302. pages 34

Luding, S. (1998). Collisions & Contacts between two particles. *Physics of dry granular media - NATO ASI Series E350*, 1:285. pages 34

Luding, S. (2008). Cohesive, frictional powders: Contact models for tension. *Granular Matter*, 10:235–246. pages 34

Matsushima, T. and Blumenfeld, R. (2014). Universal structural characteristics of planar granular packs. *Physical review letters*, 112(9):098003. pages 34

Misra, A. and Yang, Y. (2010). Micromechanical model for cohesive materials based upon pseudo-granular structure. *International Journal of Solids and Structures*, 47(21):2970–2981. pages 33

Murakami, A., Shuku, T., Nishimura, S.-i., Fujisawa, K., and Nakamura, K. (2013). Data assimilation using the particle filter for identifying the elasto-plastic material properties of geomaterials. *International Journal for Numerical and Analytical Methods in Geomechanics*, 37(11):1642–1669. pages 36

Nakano, S., Ueno, G., and Higuchi, T. (2007). Merging particle filter for sequential data assimilation. *Nonlinear Processes in Geophysics*, 14:395–408. pages 36

O'Sullivan, C. (2011). *Particulate discrete element modelling: a geomechanics perspective*. Taylor & Francis, Hoboken, NJ. pages 33

Paulick, M., Morgeneyer, M., and Kwade, A. (2014). A new method for the determination of particle contact stiffness. *Granular Matter*, 17(1):83–93. pages 34

Plassiard, J.-P., Belheine, N., and Donzé, F.-V. (2009). A spherical discrete element model: calibration procedure and incremental response. *Granular Matter*, 11(5):293–306. pages 34, 35

Schofield, A. N. and Wroth, P. (1968). *Critical state soil mechanics*. McGraw-Hill, New York. pages 36

Shahin, G., Desrues, J., Dal Pont, S., Combe, G., and Argilaga, A. (2016). A study of the influence of REV variability in double scale FEM×DEM analysis. *International Journal for Numerical Methods in Engineering*, pages n/a–n/a. pages 33

Shuku, T., Murakami, A., Nishimura, S.-i., Fujisawa, K., and Nakamura, K. (2012). Parameter identification for Cam-clay model in partial loading model tests using the particle filter. *Soils and Foundations*, 52(2):279–298. pages 36

Šmilauer, V., Chareyre, B., Duriez, J., Eulitz, A., Gladky, A., Guo, N., Jakob, C., and Kozicki, J. (2015). Using and Programming. In Project, T. Y., editor, *Yade Documentation*. 2 edition. pages 36, 39

Soga, K. and Yimsiri, S. (2010). DEM analysis of soil fabric effects on behaviour of sand. *Géotechnique*, 60(6):483–495. pages 35

Stransky, J. and Jirasek, M. (2011). Calibration of particle-based models using cells with periodic boundary conditions. In *Particle-Based Methods Ii: Fundamentals and Applications*, number May 2016, pages 274–285. pages 33

Sun, D., Huang, W., Sheng, D., and Yamamoto, H. (2007). An elastoplastic model for granular materials exhibiting particle crushing. *Key Eng. Mater.*, 340-341:1273–1278. pages 37

Thoeni, K., Giacomini, A., Lambert, C., Sloan, S. W., and Carter, J. P. (2014). A 3D discrete element modelling approach for rockfall analysis with drapery systems. *International Journal of Rock Mechanics and Mining Sciences*, 68:107–119. pages 34

Thornton, C. (2000). Numerical simulations of deviatoric shear deformation of granular media. *Géotechnique*, 50(1)(1):43–53. pages 35

Thornton, C., Cummins, S. J., and Cleary, P. W. (2011). An investigation of the comparative behaviour of alternative contact force models during elastic collisions. *Powder Technology*, 210(3):189–197. pages 34

Thornton, C., Cummins, S. J., and Cleary, P. W. (2013). An investigation of the comparative behaviour of alternative contact force models during inelastic collisions. *Powder Technology*, 233:30–46. pages 34

Wan, R. and Guo, P. (2014). Microstructural formulation of stress dilatancy. *Comptes Rendus Mécanique*, 342(3):198–207. pages 34

Wang, Y. and Mora, P. (2008). Macroscopic elastic properties of regular lattices. *Journal of the Mechanics and Physics of Solids*, 56(12):3459–3474. pages 33

Wang, Y. and Tonon, F. (2010). Calibration of a discrete element model for intact rock up to its peak strength. *International Journal for Numerical and Analytical Methods in Geomechanics*, 34(5):447–469. pages 34

Yimsiri, S. and Soga, K. (2011). Effects of soil fabric on behaviors of granular soils: Microscopic modeling. *Computers and Geotechnics*, 38(7):861–874. pages 34

Yoon, J. (2007). Application of experimental design and optimization to PFC model calibration in uniaxial compression simulation. *International Journal of Rock Mechanics and Mining Sciences*, 44(6):871–889. pages 35, 36

Zhang, Y. B., Medina-Cedina, Z., and Khoa, H. D. V. (2011). Probabilistic calibration of a discrete particle model for geomaterials. In *Geo-Frontiers 2011: Advances in Geotechnical Engineering*, pages 4204–4213. pages 36

Zhao, J. and Guo, N. (2013). Unique critical state characteristics in granular media considering fabric anisotropy. *Géotechnique*, 8(8):695–704. pages 34

Chapter 3

Discrete Element Modeling of Geosynthetic-Wrapped Granular Soil

3.1 Introduction

The knowledge of geotechnical engineering has been tested and advanced by the increasing need for countermeasures against ground disasters, such as earthquakes, slope failures and landslides. However, the growing awareness of sustainable development demands cost-effective and environmentally friendly solutions to geotechnical engineering problems. In recent decades, geosynthetic-reinforced soil (GRS), e.g., geotextile sheets for soil nailing in retaining walls, has manifested itself as one of the most effective earth/subgrade reinforcement methods that addresses both concerns [Bhandari and Han, 2010; Cai and Bathurst, 1995; Chen et al., 2014; Indraratna and Nimbalkar, 2013; Tatsuoka et al., 1997]. Instead of being layered by planar geosynthetic sheets, wrapping soils entirely in geosynthetic containers, such as soilbags [Lohani et al., 2006; Matsuoka and Liu, 2003], results in an astonishing rise in the bearing capacity by utilizing the straining geosynthetic fabrics that inhibit the dilatancy of the soil. Regardless of the different ways that geosynthetic is included in the ground, the GRS is fabricated to be more heterogeneous than natural soils. Due to the discontinuity and anisotropy at the interface between soil and geosynthetic, it is difficult to conduct a

comprehensive evaluation on the performance and mechanisms of the GRS from the onset of the external load until the global/local failure of the geosynthetic reinforcement using a conventional continuum approach. The design of the GRS as a road/railway subgrade or foundation reinforcement is mainly based on laboratory testing and empirical assumptions. Hence, the development of efficient numerical tools to model GRS of various forms and types is still urgently needed.

In most cases, geosynthetic sheets are layered in soil to form planar reinforcement on road foundations or retaining structures. GRS does not typically come in the form of soilbags[1]; nevertheless, its engineering values should not be underestimated. For economical, technical and sustainable reasons, soilbags have reclaimed their role as a permanent element in earth reinforcement [Matsuoka and Liu, 2006]. Based on years of laboratory tests and engineering experience [Liu et al., 2014; Lohani et al., 2006; Matsuoka and Liu, 2003; Matsuoka et al., 2010; Xu et al., 2008] soilbag earth reinforcement has been found to be able to:

1. improve the bearing capacity of a soft foundation by five to ten times,
2. provide high compressive strength by wrapping soils of various types inside,
3. dissipate energy under traffic and seismic vibration, and
4. prevent frost heaving if broken stones are used to fill the inside.

Matsuoka and Liu [2006] proposed a simplified analytical solution for the compressive strength of soilbags in plain strain conditions, introducing an apparent cohesion c based on the assumption of uniformly distributed tension and a frictionless soil–geosynthetic interface. The idea was later extended to predict compressive deformation by considering the evolution of tension and the principal stress ratio. Since then, several attempts have been made to model the soilbag using truss elements for modeling the tensile behavior of the geosynthetic fabric. The performance of soilbag reinforcement was examined at different scales, ranging from the soilbag-assembly level [Muramatsu et al., 2009] to the soil–geotextile interface level [Tantono and Bauer, 2008].

[1]The term “soilbag” refers to soils that are entirely wrapped by a geosynthetic container as a whole

Muramatsu et al. [2009] validated the capability of a 2D finite element (FE) model to analyze the settlement of soilbag foundations under vertical load in a finite deformation scheme. To attain better control of the settlement, multiple small soilbags stacked together as an assembly are preferable to one large soilbag because the tension on the small bag is fully developed and the dilatancy of the soil is better constrained. This is part of the reason why small-sized soilbags are used in the present study. Tantono and Bauer [2008] adopted the micro-polar hypoplastic model to discuss the effect of the soil–geotextile interface (slip/rotation) on stress and strain in the wrapped GRS in a soilbag. They based the interface modeling on a master/slave surface concept and discovered that a frictionless interface leads to slightly higher bearing capacity and lower stress concentration in the middle of the GRS. Ansari et al. [2011] extended this concept in their 3D FE model, which allows for the consideration of large interfacial slips, surface separation and reclosure. Interfacial discontinuity and large deformation can be effectively addressed by implementing this concept in an FE scheme, but they can be better handled with discrete approaches such as the discrete element method (DEM).

A large amount of numerical modeling of the GRS (e.g., geotextile, geogrid) has been conducted using the DEM [Bhandari and Han, 2010; Chen et al., 2012; Han et al., 2012] and proper coupling between the DEM and other methods [Ahmed et al., 2015; Chareyre and Villard, 2005]. Nevertheless, discrete element modeling of GRS wrapped in a geosynthetic soilbag is relatively new. In this work, a woven geotextile was considered as the wrapping material of the soilbag. Its fabric has peculiar mechanical behaviors because of the easy relative motion between the yarns, fabric abrasion and impregnation (with, e.g., resin matrix) [Boubaker et al., 2007]. The structural mechanics of this woven system can be accurately represented by orthogonal bars with nodes linked by diagonal and rotational springs. A simplified modeling of the wire mesh was initiated by Thoeni et al. [2014, 2013] using the DEM, considering only the stretching springs with a stochastically distorted law that accounts for the initial distortion of the hexagonal steel wire meshes. The approach generally suits any woven system. In the present modeling, the discretization of the woven geotextile fabric was performed in a similar manner.

In this chapter, a novel approach for the discrete modeling of a soilbag is presented to investigate the stress state and fabric anisotropies of the wrapped GRS. The granular soil, which fills a polyethylene (PE) or polypropylene (PP) geotextile container, was fabricated by performing a 3D–assembling–filtering–expanding process using a well-calibrated DEM representative volume (RV) of Toyoura sand. The macroscopic behaviors of the materials and the interface were calibrated against laboratory test data. The proposed DEM soilbag model was validated with the responses of a soilbag in unconfined compression (UC) and simple shear (SS). Aside from reproducing the results of previous experimental [Cheng et al., 2013; Yamamoto and Cheng, 2012] and numerical [Ansari et al., 2011; Muramatsu et al., 2009; Tantono and Bauer, 2008] studies, the discrete approach is capable of capturing the macroscopic constitutive behavior of wrapped GRS due to discontinuous composition and interaction forces among particles while exploring the microscopic characteristics of this complex geomaterial. The evolutions of local/global stress paths and fabric anisotropies of wrapped GRS were investigated to clarify the reinforcement mechanisms of a soilbag; i.e., confinement and interlocking. This numerical study is conducted using the open-source DEM framework YADE [Šmilauer et al., 2015].

3.2 Discrete modeling of a soilbag

The numerical modeling of a soilbag must address both discontinuities in the particles and the anisotropy and heterogeneity caused by the inclusion of a geotextile. These problems can be solved by discretizing geotextile-wrapped GRS as an assembly of polydispersed particles that are capable of transferring loads and becoming mobilized by sliding and rolling/twisting. Generation of the assembly was handled with care to ensure that the macro response of Toyoura sand was sufficiently replicated in the simulation. In this model, the particles representing the woven fabric were positioned on the 3D orthogonal mesh of the container (Fig. 3.1a). These particles are connected with remote springs that sustain tension, and their rotational degrees of freedom are blocked. With accessible information about compressing, sliding, rolling/twisting and stretching among particles at the local scale,

the discrete approach can provide a microscopic description of wrapped GRS, e.g., fabric anisotropy and coordination number.

The DEM simulates these local behaviors in a rigorous manner. At the local scale, inter-particle forces are computed from detected overlaps, i.e., the distance between neighboring particles, using simple force-displacement laws. After computing the resultant forces applied on each particle, the dynamic response of the granular system is solved numerically through Newton's second law in a time-marching scheme. As a result, the material is discretized with calculations of the kinematics of each constituent particle, which renders this approach very suitable to model discontinuous behaviors, such as the separation between soil and a geotextile, the breakage of yarn and the rupture of woven fabric. In YADE, this integration scheme is implemented using an explicit finite difference algorithm that considers constant velocities and accelerations at each time step. As detailed in Šmilauer et al. [2015], global non-viscous damping is usually adopted for reducing the fluctuation of a response. In this study, a damping coefficient of 0.2 is chosen and no gravitational field is employed in order to maintain symmetry in the simulations.

3.2.1 Geometrical assumption of a woven geotextile container

In previous experimental studies [Cheng et al., 2013; Yamamoto and Cheng, 2012], each geotextile container was filled with 235.2 N Toyoura sand. The sand was thoroughly compacted until a target height of approximately 80 mm was attained for each soilbag. The container had a curved lateral surface and four slightly tightened corners (Fig. 3.1b). Given the initial cuboidal shape of the geotextile container (length and width of 400 m, height of 100 mm) and the target height for the initial compaction, the cross-sections of the soilbag perpendicular to the short and long axes after the compaction were assumed, as shown in Fig. 3.1c. From these cross-sections, the 3D geometry of the container was constructed (Fig. 3.1a). On the 3D mesh, the geotextile was discretized using discrete nodes (r = 2.5 mm), with a regular mesh size of 5 mm $\times$ 5 mm. Note that the volume of the 3D geometry is 0.015 m3. If the inside

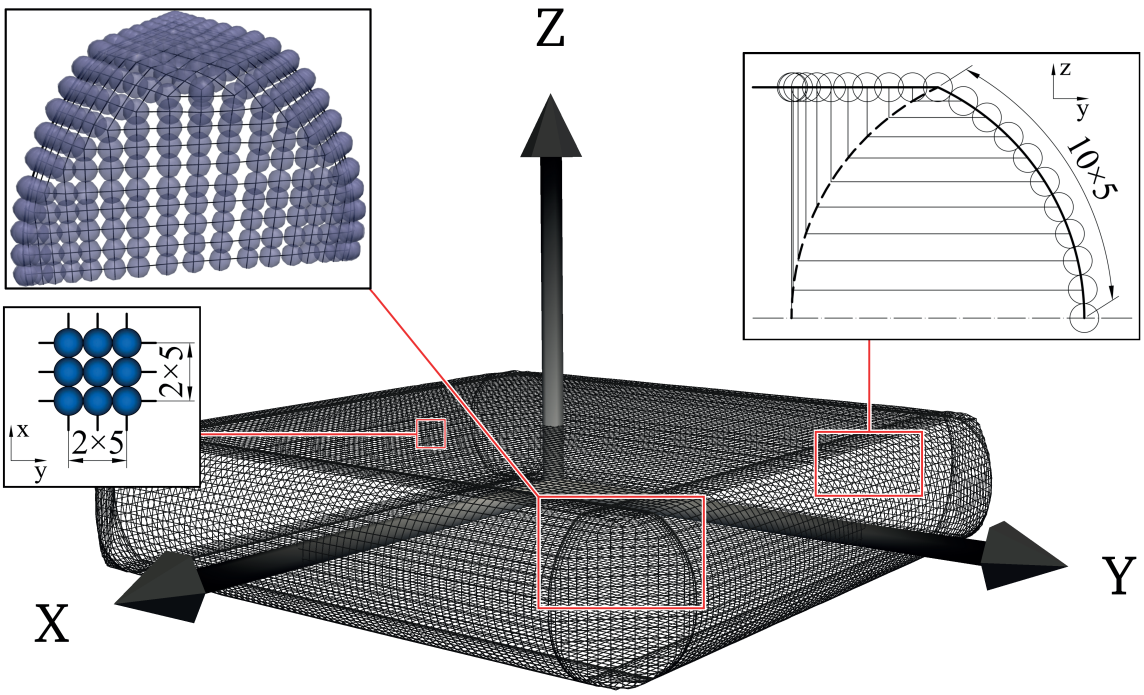

(a)

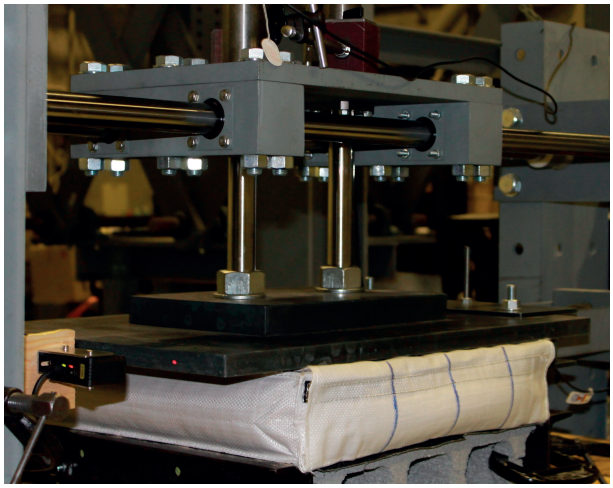

(b)

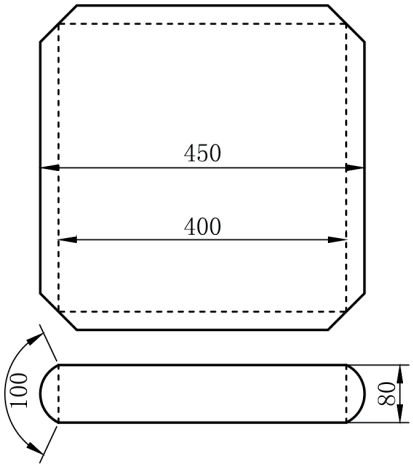

(c)

Fig. 3.1 (a) Discretization of the woven geotextile container, (b) representative laboratory soilbag after initial compaction, and (c) assumed cross-sections with dimensions of mm.

soil weighs 235.2 N, the initial void ratio of the wrapped GRS after the initial compaction is approximately 0.68.

3.2.2 Determination of the local parameters

The materials modeled using the DEM are typically calibrated against their macroscopic responses in the laboratory. The results from triaxial or biaxial tests on soil specimens for different confining pressures are commonly compared with the results from the DEM models. In this study, the contact constitutive behaviors of two interacting particles are described by the two nonlinear springs k_n and k_s, which relate the normal force $\boldsymbol{F}_n$ to the overlap $\boldsymbol{u}_n$ and the shear force increment $\mathrm{d}\boldsymbol{F}_s$ to the relative shear velocity $\dot{\boldsymbol{u}}_s$ and the time increment $\mathrm{d}t$, respectively, as shown in Eq. 3.1. The stiffness values of the springs are defined using Eq. 3.2 from the simplified Hertz–Mindlin non-slip contact law [Thornton et al., 2011]. The shear force is limited by the inter-particle friction angle φ according to the Mohr-Coulomb criterion (i.e., $F_s \leqslant \tan\varphi F_n$).

$$\boldsymbol{F}_n = k_n \boldsymbol{u}_n \quad \text{and} \quad \mathrm{d}\boldsymbol{F}_s = k_s \dot{\boldsymbol{u}}_s \mathrm{d}t \tag{3.1}$$

$$k_n = 2E^* \sqrt{r^* u_n} \quad \text{and} \quad k_s = 8G^* \sqrt{r^* u_n} \tag{3.2}$$

where $r^* = 1/(1/\boldsymbol{r_1} + 1/\boldsymbol{r_2})$ is the equivalent particle radius; $\boldsymbol{r_1}$ and $\boldsymbol{r_2}$ are the radii of two contacting particles. The equivalent effective Young's modulus E^* and the shear modulus G^* are respectively expressed as

$$E^* = \frac{1}{\frac{1-\upsilon_1^2}{E_1} + \frac{1-\upsilon_2^2}{E_2}} \quad \text{and} \quad G^* = \frac{1}{\frac{2-\upsilon_1}{G_1} + \frac{2-\upsilon_2}{G_2}} \tag{3.3}$$

where E_i and υ_i (i = 1, 2) are the Young's moduli and the Poisson's ratios of the contacting particle i, and the shear modulus G_i is related to E_i and υ_i by $G_i = E_i/2(1+\upsilon_i)$.

The moment transfer law $\boldsymbol{M} = k_m \boldsymbol{\theta}$ for the relation between the moment and the rotation on the contact surface was considered to adequately reproduce the peak stress ratio of the

soil. However, the plastic limit for the contact moment $\boldsymbol{M}$ in [Oda, 1972] was omitted due to its negligible effect when the value for k_m is set. Both contact laws are available in YADE [Modenese, 2013].

The tensile constitutive laws of PE and PP geotextiles were acquired from the wide-width tensile tests and represented by nonlinear remote springs in the DEM [Thoeni et al., 2013]. For the interactions between soil particles and geotextile nodes, the simplified Hertz–Mindlin contact law and the moment transfer law were employed; however, the parameters in this case differed, based on the calibration against shear box test results.

Sand

The Toyoura sand inside the container is uniformly graded ($D60/D10 = 1.3$) with the average radius $\tilde{r} = 0.1$ mm and the specific gravity G_s = 2.65. To calibrate the contact model such that the resulting macro response replicates the sand response in similar loading conditions, a cuboid DEM packing that consists of 1000 particles with a scaled particle-size distribution (PSD) ($\tilde{r} = 3$ mm, G_s = 2.65) was loaded in triaxial compression with periodic boundary condition (PBC). To attain an initial void ratio (e_0 = 0.68) which is identical to the initial void ratios of the cylindrical triaxial specimens of Toyoura sand (diameter of 50 mm and height of 100 mm) [Sun et al., 2007], a cloud of particles that were randomly generated in a periodic cell (50 mm $\times$ 50 mm $\times$ 100 mm) underwent an isotropic pressure of 0.1 MPa, followed by periodic reduction of the inter-particle friction angle when equilibrium was attained. The iterative process stopped when e_0 approximated 0.68. The contact orientation diagram and the coordination number of the resulting cuboidal DEM particle assembly (46.2 mm $\times$ 46.2 mm $\times$ 92.4 mm) prior to loading are shown in Fig. 3.2a.

Different levels of isotropic compression were applied before the triaxial loading. Fig. 3.2b compares the macro responses of the DEM packing and the Toyoura sand specimen in drained triaxial compression. The local behaviors of the DEM packing were defined using the parameters in Table 3.1. Because the initial void ratio of the wrapped GRS is 0.68 as well, the

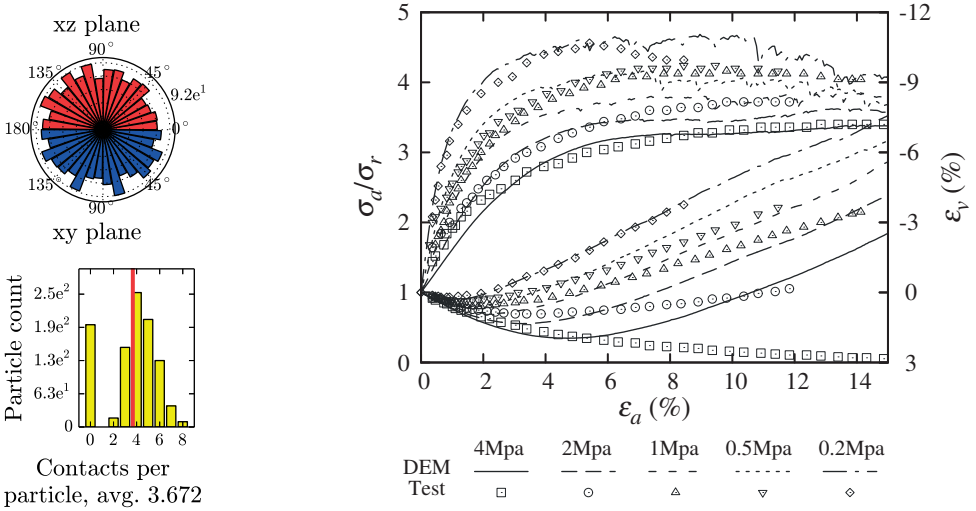

Fig. 3.2 (a) Contact orientation diagram and coordination number of the particle assembly prior to loading, and (b) response in drained triaxial compression compared with test data of Toyoura sand.

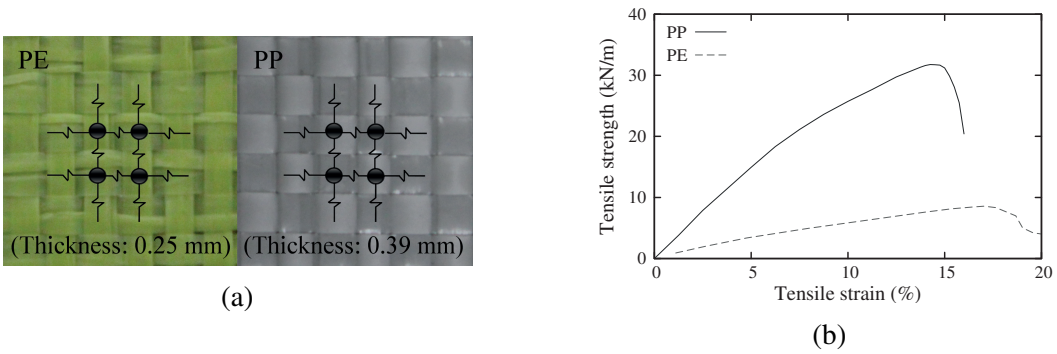

Fig. 3.3 Characteristics of PE and PP woven geotextiles: (a) woven fabric structure and (b) tensile behavior.

Table 3.1 Micro-parameters for Hertz–Mindlin contact model.

	Young's modulus (GPa)	Poisson's ratio	Rolling/twisting stiffness (N·m/rad)	Scaled density (10^3kg/m^3)	Inter-particle friction angle (°)
Soil	4	0.33	0.13	2650	29
Geotextile	8	0.33	0.13	444	PP: 21 and PE: 25
Plate	200	0.33	0.13	7850	UC: 0 and SS: 90

same initial DEM packing ($e_0 = 0.68$) which was used for contact model calibration can be employed as the RVs to generate the GRS packing inside the soilbag.

Geotextile

The discrete modeling of woven textiles considers the fabric as a collection of orthogonal yarns, giving insights into the contribution of yarn properties and fabric organization to the macro behavior [Boubaker et al., 2007]. The main objective of th current geotextile modeling is to investigate the dry interactions of the woven fabric with soil. Therefore, the woven fabric was modeled at a scale at which the fabric's structural mechanics can be described. This was done by linking the physical nodes where the warp and the weft meet with remote springs, as shown in Fig. 3.3a. Because the fabric was constantly strained with great tensile force in both the warp and the weft in either a UC or SS condition. Sliding was not introduced at the intersections of the warp and the weft and the rotation of the particles that represent the geotextile was prohibited.

Although there is some degree of irregularity in yarn properties and fabric organization, the stochastically distorted shift of the force-displacement curve as formulated in Thoeni et al. [2013] was not considered. Instead, the tensile behavior was solely governed by the curves in Fig. 3.3b, which were converted to the tensile stress-strain relations considering the fabric thickness and approximated by a piece-wise linear function. Based on the discretization in Fig. 3.1a, each remote spring is assumed to have the same cross-sectional area (PE: 5 mm $\times$ 0.25 mm or PP: 5 mm $\times$ 0.39 mm).

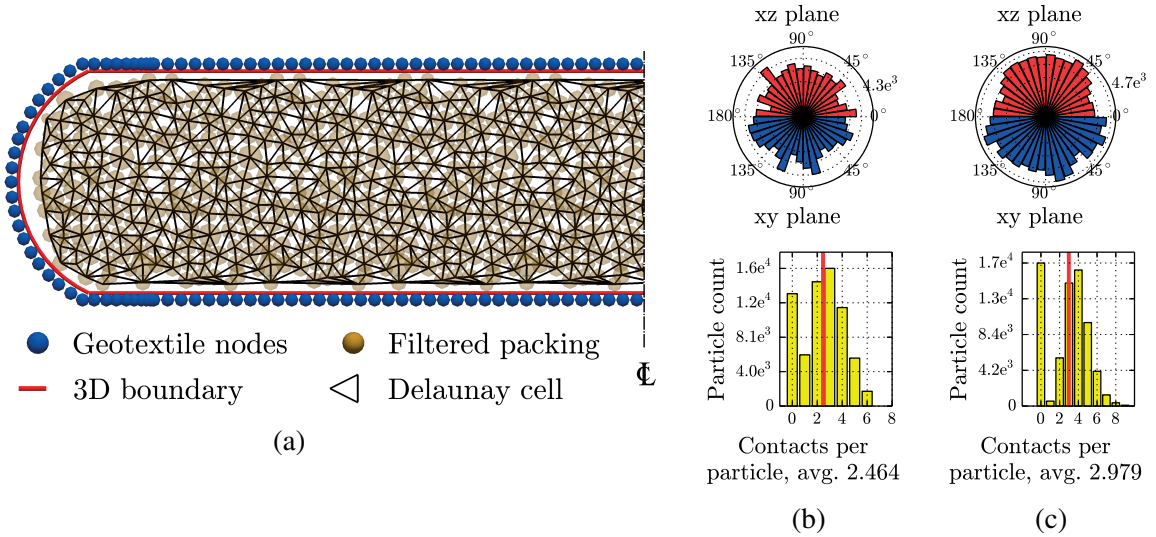

Fig. 3.4 (a) Components that represent the wrapped GRS in the central x–z plane, and corresponding contact orientation diagram and coordination number (b) before and (c) after radius expansion.

Interface between sand and geotextile

The soil–geotextile interfacial behavior, which can be affected by apertures and undulations of the geotextile, is simply considered to be the roughness that is introduced from the topography of the linked geotextile nodes in the discrete model (blue spheres in Fig. 3.4a). The interface response was calibrated by shearing a sandbox (100 mm $\times$ 100 mm $\times$ 6 mm) on a fixed PE/PP geotextile sheet (200 mm $\times$ 200 mm). Friction on the bottom and inner surfaces of the sidewalls were excluded by using double-layered Teflon films with silicone grease lubrication. The same boundary conditions were set for the soil spheres within the shear box in the simulations. Fig. 3.5a displays a schematic view of a shear box simulation. The best agreement with the experimental data was obtained with the interface friction angles 25°and 21°for the PE sheet and the PP sheet, respectively (Fig. 3.5b). A detailed explanation on the calibration process is provided in Cheng and Yamamoto [2015, 2016].

3.2.3 Generation of geotextile-wrapped GRS

With the closed 3D boundary properly defined in Fig. 3.1a, the inside can be easily filled with a DEM packing, whose constituent particles expand in radii only when equilibrium is attained

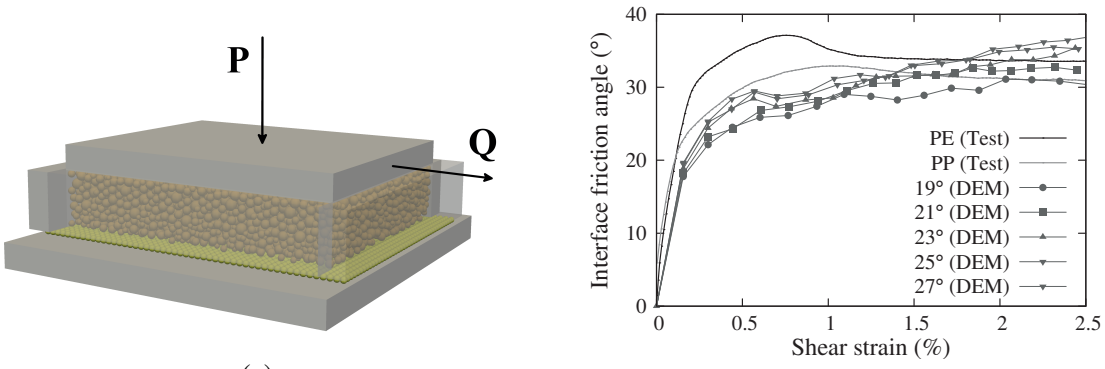

(a) (b)

Fig. 3.5 (a) Schematic of the shear box simulation and (b) interfacial response in experimental tests and simulations with different soil–geotextile interface friction angles.

[O'Sullivan, 2011]. The primary concern is preserving a fabric structure that is equivalent to the fabric structure of the wrapped Toyoura sand after the initial compaction in the tests. The void ratio is the most conventional and convenient indicator to describe the fabric structure of an isotropic specimen and is also of great significance in classical soil models. Hence, a packing generation process in which a void-ratio-specified DEM packing gradually grows is applied. Thereby, the particles become geometrically compatible to the 3D boundary in the end without inducing excessive internal forces.

To generate a packing with a particular void ratio, the initial DEM packing ($e_0 = 0.68$) in Section 3.2.2 was used as the RVs to construct the geotextile-wrapped GRS packing. Because of the compatible contacts along the boundaries of neighboring RVs, the assembled cuboid-shaped packing with 100 RV duplicates (10 along the x-axis and 10 along the y-axis) has intrinsic fabric consistency. Because the response of the DEM packing used as RVs was calibrated against a series of triaxial tests (although not precisely for volumetric strain at high confining pressure), the cuboid-shaped packing is deemed capable of quantitatively reproducing the macro response of the wrapped Toyoura sand while shedding some light on the fabric characteristics of a soilbag in given loading courses.

The cuboid-shaped packing was filtered to satisfy the 3D soilbag boundary (red envelope in Fig. 3.4a). An illustration of the components representing the wrapped GRS on the central cross-sectional plane before the radius expansion is given in Fig. 3.4a. As shown in Fig. 3.4b, the contact orientation diagram and the contact number histogram of the wrapped GRS are

similar to those for the RV in Fig. 3.2a. However, the coordination number in Fig. 3.2a is slightly bigger. This is because the RV is in periodic boundary condition, whereas the wrapped GRS has no contacts supporting its boundary, as shown in Fig. 3.4a.

To ensure that the filtered packing sufficiently conformed to the boundary, the sphere radii of the soil particles were multiplied by the small factor $\alpha = 1.0001$. A number of DEM calculation cycles were performed to dissipate the disturbances caused by the radius expansion in order to ensure that the packing regains equilibrium after the radius expansion (the ratio of the mean unbalanced force on the particles to the mean force on the interactions is less than 10^{-3}). To prevent the particles from significantly deviating from their original positions, the system was given a global damping coefficient of 0.9 during the DEM cycles. This process, which is classified as"dynamic specimen generation" [O'Sullivan, 2011], repeats until the total volume of the Delaunay cells of the packing (note that the triangles shown in Fig. 3.4a are actually tetrahedrons as this is done in 3D) ceased to grow and the mean overlap ratio decreased to 2.0×10^{-8} (the same level as for the RV in Section 3.2.2).

Fig. 3.4c shows the contact orientation diagram and coordination number after the radius expansion. The coordination number of the wrapped GRS packing is 2.979, which is slightly smaller than the coordination number of the RV (Fig. 3.2a) due to the convex boundary of identical spheres. Nevertheless, consistent shapes of the contact orientation diagrams and contact number histograms of these two particle systems can be observed. Fig. 3.2a, Fig. 3.4b and c demonstrate that the fabric characteristics of the original RV were well preserved throughout this 3D–assembling–filtering–expanding process. The filtered packing that contains 68,883 spheres attained a void ratio of 0.675. Because the geotextile nodes (blue spheres in Fig. 3.4a) were fixed during this process, the produced packing is equally applicable for the PE and PP geotextile cases. It should be noted that the void ratio of the RV is computed using the volume of the periodic cell. Analogously, the void ratio of the packing is evaluated from the total volume of the Delaunay cells.

3.2.4 Particle-based stress tensor

The particle-based stress tensor can be computed as

$$\boldsymbol{\sigma}^c = \frac{1}{V}\sum_{N_c} \boldsymbol{d}^c \otimes \boldsymbol{f}^c \tag{3.4}$$

where $\boldsymbol{\sigma}^c$ is the bulk stress tensor, N_c denotes the number of considered contacts on a particle, V is the volume of the Voronoi cell occupied by the particle, and $\boldsymbol{d}^c$ and $\boldsymbol{f}^c$ are the corresponding branch vector and force vector, respectively, of the contacts [Guo and Zhao, 2013]. By weighting the micro-tensors $\boldsymbol{\sigma}^c$ over the preferred domains, one can easily acquire the relevant global/local macro stress tensor as well as the mean stress p and deviatoric stress q. Because the soilbag packing is derived from the original RV packing in the PBC cell, it is reasonable to base the local p and q values on these RV duplicates. The stress components in Figs. 3.7, 3.8, 3.10, 3.11 and 3.16 are computed in such an averaged manner.

3.3 Results and discussion

3.3.1 Validation of the soilbag model

The macro responses obtained from the UC and SS tests were used to validate the proposed DEM soilbag model. In the UC test, a triple-layered PE soilbag stack was compressed vertically using a large steel loading plate at a constant compressive strain rate of 0.1%/s. In the SS tests, a single-layered PP soilbag was sheared at a shear strain rate of 0.02%/s with a constant vertical dead load P of 1.33, 1.87, and 2.41 kN. Abrasive paper (grit 40) was firmly attached to the bottom of the loading plate and the top of the test platform to minimize the interface sliding, but the effect became marginal at high levels of vertical load during the UC test. This can be understood from the similar failure modes (fabric rupture in the middle) in the test (Fig. 3.6a) and the simulation with a 0°geotextile–plate interface friction angle (Figs. 3.6b). When a friction angle of 90°is used (an extreme case to eliminate sliding), the fabric ruptures along the seams (Figs. 3.6c), which differs significantly from the experimental

Table 3.2 Setup of simulations and tests for model validation.

		Strain rate	Num. of soilbags	Initial compaction	Geotextile-plate interface	Geotextile type
Test	UC	0.1%/s	Three	With	Sandpaper (grit 40)	PE
	SS	0.02%/s	One	With	Sandpaper (grit 40)	PP
Simulation	UC	10%/s + Stress increment	One	Without	Smooth (0°)	PE
	SS	10%/s	One	With	Fixed (90°)	PP

observation (Figs. 3.6a). In addition, introducing friction on the geotextile–plate interface will affect the confinement of the wrapped GRS. Therefore, the UC simulations excluded such interfacial friction. In the SS simulation, however, the geotextile–plate contacts were given a 90° friction angle to eliminate the interfacial sliding. During initial vertical loading prior to shear, a friction angle of 0° was applied at the interface. To reduce the computational costs, only one soilbag was modeled in the simulations and density scaling [Thornton, 2000] was applied according to Table 3.1. The initial compaction process was left out because its effect on the initial void ratio has been considered by the assumed 3D geometry, as stated in Section 3.2.1. The strain rate was held constant at 10%/s in both the UC and SS simulations. Although not shown here, a consistent macro response was obtained with strain rates of 1%/s and 0.1%/s. The UC simulations were incrementally conducted; each step was completed when the soilbag attained a quasi-static state with a negligible level of unbalanced force ratio (10^{-3} as in Ng [34]) and kinetic energy (lower than 10^{-5} J). The setups of the simulations and the tests for model validation are given in Table 3.2.

Good agreement was observed between the responses in the tests and the simulations with the parameters given in Table 3.1 (see Fig. 3.7 for the UC case and Fig. 3.8 for the SS case). Fig. 3.7 provides the evolutions of the external axial stress on the soilbag σ_a and the z component of the average stress tensor $\boldsymbol{\sigma}$ over the GRS domain σ_z using Eq. 3.4. Because the soilbag was continuously flattened, σ_a' calculated as P over the reference top surface area of the soilbag ($A = 0.16\text{m}^2$) is not accurate. The true value was computed in a manner similar to σ_z, except that the averaging took place over the whole soilbag domain. Nevertheless, the

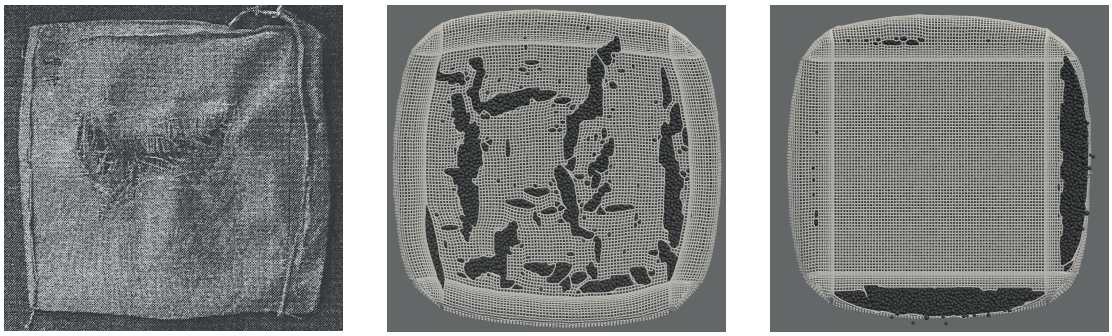

(a) (b) (c)

Fig. 3.6 Failure modes in (a) test and simulations with (b) 0° and (c) 90° interface friction angle for geotextile–plate contacts.

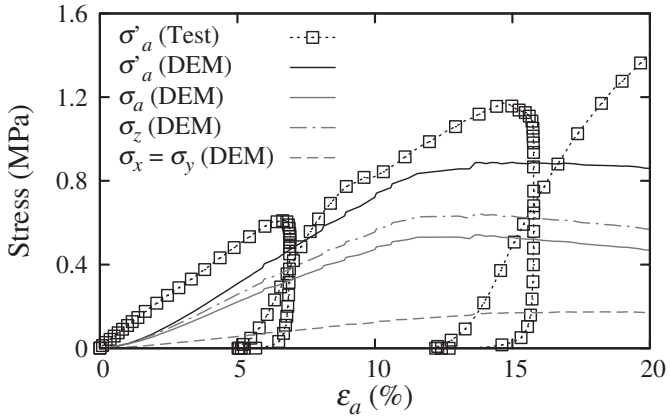

Fig. 3.7 Stress-strain relationship of a PE soilbag in UC test (partially cyclic) and simulation.

stress $\sigma_a' = P/A$ is plotted for direct comparison between test and simulation responses. σ_z constantly exceeds σ_a due to the additional confining stress on the wrapped GRS from the sustained tension on the geotextile. After the soilbag attained global failure in UC at the axial strain $\varepsilon_a \approx 13\%$, both σ_z and σ_a began to decrease while the level of the lateral stress σ_x and σ_y remained stationary due to the interlocking force between the soil particles and geotextile nodes. In the test, however, the PE soilbag did not fail in the ε_a range considered. Such difference in bearing capacity can be attributed to the relatively large radii of the geotextile nodes in the simulation (r_{bag} = 2.5 mm, 10 times the PE geotextile thickness). When the fabric ruptured as illustrated in Fig. 3.6b, large interconnecting openings are formed with soil particles consistently being shoved into them. As a result, the GRS volume expanded with a gradual decline in stress level (see Fig. 3.10c). The first local constituent yarn broke at ε_a = 8% in the simulation. An additional 5% was required for the breakages to develop into full openings and the stress in the GRS to reach the peak. In the test, given the thin PE geotextile, more strain would be required for global failure to occur. The initial toe region of the stress-strain relationship in Fig. 3.7 was another difference between the simulation and test, possibly due to the lack of initial compaction. As suggested by O'Sullivan et al. [2008], cyclic loading (initial compaction) rearranges the strong force chains to be more anisotropic, which causes hardening of the granular material. Previous experiments have also found that the initial stiffness of soilbags improved with thorough initial compaction.

Furthermore, because of the absence of compaction in the numerical model, the maximum normal strain ε_a was reproduced higher in the SS simulations than in the tests, but the evolution of the stress ratio τ/σ_a (τ is computed as shear force Q over A) matches the test data well (see Fig. 3.8). Fig. 3.8 also provides the evolution of the shear-to-tangential stress ratio τ_{zx}/σ_z on the x–y plane of the wrapped GRS using Eq. 3.4. τ_{zx}/σ_z was found to fall progressively behind τ/σ_a' due to the increasing σ_z in the GRS (see Fig. 3.16) because of the enhancing confinement from the wrapping geotextile. As would be expected, both the stress ratios and axial strain decrease accordingly with greater vertical load. It should be noted that at the lowest vertical load level (Q = 1.33 kN) the stress-strain response of the wrapped soil is unstable particularly after the contractive-to-dilative transition of the volumetric strain. This

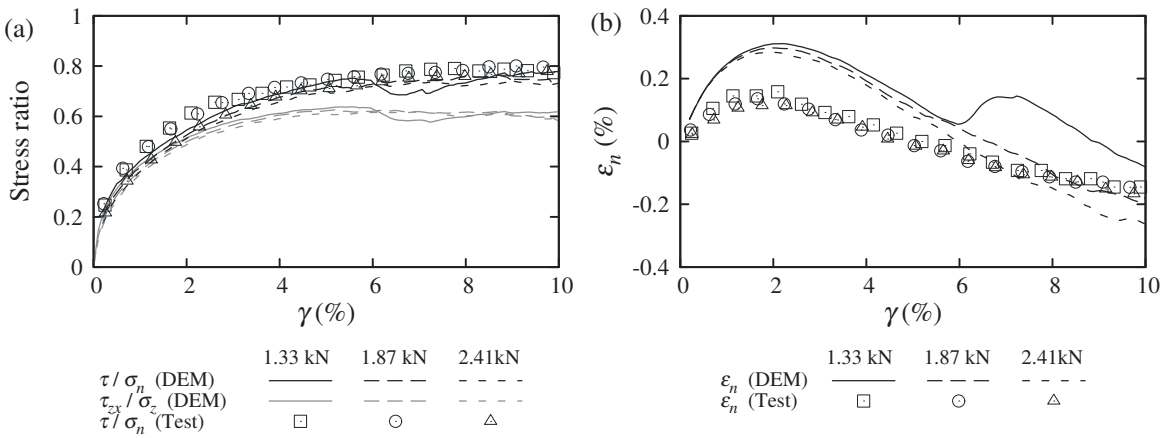

Fig. 3.8 Response of (a) the tangential–normal stress ratio and (b) the normal strain of a PP soilbag in SS tests and simulations.

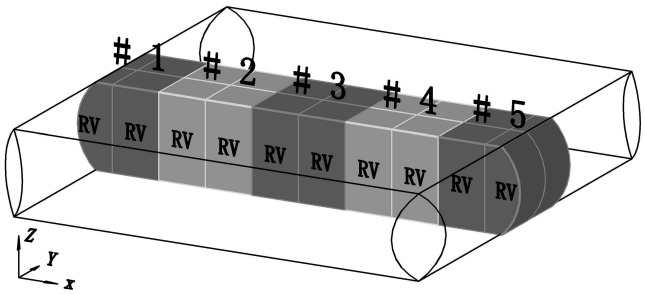

Fig. 3.9 Illustration of the five selected volumes for probing local stress paths.

is because the confinement effect is the least significant and the most anisotropic among all cases (see Fig. 3.18) which raises the possibility of sudden fluctuations in the force chains and particle configuration of the granular system.

3.3.2 Stress path analysis

The particle-based stress tensors were averaged in five consecutive GRS volumes, #1–5, aligned along the x axis. Each consists of four neighboring RVs as shown in Fig. 3.9. #0 represents averaging over the overall Delaunay volume of the entire GRS from which the void ratio is computed.

Fig. 3.10 shows the stress paths of the selected GRS volumes in the PE and PP soilbags under the UC loading course. In both cases, linear global and local stress paths were observed regardless of the difference in the tensile strength of the two geotextiles. The paths turned slightly nonlinear when partial breakages on the geotextile fabric started to form. After the

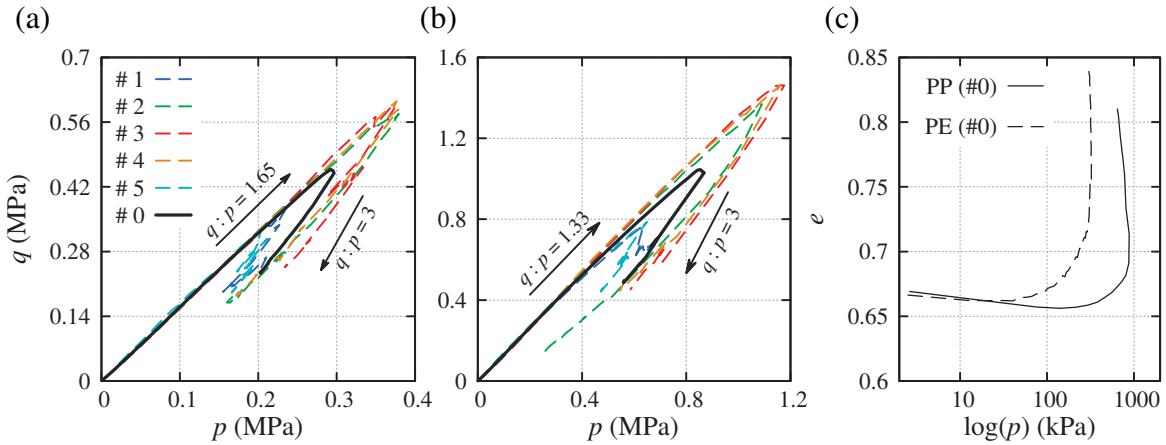

Fig. 3.10 Global and local stress paths of the soil wrapped by (a) PE and (b) PP geotextile, and (c) the e-log(p) relations of both types of GRS in UC simulations.

global failure, the PE and PP soilbags underwent stress paths similar to the unloading of drained triaxial compression. The sustained lateral stress σ_x and σ_y, as shown in Fig. 3.7, ensured a gentle decrease in the compressive strength of the soilbag. A summary view of the internal force chains and the distribution of mean stress p in the PE geotextile-wrapped GRS at the peak stress state and the final state is shown in Fig. 3.12. T represents the tensile force in the geotextile yarns. The colors of the force chains indicate the magnitudes of the tangential forces f_t^c, whereas the radii of the force chains' cylinders are proportional to the norms of the normal forces f_n^c. It was confirmed again, as in Tantono and Bauer [2008], that a soilbag under compression has concentrated stress in the middle (#2, #3 and #4 in Fig. 3.12a). This non-uniformity does not exist initially. It grows with sustained compression until the global failure and then drops gradually as the fabric rupture progresses in the geotextile. At the final state (ε_a = 20%) the geotextile wears out in the middle part, which corresponds to the failure mode of the soilbag in the test (see Figs. 3.6a and 3.12b). The development of large interconnecting openings as shown in Fig. 3.12b leads to a great loss of strong normal force chains in the vicinity. As a result, all local stress paths collapse to the global one, returning to a uniform stress state.

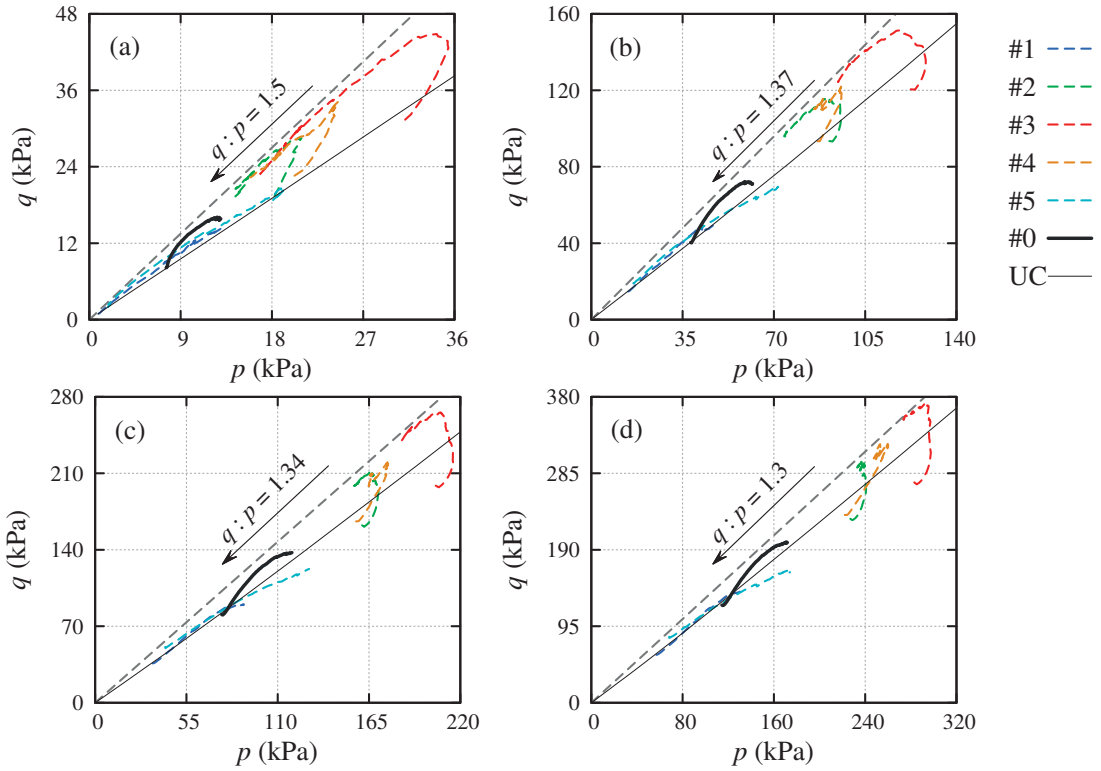

Fig. 3.11 Global and local stress paths of the soil wrapped by PP geotextile in SS with a vertical dead load P corresponding to: (a) 2.41 kN, (b) 12.05 kN, (c) 24.1 kN, and (d) 36.15 kN.

The stress paths of the PP soilbag under SS are plotted in Fig. 3.11. Four cases (P = 2.41, 12.05, 24.1 and 36.15 kN) are presented here. In each case, the global stress path initially deviates from the stress path under UC, approaching the critical state line (CSL) of the wrapped GRS. Because shearing only dominates in the middle part of the GRS, the global path eventually heads away from the CSL. As the vertical dead load rises, the slope of the CSL of the wrapped GRS decreases gradually and is always lower than that of the Toyoura sand. As a result, less distortion is produced at the critical state in the wrapped GRS than in the Toyoura sand. The dilatancy of the sand is better contained by wrapping the soil completely in a soilbag.

At the local scale, interesting loading-unloading local stress paths exist in the middle (#2–4) of the GRS. After passing the phase transformation stage (PTS), which coincides with ε_a changing from compressive to dilative, further shear deformation results in a persistent drop in both p and q levels along the CSL. While the GRS in the middle keeps dilating, the particles neighboring the lateral boundaries (#1, #5) are constantly compressed along the

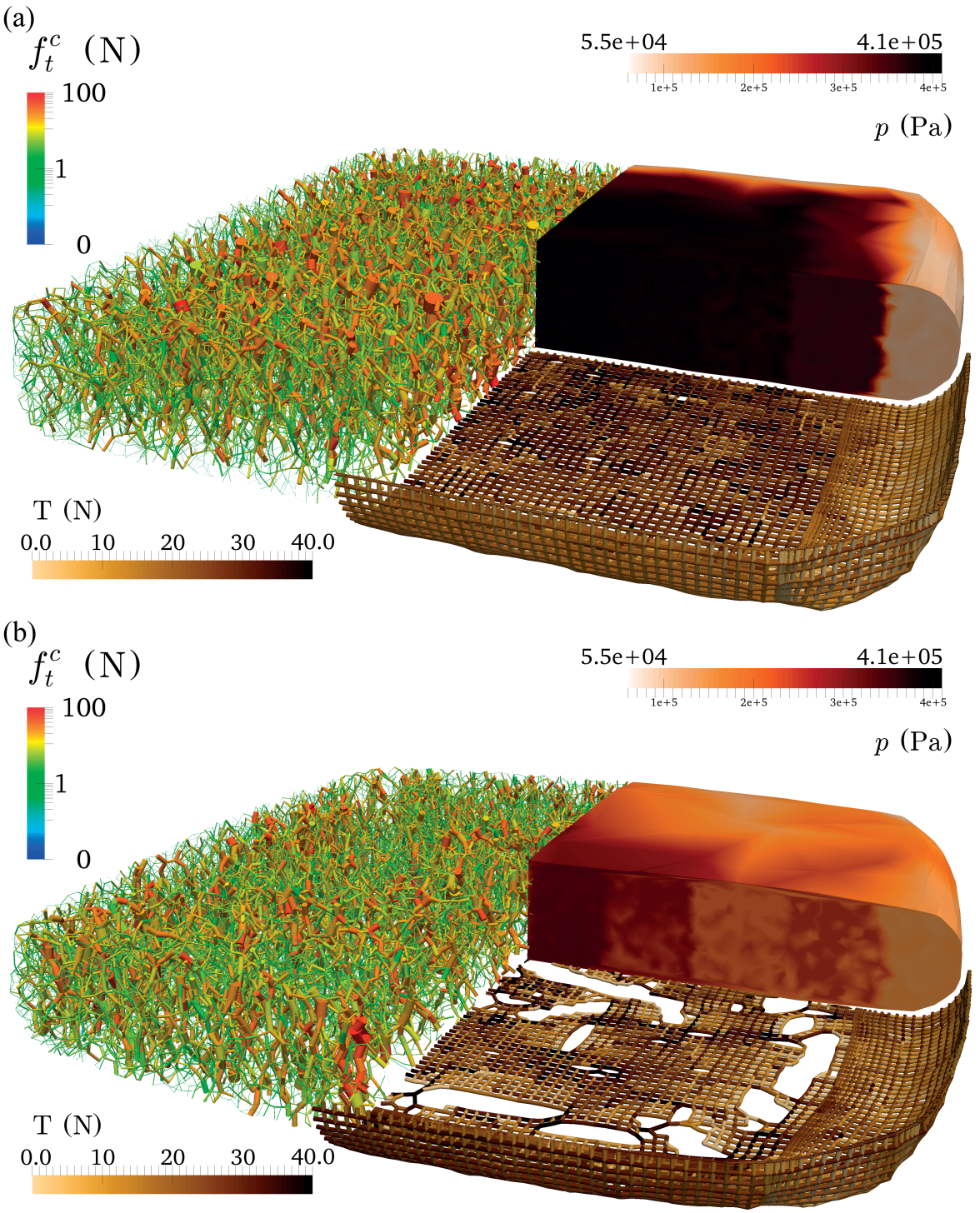

Fig. 3.12 Force chain, p distribution in the wrapped soil and T distribution in the geotextile of a PE soilbag for (a) peak stress state and (b) final state in UC.

compression line. In turn, the global stress state evolves toward a more uniform state and the dilatancy is further restrained. High damping in the soilbag can be attributed to hysteresis energy dissipation induced by the partial loading-unloading stress paths in the middle of the soilbag. These absorbing local stress paths result from the redistribution of internal forces.

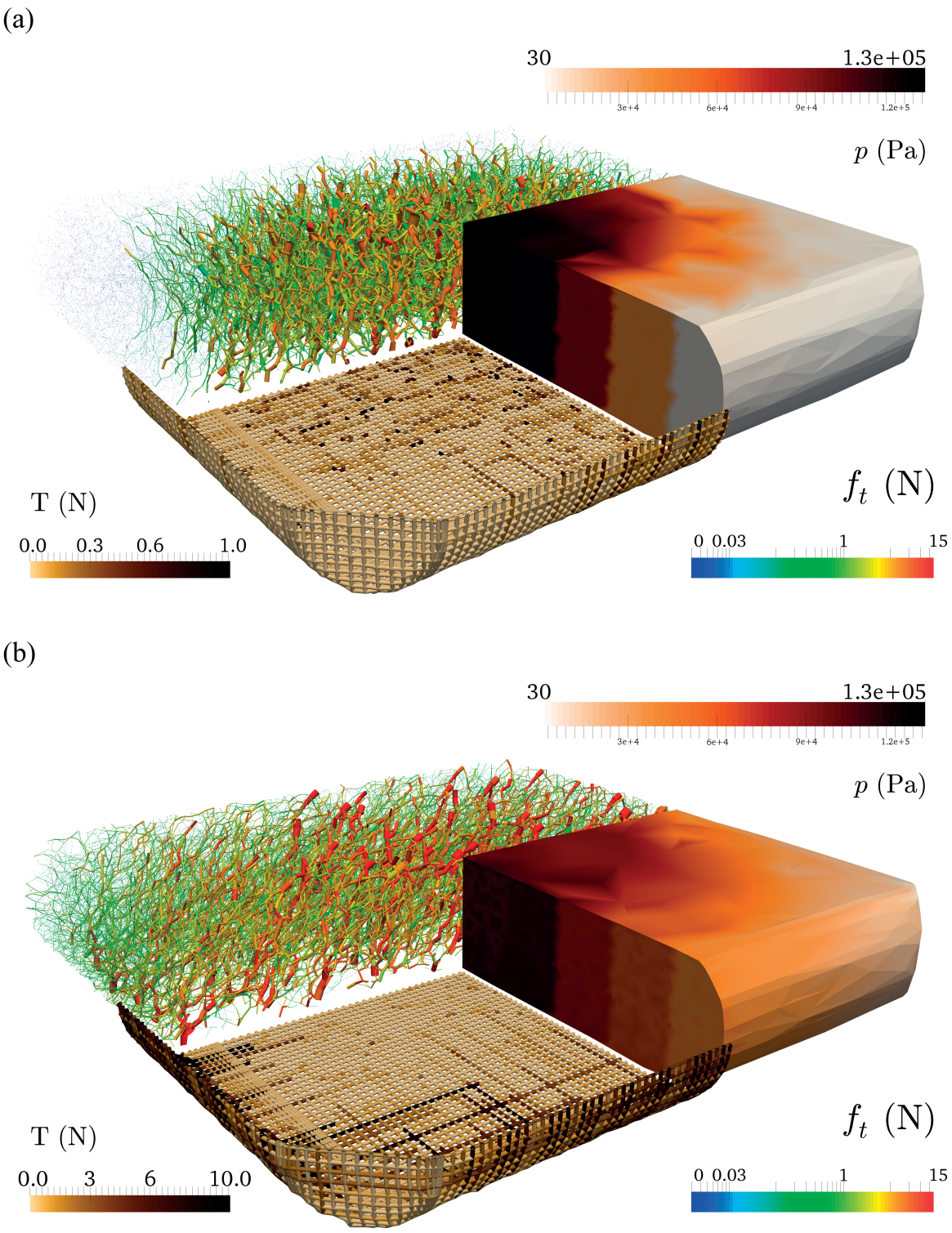

Fig. 3.13 Force chain, p distribution in the wrapped soil and T distribution in the geotextile of a PP soilbag for (a) initial state and (b) final state in SS (P = 12.05 kN).

The transfer of concentrated force chains into the domain near the lateral boundaries during shear is shown in Fig. 3.13 (P = 12.05 kN). Upon the wrapped GRS reaching its shear strength during shear, tension distributes in a pattern opposite to that in the UC condition: the tensile

force on the lateral faces is higher than on the top and bottom surface of the geotextile bag. In both loading courses, tension in the yarns was found to be greater along the hoop direction than in the axial direction.

3.3.3 Volumetric change in compression

The relationships between the void ratio e and mean stress p of the PE and PP geotextile-wrapped GRS under UC are compared in Fig. 3.10c. The dashed line shows persistent volumetric expansion in the PE soilbag after initial contraction, similar to the volumetric change of dense sand in triaxial compression. However, applying stress paths like those in Fig. 3.10a and b to the sand should result in volumetric contraction instead. Such a difference can be attributed to the contribution of the confinement mechanism in the soilbag. Unlike compression at all principal directions on the sand specimen in triaxial tests, the confining stress on the soilbag is gained from growing tension in the geotextile, which is essentially induced by axial compression and lateral extension. In the case of the weaker geotextile (PE), relatively less lateral confinement (larger σ_z/σ_x, or q/p) is produced. When the lateral extension surpasses the axial compression, the wrapped GRS volume expands, as illustrated by the dashed line in Fig. 3.10c. The stress path in the PE case has a slope (q/p = 1.65) close to that of the critical state line (M_c = 1.76) of the Toyoura sand at 90% relative density in the triaxial compression condition. Furthermore, the deviatoric strain distribution in the x–z cross-sectional plane (see Fig. 3.14) indicates strain localization, which is often regarded a precursor to progressive failure, starting at a small strain level. Because the confinement effect provides the wrapped GRS with additional lateral stress, the stress state of the wrapped GRS evolves along the CSL until the global failure of the geotextile. In this case, it is the progressing granular failure that eventually drives the failure of the soilbag.

The solid line in Fig. 3.10c shows a completely different failure mechanism. The volume of the PP soilbag was contracted persistently until the geotextile could no longer bear any greater tensile force. Prior to the first fabric rupture, the void ratio remained nearly constant. With the ruptures growing on the top and bottom surfaces of the container, the wrapped GRS

gradually expanded. After a sufficient number of large openings were formed, the mean stress p started to drop gradually with more significant volumetric expansion in the wrapped GRS. In this case, it is the sustained flattening of the geometrical shape of the soilbag that caused the failure. The wrapped GRS did not fail during the whole loading course and the stress state was heading away from the CSL. This finding explains how effective the reinforcement is in making use of and constraining the dilatancy to improve the bearing capacity of the wrapped soil.

3.3.4 Interlocking in compression and confinement in shear

One of the motivations of this study is to clarify the roles of confinement and interlocking in a soilbag in symmetrical (UC) and asymmetrical (SS) boundary conditions. The following equation can be applied to examine the interfacial interlocking in the DEM soilbag during compression.

$$\Phi_i = 180/\pi \tan^{-1}(\sqrt{\tau_{ij}^2 + \tau_{ik}^2}/\sigma_i) \tag{3.5}$$

where τ_{ij} and τ_{ik} are a pair of shear stresses on the interface at which the normal stress σ_i is applied, and Φ_i represents the friction angle at the interface perpendicular to axis i. Interfacial stresses defined in this manner are shown in Fig. 3.15a. Because local shear stress should be symmetrically distributed during UC, averaging over the entire GRS domain would produce shear stress caused by strain localization. Thus, the averaging was carried out over a quarter of the GRS, as shown in Fig. 3.15a, to calculate the interfacial friction angles.

In the case of the PE soilbag, the interfacial friction angle was considerably smaller than the maximum strength (Fig. 3.15b and Fig. 3.5b), whereas the wrapped soil attained its frictional strength at a small strain level and exploited it thereafter with increasing confinement from the wrapping material (Fig. 3.10a). As shown in Fig. 3.14, the deviatoric strain at the soil–geotextile interface was not as mobilized as the deviatoric strain in the shear bands of the

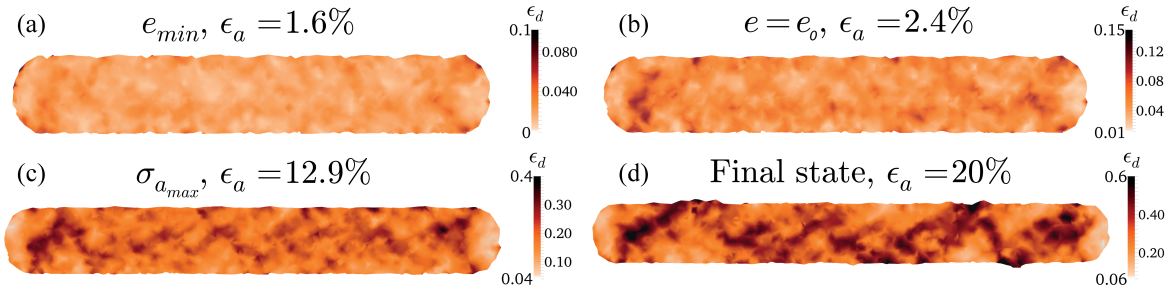

Fig. 3.14 Deviatoric strain distribution on the central x–z cross-section plane of a PE soilbag in UC.

wrapped GRS. On the x–z or y–z planes, both the soil and the geotextile compatibly deformed at the interface where no shear stress is produced.

This finding is reasonable; if the symmetry holds for the GRS and the boundary condition for UC on the wrapped soil is symmetrical, shear stress will never be exerted at the interface. In the simulation, the interlocking force should be negligible when the symmetry remains intact. Fig. 3.15b shows that only the interfacial friction on the x–y plane developed with axial compression of the soilbag. Starting at a mild level, the friction abruptly increased after passing the failure and then became stagnant. It suggests that the symmetry on the x–y plane does not perfectly hold even at a small strain level, which causes some initial interlocking along the hoop direction. When the geotextile begins to rupture, which triggers the symmetry to break, the interlocking will be significantly enhanced and will work as a secondary mechanism for constraining the swelling of the soil and maintaining effective lateral confinement.

The interface interlocking serves a dominant role in the soilbag in shear. The confinement effect in shear should also be investigated to analyze the roles of the two mechanisms. Fig. 3.16 shows that the lateral normal stress σ_x and σ_y nearly doubled when the wrapped GRS approached its shear strength. However, because σ_z was rising with sustained shear, there should be neither a peak nor softening in the τ_{zx} response. Upon reaching the critical condition, the stress state of the wrapped GRS can be approximated as an isotropic stress coupled with a pair of shear stresses in the shear (x–z) plane.

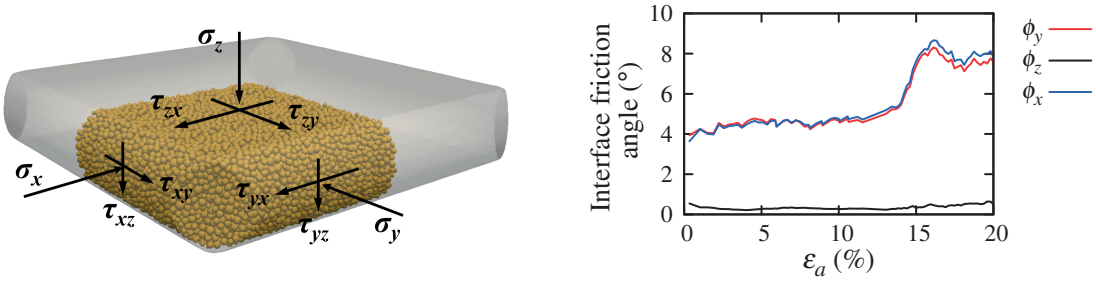

Fig. 3.15 (a) A quarter of the GRS domain and corresponding stress components and (b) evolution of friction angles at the soil–geotextile interfaces of a PE soilbag in UC.

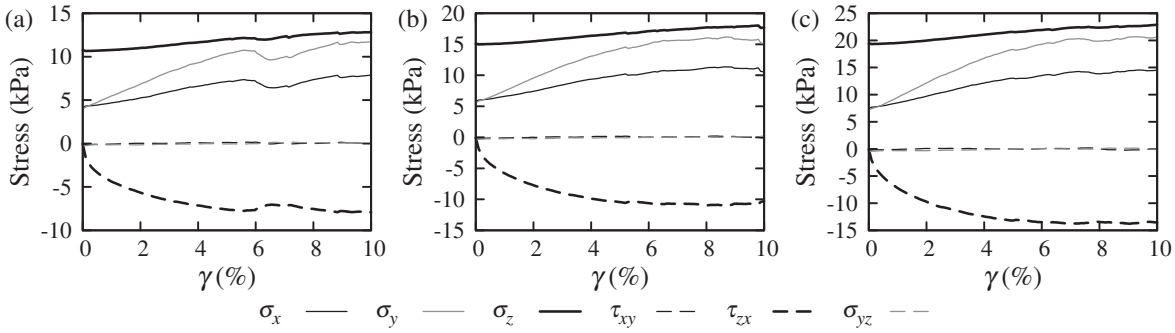

Fig. 3.16 Average stress components over the entire GRS domain of a PP soilbag with a vertical dead load P that corresponds to (a) 1.33 kN (b) 1.87 kN, and (c) 2.41 kN.

3.3.5 Fabric anisotropies of the wrapped GRS

The characteristics of the fabric anisotropies in the geotextile-wrapped GRS are investigated based on the studies of Oda [1972] and Guo and Zhao [2013], which should explain the soilbag reinforcement mechanisms from a microscopic perspective. With the information about the configuration of particles and internal force chains, Eqs. 3.6–3.8 provide the corresponding fabric tensors for the spatial distribution of the contact normals and the normal and tangential force chains, namely, $\boldsymbol{\varphi}^c$, $\boldsymbol{\chi}^n$, and $\boldsymbol{\chi}^t$. As an analogy to q of the stress tensor, the deviatoric parts of these tensors are used to compute the anisotropies.

$$\boldsymbol{\varphi}^c = \frac{1}{N_c} \sum_{N_c} \boldsymbol{n^c} \otimes \boldsymbol{n^c} \tag{3.6}$$

$$\boldsymbol{\chi}^n = \frac{1}{N_c} \sum_{N_c} \frac{f_n^c \boldsymbol{n}^c \otimes \boldsymbol{n}^c}{1 + \boldsymbol{a}^c : (\boldsymbol{n}^c \otimes \boldsymbol{n}^c)} \tag{3.7}$$

$$\boldsymbol{\chi}^t = \frac{1}{N_c}\sum_{N_c}\frac{f_t^c \boldsymbol{t}^c \otimes \boldsymbol{n}^c}{1+\boldsymbol{a}^c : (\boldsymbol{n}^c \otimes \boldsymbol{n}^c)} \tag{3.8}$$

where $\boldsymbol{n}^c$ and $\boldsymbol{t}^c$ correspond to the unit vectors normal and tangential to the contact plane, respectively; N_c is the total number of contacts that fall into the categories of (a) soil-to-soil, (b) soil-to-geotextile, (c) soil-to-plate (only definable after fabric rupture); and f_n^c and f_t^c are the length of the inter-particle contact forces along the normal and tangential directions, respectively. $\boldsymbol{a}^c = 15/2\mathrm{dev}(\boldsymbol{\varphi}^c)$ is the fabric anisotropy tensor due to geometrical change. Analogously, using the averaged contact normal force $\bar{f}^0 = \mathrm{tr}(\boldsymbol{\chi}^n)$, the other two mechanical anisotropy tensors can be defined as $\boldsymbol{a}^n = 15/2\mathrm{dev}(\boldsymbol{\chi}^n)/\bar{f}^0$ and $\boldsymbol{a}^t = 15/3\mathrm{dev}(\boldsymbol{\chi}^t)/\bar{f}^0$ for the normal and tangential part of the force chains, respectively. Their second invariants can be employed to measure the intensity of anisotropy as defined in Eq. 3.9

$$a_* = \mathrm{sign}(S_r)\sqrt{\frac{3}{2}\boldsymbol{a}^* : \boldsymbol{a}^*} \tag{3.9}$$

where * denotes c, n or t and S_r is computed as the inclination between a specific anisotropy tensor and the stress deviator $\mathrm{dev}(\boldsymbol{\sigma})$. For the wrapped GRS, S_r is always positive in either the UC or SS loading condition. The following paragraphs will discuss the relation of these fabric anisotropies to the confinement effect, the compressive and the shear strength of soilbag.

Fig. 3.17 shows the evolution of the fabric anisotropies a_c, a_n and a_t with deviatoric strain ε_d under UC. For both PE and PP soilbags, a_n and a_t drop gradually with increasing ε_d, indicating an increase of normal and tangential forces in the lateral directions. Macro-

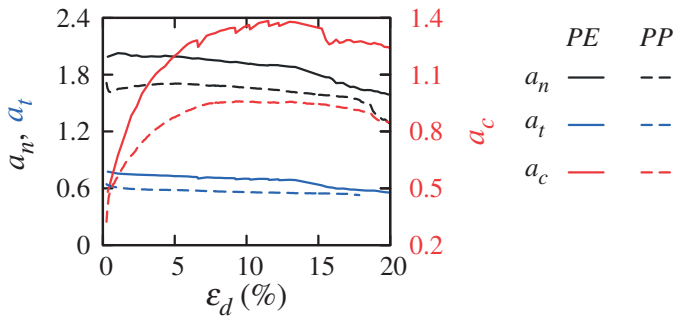

Fig. 3.17 Evolution of fabric anisotropies a_n, a_t and a_c of PE and PP soilbag in UC.

scopically, this results in rising lateral confining stresses σ_x and σ_y. Fabric anisotropy due to the geometrical configuration in the soilbag has a tendency similar to that in conventional triaxial loading conditions. In both cases, a_c becomes stagnant when some yarn starts to break partially, as illustrated in Fig. 3.12a, and drops down mildly after some interconnecting ruptures start to develop, as shown in Fig. 3.12b. Although similar tendencies can be found regardless of the tensile strength in use, the magnitude of each fabric anisotropy is lower in the case of the stronger PP geotextile. With a strong geotextile, relatively more and stronger lateral force chains (lower a_c and a_n) exist in the wrapped GRS. At the macro scale, this results in greater confining stress and eventually reduces the slope of the stress path under the UC condition. Fig. 3.18 shows the evolution of the fabric anisotropies a_n and a_c with shear strain γ under SS. For all considered SS simulations, a_n dropped gradually with sustained γ after passing the PTS even though a constant vertical load was maintained in these cases. The geometrical fabric anisotropy a_c has a similar tendency to that of a soil specimen in triaxial compression DEM simulations [Guo and Zhao, 2013]. In both cases, a_c becomes stagnant when the wrapped soil reaches its shear strength. The critical value of a_c in granular material is closely related to the material's shear strength. For geotextile-wrapped GRS, the critical a_c should be determined from both the geotextile's tensile stiffness and the soil property. Fig. 3.18 also gives a group of fabric anisotropy responses under a variety of vertical dead loads. In addition to the variation of a_c with shear deformation, the critical a_c was found to be reduced with higher levels of compressive load, suggesting that the critical a_c is a state parameter related to the stress history as well. A similar pattern exists among the responses of the mechanical fabric anisotropy a_n under different vertical loads. From a microscopic

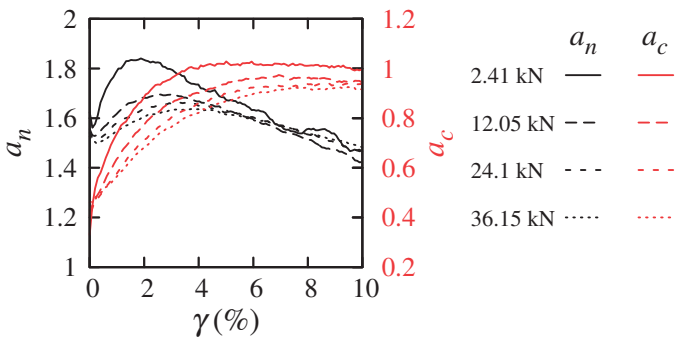

Fig. 3.18 Evolution of fabric anisotropies a_n and a_c of a PP soilbag in SS.

viewpoint, the confinement of the geotextile-wrapped GRS develops in not only compression but also shear. Greater compression prior to shear will enable more isotropic confinement to be attained on the wrapped GRS during shear.

3.4 Conclusions

This chapter presents a novel approach for the discrete modeling of soilbags. New knowledge is provided for clarifying the reinforcement mechanisms of the geosynthetic-wrapped soil from the perspectives of stress state, volumetric change and anisotropies. Two types of woven geotextile (PE and PP) soilbags were modeled using the DEM. The parameters of the contact laws for the soil, the geotextile and their interface were carefully calibrated against triaxial, wide-width tensile and shear box test results. With a properly assumed 3D geometry for the geotextile container, the wrapped soil was generated in a 3D–assembling–filtering–expanding process, using the same RV as for the calibration of the contact law. The responses of the soilbag in the DEM simulations and the tests in UC and SS were consistent. Using this new approach of soilbag modeling, the evolution of fabric rupture in the geotextile can be observed and a close relationship between the fabric anisotropies and the reinforcement effect can be attained. The main findings regarding the stress states and the fabric anisotropies of a soilbag are as follows:

- Under unconfined compression, both global and local stress paths are linear at the pre-failure state with greater p and q values in the middle of the wrapped soil. At the post-failure stage, the lateral confining stress remains nearly constant, which leads to a gentle decline in the bearing capacity. The soil–geotextile interfacial shear stresses are found to be higher on the lateral sides than on the top and bottom sides, but each of them is greatly below the maximum for mobilizing the interface.

- The global stress path in simple shear approaches the critical state line of the wrapped soil first and then heads away with lower q and greater p. Partial loading–reloading paths are experienced in the middle of the wrapped soil, which explains the high

damping of the soilbag. As the vertical dead load rises, the slope of the critical state line decreases, indicating a better control on the dilatancy of the wrapped soil.

- The soilbag constrains dilatancy differently depending on the tensile stiffness of the geotextile. For the soil wrapped by the strong geotextile (PP), the numerical predictions show that the critical state is never reached during compression and the volume does not dilate until the geotextile starts to fail. For the weak geotextile (PE), the soil reaches the critical state with sufficiently developed shear bands and dilatancy. However, the stress path progresses along the critical state line due to the sustained confinement on the wrapped soil.

- The decreasing mechanical fabric anisotropies in either loading course suggest that confinement is the primary mechanism of the soilbag reinforcement method. A stronger geotextile enables more isotropic confinement. The results on interfacial shear indicate that the interlocking effect takes a secondary role in prolonging the effective lateral confinement, particularly during the post-failure stage of compression. During simple shear, the confinement of the wrapped soil grows increasingly isotropic with greater shear deformation and a higher level of vertical dead load.

References

Ahmed, M., Tran, V., and Meguid, M. (2015). On the role of geogrid reinforcement in reducing earth pressure on buried pipes: experimental and numerical investigations. *Soils and Foundations*, 55(3):588–599. pages 51

Ansari, Y., Merifield, R., Yamamoto, H., and Sheng, D. (2011). Numerical analysis of soilbags under compression and cyclic shear. *Computers and Geotechnics*, 38(5):659–668. pages 51, 52

Bhandari, A. and Han, J. (2010). Investigation of geotextile–soil interaction under a cyclic vertical load using the discrete element method. *Geotextiles and Geomembranes*, 28(1):33–43. pages 49, 51

Boubaker, B., Haussy, B., and Ganghoffer, J. (2007). Discrete models of woven structures. Macroscopic approach. *Composites Part B: Engineering*, 38(4):498–505. pages 51, 58

Cai, Z. and Bathurst, R. J. (1995). Seismic response analysis of geosynthetic reinforced soil segmental retaining walls by finite element method. *Computers and Geotechnics*, 17(4):523–546. pages 49

Chareyre, B. and Villard, P. (2005). Dynamic spar elements and discrete element methods in two dimensions for the modeling of soil-inclusion problems. *Journal of Engineering Mechanics*, 131(7):689–698. pages 51

Chen, C., McDowell, G., and Thom, N. (2012). Discrete element modelling of cyclic loads of geogrid-reinforced ballast under confined and unconfined conditions. *Geotextiles and Geomembranes*, 35:76–86. pages 51

Chen, C., McDowell, G. R., and Thom, N. H. (2014). Investigating geogrid-reinforced ballast: Experimental pull-out tests and discrete element modelling. *Soils and Foundations*, 54(1):1–11. pages 49

Cheng, H. and Yamamoto, H. (2015). Discrete modeling of geotextile-wrapped soil under simple shear. In *PARTICLE-BASED METHODS IV Fundamentals and Applications*, pages 485–496, Barcelona, Spain. pages 59

Cheng, H. and Yamamoto, H. (2016). Modeling microscopic behavior of geotextile-wrapped soil by discrete element method. *Japanese Geotechnical Society Special Publication*, 2(65):2215–2220. pages 59

Cheng, H., Yamamoto, H., Jin, S., and Okano, S. (2013). Soil reinforcement using soilbags – A preliminary study on its static and dynamic properties. In *Geotechnics for Sustainable Development*, pages 569–578, Hanoi, Vietnam. pages 52, 53

Guo, N. and Zhao, J. (2013). The signature of shear-induced anisotropy in granular media. *Computers and Geotechnics*, 47:1–15. pages 62, 74, 76

Han, J., Bhandari, A., and Wang, F. (2012). DEM analysis of stresses and deformations of geogrid-reinforced embankments over piles. *International Journal of Geomechanics*, 12(4):340–350. pages 51

Indraratna, B. and Nimbalkar, S. (2013). Stress-strain degradation response of railway ballast stabilized with geosynthetics. *Journal of Geotechnical and Geoenvironmental Engineering*, 139(5):684–700. pages 49

Liu, S., Gao, J., Wang, Y., and Weng, L. (2014). Experimental study on vibration reduction by using soilbags. *Geotextiles and Geomembranes*, 42(1):52–62. pages 50

Lohani, T., Matsushima, K., Aqil, U., Mohri, Y., and Tatsuoka, F. (2006). Evaluating the strength and deformation characteristics of a soil bag pile from full-scale laboratory tests. *Geosynthetics International*, 13(6):246–264. pages 49, 50

Matsuoka, H. and Liu, S. (2003). New earth reinforcement method by soilbags ("Donow"). *Soils and Foundations*, 43(6)(6):173–188. pages 49, 50

Matsuoka, H. and Liu, S. (2006). *A new earth reinforcement method using soilbags*. Taylor & Francis/Balkema, The Netherlands (2006). pages 50

Matsuoka, H., Yamamoto, H., and Nomoto, F. (2010). D·Box method as modern soilbag technology and its local consolidation and vibration reduction effects. *Geosynthetics Engineering Journal*, 25:19–26. pages 50

Modenese, C. (2013). *Numerical study of the mechanical properties of lunar soil by the discrete element method*. PhD thesis, University of Oxford. pages 56

Muramatsu, D., Bin, Y., and Zhang, F. (2009). Numerical simulation of vibration damping effect of soilbag. *Japanese Geotechnical Journal*, 4(1):71–80. pages 50, 52

Oda, M. (1972). Initial fabrics and their relations to mechanical properties of granular material. *Soils and Foundations*, 12(1)(1):17–36. pages 56, 74

O'Sullivan, C. (2011). *Particulate discrete element modelling: a geomechanics perspective*. Taylor & Francis, Hoboken, NJ. pages 60, 61

O'Sullivan, C., Cui, L., and O'neill, S. C. (2008). Discrete element analysis of the response of granular materials during cyclic loading. *Soils and Foundations*, 48(4):511–530. pages 65

Šmilauer, V., Chareyre, B., Duriez, J., Eulitz, A., Gladky, A., Guo, N., Jakob, C., and Kozicki, J. (2015). Using and Programming. In Project, T. Y., editor, *Yade Documentation*. 2 edition. pages 52, 53

Sun, D., Huang, W., Sheng, D., and Yamamoto, H. (2007). An elastoplastic model for granular materials exhibiting particle crushing. *Key Engineering Materials*, 340-341:1273–1278. pages 56

Tantono, S. F. and Bauer, E. (2008). Numerical simulation of a soilbag under vertical compression. In *Proceedings of the 12th International Conference of International Association for Computer Methods and Advances in Geomechanics*, Goa. pages 50, 51, 52, 67

Tatsuoka, F., Tateyama, M., Uchimura, T., and Koseki, J. (1997). Geosynthetic-reinforced soil retaining walls as important permanent structures. *Geosynthetics International*, 4(2):81–136. pages 49

Thoeni, K., Giacomini, A., Lambert, C., Sloan, S. W., and Carter, J. P. (2014). A 3D discrete element modelling approach for rockfall analysis with drapery systems. *International Journal of Rock Mechanics and Mining Sciences*, 68:107–119. pages 51

Thoeni, K., Lambert, C., Giacomini, A., and Sloan, S. W. (2013). Discrete modelling of hexagonal wire meshes with a stochastically distorted contact model. *Computers and Geotechnics*, 49:158–169. pages 51, 56, 58

Thornton, C. (2000). Numerical simulations of deviatoric shear deformation of granular media. *Géotechnique*, 50(1):43–53. pages 63

Thornton, C., Cummins, S. J., and Cleary, P. W. (2011). An investigation of the comparative behaviour of alternative contact force models during elastic collisions. *Powder Technology*, 210(3):189–197. pages 55

Xu, Y., Huang, J., Du, Y., and Sun, D. (2008). Earth reinforcement using soilbags. *Geotextiles and Geomembranes*, 26(3):279–289. pages 50

Yamamoto, H. and Cheng, H. (2012). Development study on device to reduce seismic response by using soil-bags assembles. In *Research, Development and Practice in Structural Engineering and Construction*, pages 597–602, Perth. pages 52, 53

Chapter 4

Evaluating the Performance of Geotextile Wrapped/Layered Granular Soil: A Comparative Study Using the DEM

4.1 Introduction

Constructing transportation infrastructures, e.g. road and railway, with geosynthetic-reinforced subgrade/ballast [Bathurst and Jarrett, 1988] presents an innovative and sustainable solution for geotechnical problems. Instead of nailing soil with reinforcing bars in embankments, geosynthetic sheet can be layered in the ground to stabilize the slopes. Geosynthetic-reinforced soil (GRS) retaining wall is widely used in Japan [Tatsuoka et al., 1997]. It is constructed with geosynthetic-wrapped soil (GWS) behind concrete facings and geosynthetic-layered soil (GLS) next to the GWS as illustrated in Fig. 4.1a. Matsuoka and Liu [2006] applied the GWS (sand-filled geotextile container) as reinforcement layers in road and railway subgrade, which gives considerable rise of the bearing capacity of the ground and great reduction in traffic vibration. Others found effective usage of the GWS in containing the lateral swelling of expansive soil behind retaining walls [Wang et al., 2015], preventing frost heaving in cold

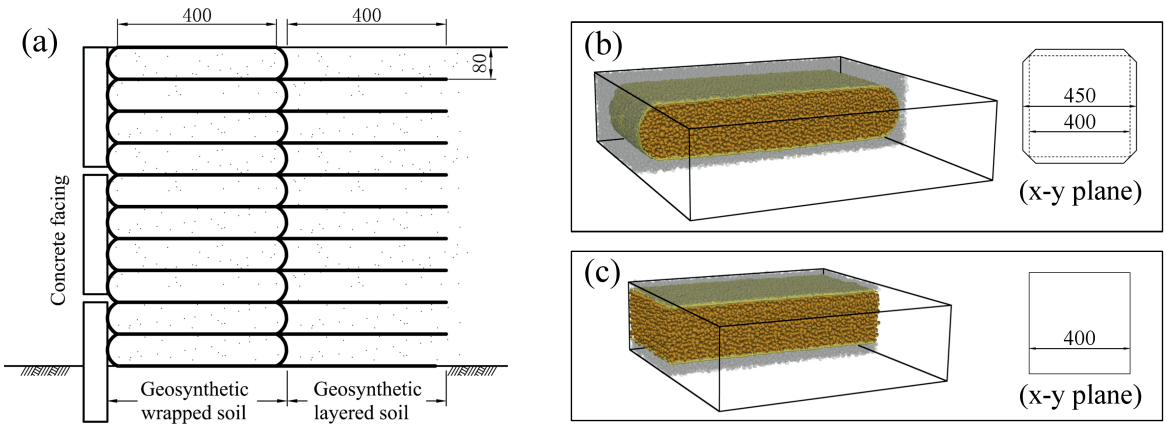

Fig. 4.1 Geosynthetic-Reinforced Soil retaining wall system, and discretization of (b) Geosynthetic-Reinforced Soil and (c) Geosynthetic-Layered Soil.

regions [Li et al., 2012], and facilitating local consolidation in soft clay [Matsuoka et al., 2010].

Though extensive research has been reported on in-situ and laboratory tests of the GWS, few attempted to thoroughly evaluate the performance of the GWS by advanced modeling approach. Meanwhile, it is not clear that under what circumstances flexible geotextile/geomembrane should be included in soils as 2D planar layering (GLS case) or as 3D encapsulation (GWS case). The Finite Element Method may present a way to describe the behavior of the GWS with surface contact algorithms [Ansari et al., 2011], but the discontinuous nature of such complex system hinders the efficiency of the numerical model, especially when failure behaviors and dynamic loads are involved. The discrete element method (DEM) is more suitable for modeling heterogeneous and discontinuous materials like the GRS and the GLS. Loading conditions difficult or expensive to be carried out in practice can be easily simulated by the DEM. Chen et al. [2012] and Han et al. [2012] used bonded DEM particles to examine the interactions between planar geosynthetic sheet and soil. Alternatively, particles can be linked remotely with stretching springs to form a planar wire system as in Thoeni et al. [2013]. Following their approaches, Cheng and Yamamoto [2015, 2016] developed and validated a discrete model of the GWS (sand-filled geotextile container). However, no further comparison to the GLS was given on the performance and the mechanism of different reinforcement methods.

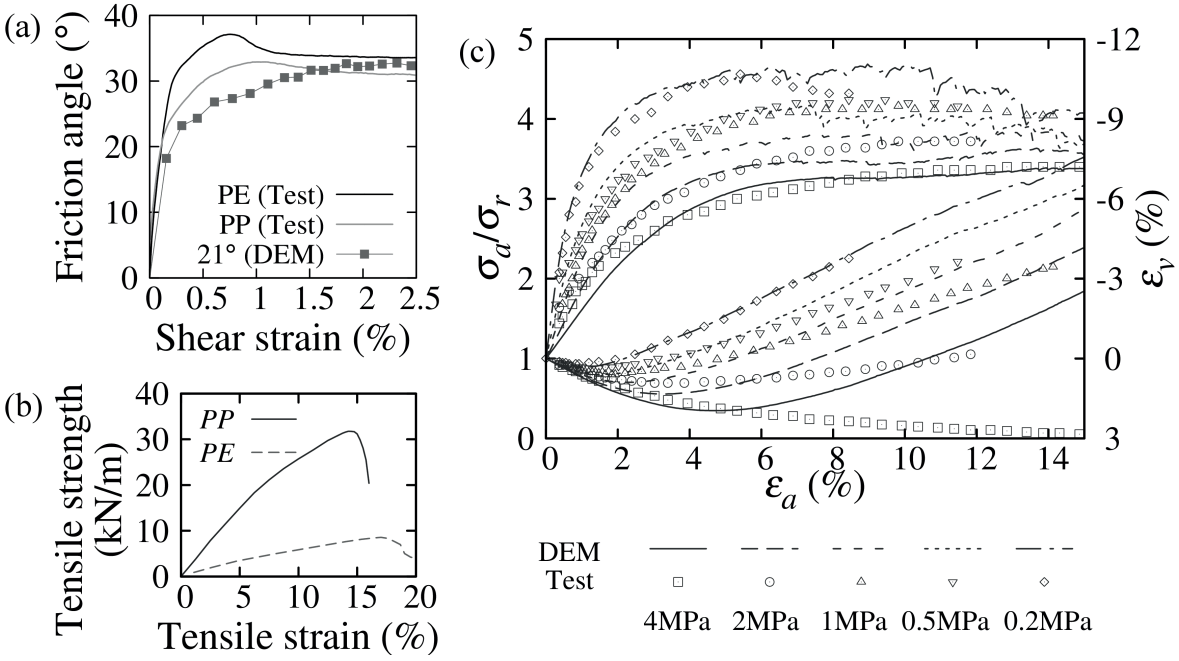

Fig. 4.2 (a) Interface friction at soil–geotextile interfaces, (b) tensile behavior of the geotextiles and (c) triaxial responses of sand specimen and DEM granular assembly.

This chapter introduces a novel approach for discretizing the GWS and the GLS (see Fig. 4.1b and c) in drained triaxial compression condition (DTC). Granular assembly wrapped inside a geotextile container or sandwiched between two geotextile layers are prepared with a scaled particle sized distribution (PSD) of the Toyoura sand. Both the geotextile and the sand are calibrated with laboratory test results. Different tensile stiffness is considered for the geotextile to understand its effect on the performance of the GWS and the GLS under DTC. In addition to comparing the macro responses of the GWS and the GLS in the global and the reinforced domains, a new perspective is provided on stress states and strain characteristics for evaluating the performance of the reinforced soil and the mechanisms of both reinforcement methods. This research is developed based on the open-source framework YADE [Šmilauer et al., 2015].

4.2 Materials of the geosynthetic-reinforced soils

To reasonably compare the responses of the GWS and the GLS, the top and bottom surfaces of the geotextile container and the rectangle geotextile layers are in the same size ($400mm \times 400$

Table 4.1 Micro-parameters for Hertz–Mindlin contact law in both discrete models of GRS.

	Young's modulus (GPa)	Poisson's ratio	Rolling/twisting stiffness (N·m/rad)	Scaled density (10^3kg/m^3)	Inter-particle friction angle (°)
Soil	4	0.33	0.13	2650	29
Geotextile	8	0.33	0.13	444	PP and PE: 21

mm), and the height of the container (80 mm) is exactly the same as the vertical distance between the two GLS layers (see Fig. 4.1b). Additionally, three geotextiles were considered in the simulations: polyethylene (PE) and polypropylene (PP) geotextiles as in the previous studies [Cheng et al., 2016], and a very strong one with fivefold tensile stiffness of the PP geotextile. The calibrated soil-geotextile interfacial friction behavior and tensile strength-strain response are shown respectively in Fig. 4.2a and b. A cubic 1000-particle representative volume (RV) with a shifted PSD was calibrated against the response of the Toyoura sand specimen with initial void ratio $e_0 = 0.68$ in DTC (Sun et al. 2007). The triaxial responses of the RV (Fig. 4.2c) which generally agree with the test data were reproduced using parameters in Table 4.1. Note that the granular assembly in the reinforced zones of both the GWS and the GLS were prepared with the RV's duplicates, such that the assembly can inherit the void ratio and the fabric configuration from the original RV. Calibration of contact laws for the geotextiles and the sand are detailed in Cheng and Yamamoto [2015, 2016].

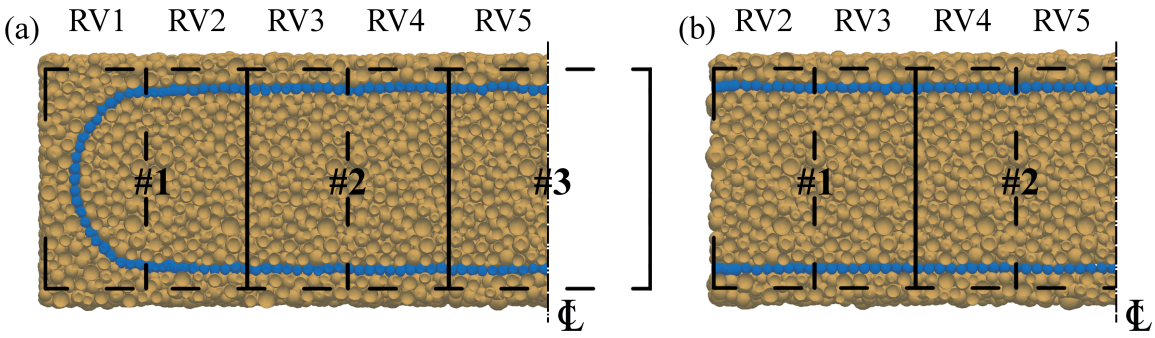

Fig. 4.3 DEM Particle assembly of (a) Geosynthetic-Wrapped Soil and (b) Geosynthetic-Layered Soil on central x–z cross section.

4.3 Discrete modeling of two geosynthetic-reinforced soils

To discretize the GWS, a cubic assembly consists of 10×10 RV copies was filtered using the boundary particles (linked blue spheres fixed in space) of the reinforced domain as illustrated in Fig. 4.3. Then, to eliminate the gaps between the assembly and the boundary, the soil particles were allowed to grow with the same enlarging ratio of 1.0001 whenever the particle system reached quasi-static state (unbalanced force ratio $< 10^{-3}$). The periodic radius expansion stopped when the volume of the system based on the Delaunay cells ceased to grow and the mean overlap ratio became negligible.

The discretization of the GLS was done by simply removing the particles located in the RV domains at the outermost layer of the GWS (e.g. RV1 in Fig. 4.3a). Fig. 4.3a and b shows two particle assemblies representing the GWS and the GLS on the central x–z cross section. At this stage both granular assemblies had the same void ratio ($e_{reinf,0} = 0.675$) and contact orientation diagram in the reinforced domain. Therefore, the only thing differentiates these two reinforced soils was how the geotextile was included, i.e. either as a pair of planar sheets for layering soil or as a container for encapsulating soil.

The particles previously cropped in the filtering stage were added back to form the cubic shape of the GWS and the GLS. These particles were first positioned slightly away from the reinforced domains to avoid overlapping with existing ones. Then, an isotropic confining pressure σ_c = 10 kPa was applied on the cubic periodic cells. While maintaining the isotropic confining pressure, the inter-particle friction of the particles outside the reinforced zone was adjusted gradually to attain the same global void ratios (e_0 = 0.68) in the GWS and the GLS. The DTC was performed with 10% maximum strain rate, 103 density scaling (see Table 4.1), 0.2 non-viscous damping ratio and zero gravitational field. At every 1% axial strain increment, the present strain level was maintained and a higher damping ratio (0.9) was adopted temporarily for acquiring the quasi-static state results (unbalanced force ratio < 10^{-3} and kinetic energy < 10^{-4} J).

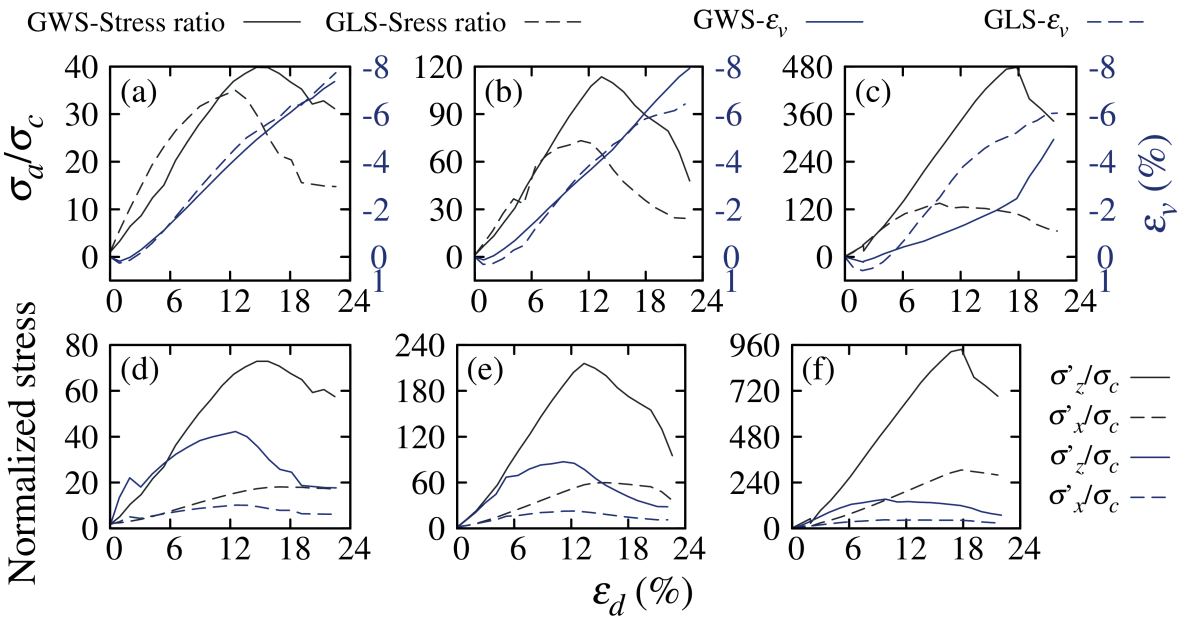

Fig. 4.4 Global triaxial responses of GRS considering (a) PE, (b) PP and (c) 5PP geotextile, and ratios of stresses in reinforced zone to cell confining pressure considering (d) PE, (e) PP and (f) 5PP geotextile.

4.4 Results and discussion

4.4.1 Triaxial response of Geosynthetic-reinforced soils

Stress can be easily acquired with properly defined volumes and the Love formula [Guo and Zhao, 2013]. Fig. 4.4a–c shows the global quasi-state response of the GWS (solid lines) and the GLS (dashed lines) in triaxial compression (σ_c = 10 kPa). In all cases, the ratio of axial stress σ_a to confining stress σ_c grows greater in the GWS than in the GLS. In addition, as the geotextile gets stronger, the GWS outperforms the GLS even further in terms of the global stress response. The global volumetric change ε_v of the periodic cell is found similar in both cases, but the largest ε_v on the contractive side increases as the tensile stiffness of the geotextile rises. When the strong geotextile (5PP) is used (Fig. 4.4c), the volume of the GWS at failure is approximately half that of the GLS. A closer look into the stress inside the reinforced domain helps evaluate the reinforcement effect due to geosynthetic inclusion. Fig. 4.4d-–f compare the normalized horizontal and vertical stress (σ'_x/σ_c and σ'_z/σ_c) in the reinforced domain (enclosed part in Fig. 4.1b and c). As would be expected. Both σ'_x/σ_c and σ'_z/σ_c of the GWS exceed those of the GLS in the whole loading courses and the differences

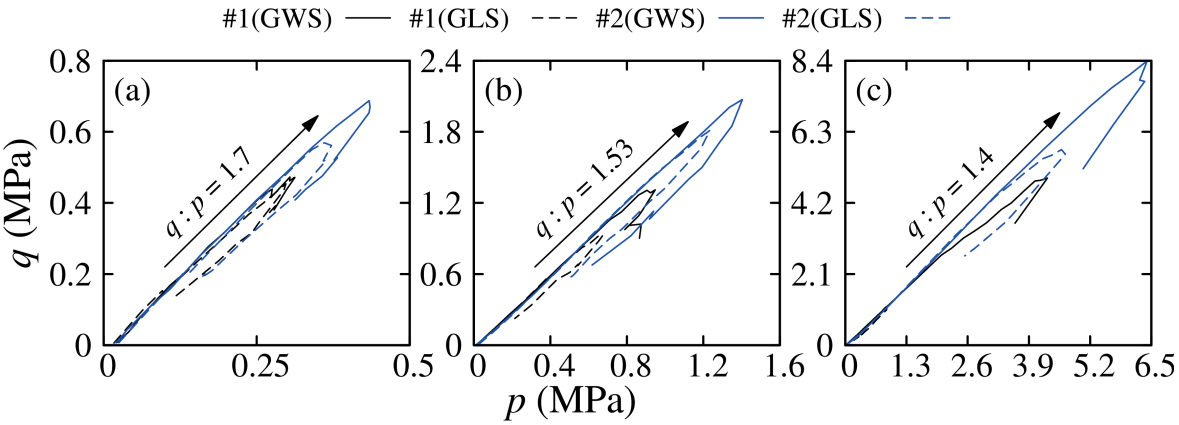

Fig. 4.5 Local stress paths in reinforced zone of (a) PE, (b) PP and (c) 5PP GRS.

herein are greater than in the global domain. In addition, the lateral stress ratio σ_x'/σ_c has higher residue in the GWS, while the ratio drops to the initial level at last in the GLS. In the 5PP case, the GLS's vertical stress ratio is far less than the GWS's horizontal one.

4.4.2 Stress paths analysis

Similar to the stress paths of soil wrapped in a soilbag under unconfined compression [Cheng et al., 2016], linear stress paths are obtained in both the GWS and the GLS under triaxial compression (Fig. 4.5). Based on the locations of the RVs in Fig. 4.3, particle-based stress tensors were averaged in the reinforced domains #1 – #3. Each contains two RVs whose triaxial responses were calibrated as in Fig. 4.2. For simplicity only stress paths in two domains (#1 and # 2) are presented. In all cases, the volume-averaged mean stress p and deviatoric stress q becomes higher, as the probing location moves from the edge to the center. This spatial difference is more significant when the soil is layered and the strong geotextile 5PP is used. This can be attributed to particles near the edges of geotextile sheet continuously flowing out of the effective reinforced domain during compression. In the GWS case, particles were trapped inside the container, thus higher and more uniform stress is produced in the reinforced zone.

Though the geotextile is included differently, the global and local stress paths of the GWS and the GLS have the same slope before the global failure. It seems that the slope of the stress paths of GRS in the reinforced domain is solely determined by the materials, i.e. geotextile'

tensile stiffness and soil's friction coefficient, and loading conditions. It does not change with reinforcement forms: wrapping or layering in the present study. Fig. 4.5a gives a larger stress-path slope ($q/p = 1.7$) which is very close to that of the critical state line (CSL) of the unreinforced Toyoura sand in DTC. As the geotextile becomes stronger (Fig. 4.5a–c), both the global and local stress paths turn increasingly away from the CSL of the soil. This interesting finding helps clarify the reinforcing mechanism of geosynthetic inclusion. By including geosynthetic in soil, additional confining stress is provided with the ratio between p and q depends on the materials and the loading condition. As a result, a new linear state line is posed on the p–q space. In DTC, stress in the reinforced soil grows and then follows this line until the geotextile fails. For weak geotextile, the line overlaps the CSL of the soil (soil fails prior to geotextile). For strong geotextile, it always deviates below the CSL of the soil.

4.4.3 Strain characterization

The void ratios of the particles in the reinforced domain were computed using the Delaunay Triangulation. During the initial isotropic compression, particles wrapped in the container are subjected to additional confining pressure. As a result, the GWS has a slightly lower void ratio in the reinforced domain (e_{reinf}) than the GLS, at the initial state as Fig. 4.6b shows. Owing to the same reason, deviatoric strain ε_d is slightly greater in the GWS than in the GLS at the minimum e_{reinf} state (Fig. 4.6c and d). As axial strain increases, the GLS contracts more than the GWS globally (Fig. 4.6a), but their final global void ratios are almost the same. In the reinforced zone, however, the GWS contracts more than the GLS whose volume is almost constant before the geotextile starts to fail. At last, particles outside the reinforced zone of the GLS are compressed more than the inside ($e_{reinf} \approx 1.5e$), whereas the void ratio is almost uniform in the GWS ($e_{reinf} \approx e$). This is caused by the particles flowing outside the reinforced zone in the GLS as illustrated by the ε_d distribution at the maximum e_{reinf} state in Fig. 4.6e and f. Obvious shear bands develop in the reinforced zone in Fig. 4.6f, but only one significant shear band appears close to the edge of the container in Fig. 4.6e, possibly due to some corner effect. Note that the stress in the two GRS varies greatly at these states. They are chosen for comparing the shear bands in the soils which are reinforced differently.

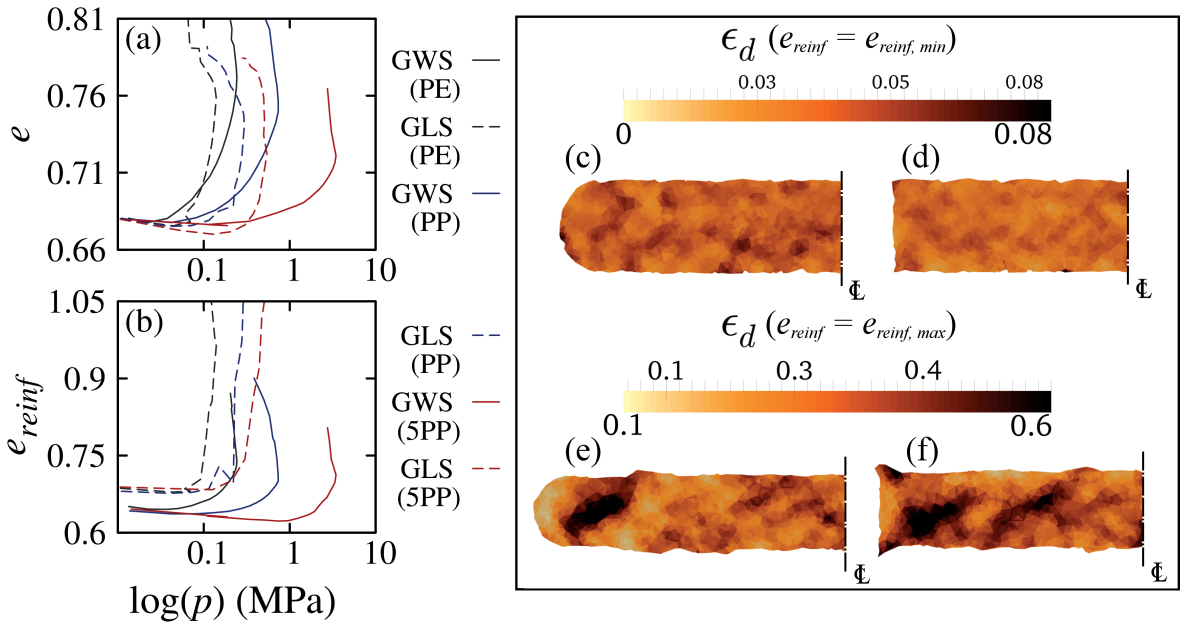

Fig. 4.6 Evolution of void ratio in (a) global and (b) reinforced domain, and (c)–(f) strain localization in the reinforced domain of GWS and GLS considering PP geotextile.

4.5 Conclusions

A comparative study on geosynthetic-wrapped/layered soils was conducted using the discrete element method. The geosynthetic-layered soil was derived from an existing discrete model of the geosynthetic-wrapped soil. Both models were loaded in triaxial compression condition. Global triaxial response, stress path and strain characteristics were investigated in particular. Interesting findings are summarized as follows.

- The geosynthetic-wrapped soil gives greater stress response than the layered soil in the reinforced and global domains. The horizontal stress residue in the former is larger than the vertical one in the latter, if strong geotextile is used. Global volumetric strain changes similarly in two cases, with the layered soil contracting more than the other.

- The simulations produce linear stress paths in the global and local domains having the same slope, regardless of different reinforcement form in use, i.e. container and sheet. Nevertheless, stress is concentrated more in the center in the sheet-layered soil. With the tensile stiffness of the geotextile increasing, both global and local stress paths deviate increasingly below the critical state line of the soil in unreinforced state.

- The simulation shows the soil in the reinforced domain contracts more in the case of the wrapped soil than the layered soil. After 20% axial compression, the void ratio in the reinforced zone of the layered case is 1.5 times of the global one, causing severe strain localization. The wrapped soil, however, has similar void ratio across the whole domain, with less localized strain in the reinforced region.

References

Ansari, Y., Merifield, R., Yamamoto, H., and Sheng, D. (2011). Numerical analysis of soilbags under compression and cyclic shear. *Computers and Geotechnics*, 38(5):659–668. pages 84

Bathurst, R. J. and Jarrett, P. M. (1988). Large-scale model tests of geocomposite mattress-esover peat subgrades. *Transportation Research Record*, 1188:28–36. pages 83

Chen, C., McDowell, G., and Thom, N. (2012). Discrete element modelling of cyclic loads of geogrid-reinforced ballast under confined and unconfined conditions. *Geotextiles and Geomembranes*, 35:76–86. pages 84

Cheng, H. and Yamamoto, H. (2015). Discrete modeling of geotextile-wrapped soil under simple shear. In *PARTICLE-BASED METHODS IV Fundamentals and Applications*, pages 485–496, Barcelona, Spain. pages 84, 86

Cheng, H. and Yamamoto, H. (2016). Modeling microscopic behavior of geotextile-wrapped soil by discrete element method. *Japanese Geotechnical Society Special Publication*, 2(65):2215–2220. pages 84, 86

Cheng, H., Yamamoto, H., and Thoeni, K. (2016). Numerical study on stress states and fabric anisotropies in soilbags using the DEM. *Computers and Geotechnics*, 76:170–183. pages 86, 89

Guo, N. and Zhao, J. (2013). The signature of shear-induced anisotropy in granular media. *Computers and Geotechnics*, 47:1–15. pages 88

Han, J., Bhandari, A., and Wang, F. (2012). DEM analysis of stresses and deformations of geogrid-reinforced embankments over piles. *International Journal of Geomechanics*, 12(4):340–350. pages 84

Li, Z., Liu, S., Wang, L., and Zhang, C. (2012). Experimental study on the effect of frost heave prevention using soilbags. *Cold Regions Science and Technology*, 85(June):109–116. pages 84

Matsuoka, H. and Liu, S. (2006). *A new earth reinforcement method using soilbags*. Taylor & Francis/Balkema, The Netherlands (2006). pages 83

Matsuoka, H., Yamamoto, H., and Nomoto, F. (2010). D·Box method as modern soilbag technology and its local consolidation and vibration reduction effects. *Geosynthetics Engineering Journal*, 25:19–26. pages 84

Šmilauer, V., Chareyre, B., Duriez, J., Eulitz, A., Gladky, A., Guo, N., Jakob, C., and Kozicki, J. (2015). Using and Programming. In Project, T. Y., editor, *Yade Documentation*. 2 edition. pages 85

Tatsuoka, F., Tateyama, M., Uchimura, T., and Koseki, J. (1997). Geosynthetic-reinforced soil retaining walls as important permanent structures. *Geosynthetics International*, 4(2):81–136. pages 83

Thoeni, K., Lambert, C., Giacomini, A., and Sloan, S. W. (2013). Discrete modelling of hexagonal wire meshes with a stochastically distorted contact model. *Computers and Geotechnics*, 49:158–169. pages 84

Wang, L.-J., Liu, S.-H., and Zhou, B. (2015). Experimental study on the inclusion of soilbags in retaining walls constructed in expansive soils. *Geotextiles and Geomembranes*, 43(1):89–96. pages 83

Chapter 5

An Analytical Solution for Geotextile-Wrapped Soil Based on Insights from DEM Analysis

5.1 Introduction

Geosynthetics are cost-effective and environmental-friendly geomaterials that can be designed with great flexibility to reinforce geostructures. Planar geosynthetic sheets, such as geotextiles and geogrids, are commonly embedded horizontally within retaining walls [Kerry Rowe and Skinner, 2001; Tatsuoka et al., 2007] and subgrades [Giroud and Han, 2004a,b]. The cellular forms of geosynthetic reinforcements, e.g. geosynthetic encasements, are installed around granular stone columns in a soft foundation to improve lateral support and restrain dilation [Balaam and Booker, 1985; Pulko et al., 2011; Wu and Hong, 2014]. To facilitate confinement from both vertical and lateral directions on the reinforced soil, Matsuoka and Liu [2003] proposed an earth reinforcement method with complete encapsulations of soil, i.e. wrapping soils in closed geotextile containers. Geotextile-Wrapped Soil (GWS) which incorporates the reinforcing effects produced by both planer- and cellular-form geosynthetics has been proven to be effective for the constructions of retaining structures [Wang et al.,

2015], slope protections [Xu et al., 2008] and roads [Matsuoka et al., 2010], among others. Some have reported the application of GWS assemblies as damping layers to reduce traffic-induced vibrations [Liu et al., 2014; Muramatsu et al., 2009]. Analogues to sand-filled geotextile containers are water/slurry-inflated geomembrane tubes which are usually stacked into offshore barriers. The analytical solutions proposed by Guo et al. [2011, 2015] can predict settlements of the tubes and tensile force distributions on the tube materials under pumping pressure. Nevertheless, the mechanical behavior of the semi-fluid materials inflating the tubes differs fundamentally from the granular soil wrapped within the containers. Moreover, the surcharge loads on sand-filled geotextile containers are usually considerably higher than those on water/slurry-inflated tubes. Compared with the conventional planar sheets, geosynthetics manufactured in partially or entirely closed cellular forms produce greater improvement in the stiffness and strength of the soil [Lajevardi et al., 2015; Latha and Murthy, 2007; Tafreshi and Dawson, 2010]. However, the cellular form inevitably complicates the constitutive behavior of the reinforced soil, making the analytical solution for this composite geomaterial a difficult task.

Some analytical solutions have been proposed for stone columns reinforced with radially closed geosynthetic encasements in soft ground [Balaam and Booker, 1985; Pulko et al., 2011]. The geosynthetic-encased stone columns were considered as perfectly elastoplastic cylindrical solids in triaxial state, whereas the surrounding soil was assumed elastic. The continuity of stress and strain was solved at the soil-stone interface where the additional lateral pressure exerted by the encasement was taken into account. Instead of an elastoplastic approach, empirical relations such as one between dilation rate and deviatoric strain can be extracted from experimental results for developing a simplified solution [Wu and Hong, 2014]. Matsuoka et al. [2004] and Matsuoka and Liu [2006] adopted a similar method in deriving their analytical solution for GWS. They approximated the evolution of stress ratio in GWS under uniaxial/triaxial compression by an exponential function of vertical strain. Although the empirical relation was calibrated by the test results of triaxial compression on the inside soil, the characterization of the stress states was incomplete: the lateral confining stresses in wrapped soil increase as the compression proceeds, rather than staying constant like in

conventional triaxial tests. Moreover, the volume of GWS was assumed constant in Matsuoka and Liu's analytical solution based on engineering experiences, whereas the dilation of the wrapped soil has been characterized as one of the key factors that contribute to the failure pattern of GWS in a recent Discrete Element Method (DEM) analysis of sand-filled geotextile containers [Cheng et al., 2016b].

The objective of this work is to examine the assumptions for the existing analytical model of GWS (AN-GWS) with evidences provided by the DEM simulations of the validated discrete model of GWS (DE-GWS), and thereby propose an elastoplastic analytical framework for this particular cellular-form Geosynthetic-Reinforced Soil (GRS). New assumptions on stress path and dilation rate are made based on the insights obtained from the DEM analyses of GWS. With the help of these assumptions, an elastoplastic formulation for the stress-strain behavior of GWS satisfying the Mohr-Coulomb criterion is proposed. This chapter is organized as follows. Section 5.2 investigates the characteristics of the boundary and interface conditions using the previously validated DE-GWS model [Cheng et al., 2016b]. The stress-strain responses of the constituent soil and geotextile are analyzed respectively to facilitate the understanding of their respective behaviors and the correlation between them. Section 5.3 formulates the elastoplastic analytical solution. Section 5.4 discusses the validity of the model . Section 5.5 examines the predictive capacity of the proposed analytical model in triaxial compression conditions.

5.2 DEM analysis of geotextile-wrapped soil

Numerical methods are usually adopted either to investigate the fundamental behaviors of geomaterials [Guo and Zhao, 2013; Li and Yu, 2013; Zhao and Guo, 2013] or to predict the performance of complex geostructures [Hussein and Meguid, 2016; Indraratna and Nimbalkar, 2013; Yoo and Kim, 2008]. Though the Finite Element Method gives reasonable predictions for the geostructures with geosynthetic reinforcements in planar forms, numerous GRS-related works are conducted using the DEM. The majority of them attempts to explore the reinforcement mechanisms of the GRS designed in various forms and shapes from the

micromechanics perspective [Chen et al., 2012; Cheng et al., 2016b; Han et al., 2012; Ngo et al., 2015; Wang et al., 2016]. The knowledge accumulated from these works needs to be further exploited to facilitate the development of the analytical and constitutive modeling of GRS. To this end, the current work pays a revisit to the new understanding obtained from the DE-GWS model to examine the basic assumptions for the AN-GWS model. In what follows, the DEM fundamentals, i.e. contact laws and model generation, which governs the behavior of the DE-GWS model are introduced first. The evolution of interfacial friction and the distribution of principal stress during uniaxial and triaxial compression numerical tests are then investigated to ascertain the boundary condition assumption for the AN-GWS model. In order to acquire a full picture of the GWS behaviors, the responses of the constituent soil and geotextile are presented respectively considering a wide range of geotextile tensile stiffnesses: the constitutive behavior of the wrapped soil is presented in the e–p'–q space, where e, p' and q correspond to void ratio, mean effective stress and deviatoric stress, respectively, and the average tensile stresses are correlated to the surcharge load.

5.2.1 A DEM model of geotextile-wrapped soil

The DE-GWS model was validated by comparing the numerical predictions with the experimental measurements of the stress-strain responses of a sand-filled geotextile container (length and width of 400 mm, height of 80 mm after initial compaction) subjected to uniaxial compression [Cheng and Yamamoto, 2015b] and simple shear [Cheng and Yamamoto, 2015a]. As illustrated in Fig. 5.1a–b, the Toyoura sand is represented by a particle packing assembled with 100 duplicates of a DEM representative volume of Toyoura sand. The representative volume consists of 1000 particles and was generated with periodic boundary condition (see Fig. 5.1d) and then calibrated with the triaxial response of Toyoura sand specimen with a initial void ratio $e_0 = 0.68$ [Cheng and Yamamoto, 2016]. Because periodic boundary conditions were employed, the compatibility of the contact geometry and mechanics at the interfaces between neighboring representative volumes were guaranteed. The structural mechanics of the geotextile fabrics are approximated by a system of remote springs linked with discrete spherical nodes positioned on an orthogonal mesh (see Fig. 5.1c) [Thoeni et al., 2013]. The

DE-GWS model was adapted in Cheng and Yamamto [2016] for evaluating the performance of GWS and geosynthetic-layered soil in triaxial loading conditions, as shown in Fig. 5.1b. The boundary and interface behaviors during uniaxial and triaxial compression along the short axis are examined in Section 5.2.2 considering the polyethylene (PE) or polypropylene (PP) geotextiles. In Section 5.2.3 four additional GWS cases are included, with the geotextile tensile stiffness set to half, two, three and four times that of the PP geotextile (denoted as 0.5PP, 2PP, 3PP and 4PP).

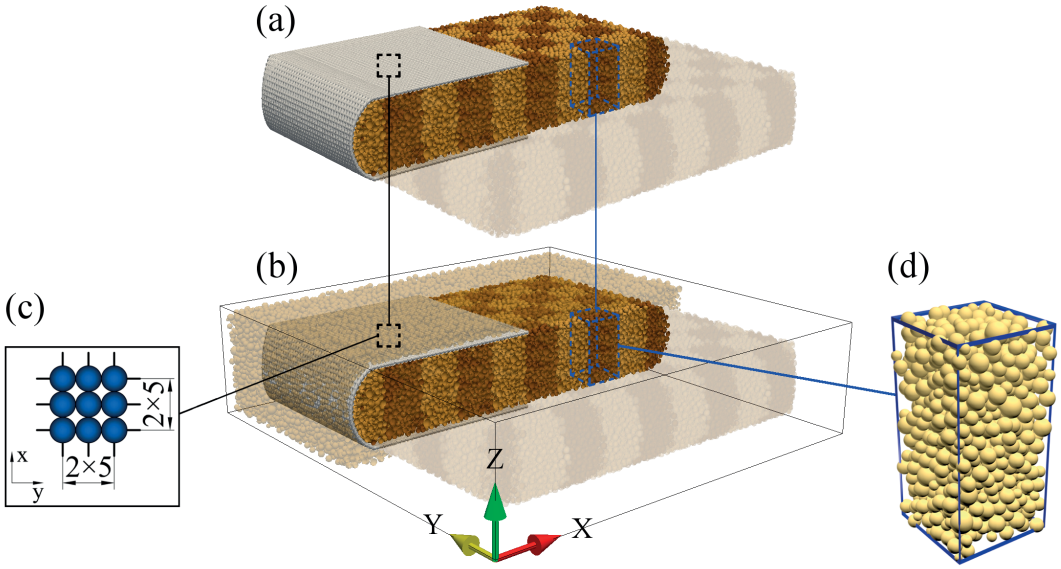

Fig. 5.1 DE-GWS model in (a) uniaxial and (b) triaxial compression states, (b) discretization of geotextile fabrics and (d) representative volume of Toyoura sand.

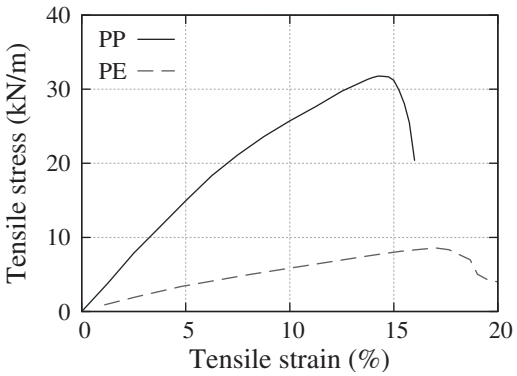

Fig. 5.2 Tensile stress-strain behavior of geotextile fabrics subjected to uniaxial tension

The simplified Hertz-Mindlin model [Thornton et al., 2011] is adopted for the relationship between contact forces and relative displacements of two adjoining particles. A Mohr-Coulomb type plastic condition is enforced on the tangential force to take into account the

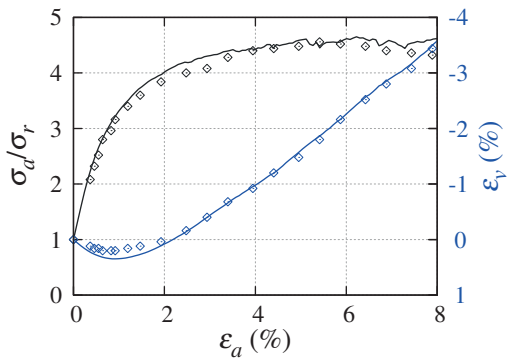

Fig. 5.3 Triaxial response of representative soil volume under 0.2 MPa confining pressure

Table 5.1 Micromechanical parameters for Hertz-Mindlin contact model in DEM analysis.

	Young's modulus (GPa)	Poisson's ratio	Rolling and twisting stiffness (N·m/rad)	Scaled density (10^3kg/m^3)	Inter-particle friction angle (°)
Soil	4	0.33	0.13	2650	29
Geotextile	8	0.33	0.13	444	21
Plate	200	0.33	0.13	7850	0

mobilization of particles. In order to match the macroscopic experimental response, moment transfer is enabled on the contact surfaces where the moments and rotations are related via rolling and bending springs. The remote springs that account for the tensile behavior of the geotextile fabrics are defined by piece-wise linear stress-strain relations (see Fig. 5.2) for PE and PP cases). Friction between wrap and weft was excluded for simplicity. Table 5.1 lists the micromechanical parameters that reproduce the triaxial response of Toyoura sand as shown in Fig. 5.3.

After having filtered the assembled particle packing with the assumed geometry of the geotextile container (see Fig. 5.1a), the radii of the constituent particles were enlarged until the volume conformed to the boundary and the same void ratio as in the representative volume was attained [Cheng et al., 2016b]. During the model generation the virtual spherical nodes of the geotextile were fixed on the mesh, whereas in the uniaxial and triaxial loading stage only the rotational degrees of freedoms are be blocked. To apply triaxial compression on GWS, the assembled particle packing is enclosed in a periodic cell (see Fig. 5.1b) with particles of the same properties filling the remaining empty spaces. The void ratio of the GWS is measured

from the total volume occupied by the assembled particle packing that represents the wrapped soil using a 3D Delaunay triangulation.

The following DEM analysis of the DE-GWS model under uniaxial and triaxial compression are conducted in a quasi-static manner using the open-source framework YADE [Šmilauer et al., 2015]. Readers are referred to Cheng et al. [2016b] and Cheng and Yamamto [2016] for calibration and validation of the DE-GWS model under uniaxial and triaxial compression, whereas more details of the remote springs for modeling general tensile behavior can be found in Thoeni et al. [2013].

5.2.2 Characterization of stress state and interface behavior

Spatial distribution of principal stress

The average stress tensors are homogenized over the representative volumes by using the Love-Weber formula. Fig. 5.4 illustrates the distribution of principal stress directions based upon the homogenization performed over the representative volumes at different locations. Red, blue and green colors are used respectively to render the scales of major, medium and minor principal stresses (σ_1, σ_2 and σ_3). The DE-GWS model involved in Fig. 5.4 considers PP geotextile and uniaxial compression condition. It is found that the major principal stress directions stay paralleled to the short axis z during the entire loading course, with σ_1 decreasing from the middle to the edges. Before the minimum void ratio e_{min} is reached, the majority of medium and minor principal stress directions are kept aligned with the long axes x and y except for those around the corners as shown in Fig. 5.4a. As the compression proceeds, the medium principal stress directions become increasingly inclined to the $x = \pm y$ planes that lie perpendicular to the corner surface. The misalignment of medium and minor principal stress directions propagates to the middle part when the GWS reaches its full strength, as shown in Fig. 5.4b. The spatial distribution of principal stress directions presented here closely assembles those in the soil specimen in a cuboidal triaxial cell, because stress concentration cannot be avoided at the cell corners. Nevertheless, the local misalignment of medium and

minor principal stress directions can be balanced by homogenizing the stresses over the entire GWS volume.

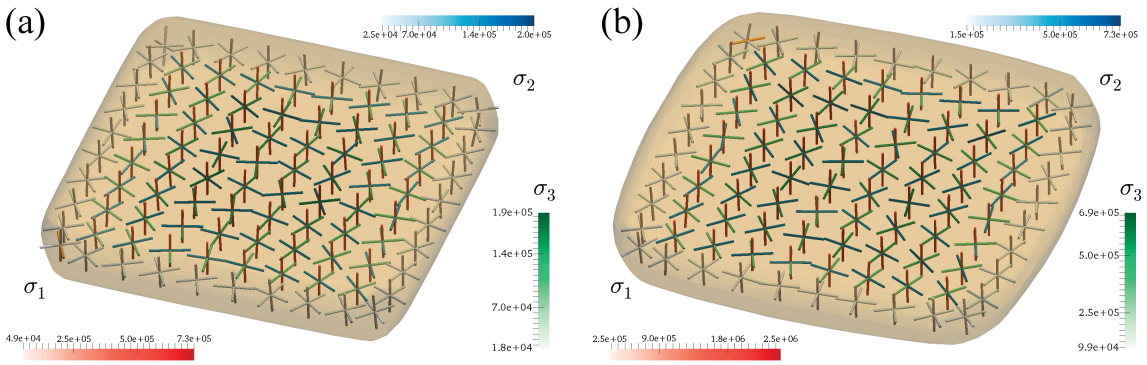

Fig. 5.4 Spatial distribution of principal stresses in GWS at (a) $e = e_{min}$ and (b) maximum σ_{am} states.

Interface friction

Considering a cuboidal shape for the DE-GWS model, the soil–geotextile interface friction can be computed as the ratio of tangential to normal stresses on a given interface. To avoid the canceling out of asymmetric shear components, the homogenization is performed on a quarter of the GWS volume. As explained in Cheng et al. [2016b], friction is more significant on the lateral soil–geotextile interfaces (yz- and zx-planes) than the horizontal interface (xy-plane). The friction angles on the lateral interfaces increase as the geotextile yarns break progressively, which is also true in the cases of drained triaxial compression (DTC, dashed lines) as shown in Fig. 5.5. Compared with the uniaxial compression (UC) cases (solid lines), the evolutions of interface frictions during drained triaxial compression is not stagnant in the pre–failure stage. This is because the geotextile fabrics at the initial stage of triaxial compression are not as strained as those under uniaxial compression. In both the uniaxial and triaxial compression conditions, the maximum levels of interface frictions are far less than the interfacial shear strength measured in shear box tests regardless of the tensile stiffness of geotextile [Cheng and Yamamoto, 2015a]. Therefore, it is safe to assume smooth soil–geotextile interfaces for GWS under compression in the analytical framework presented in Section 5.3.

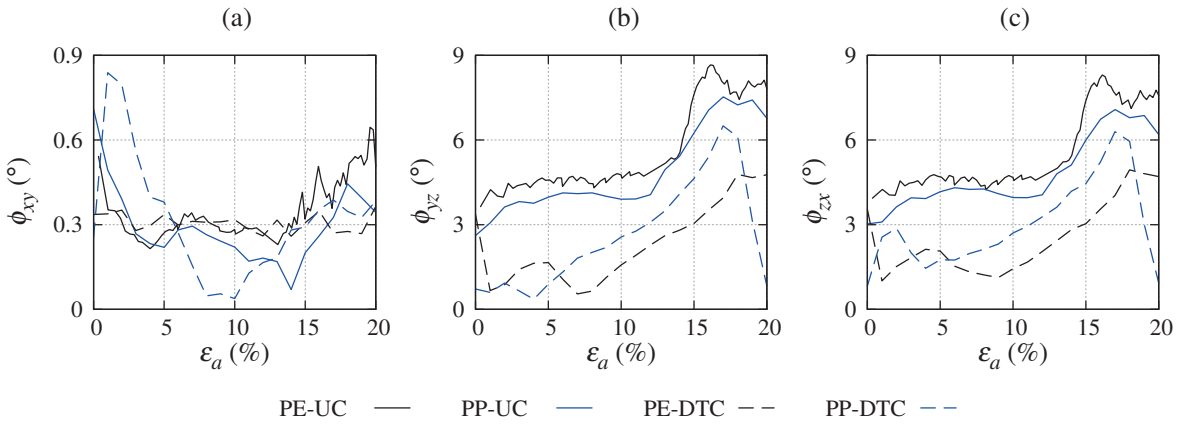

Fig. 5.5 Evolution of friction angles on soil–geotextile interfaces in (a) *xy*-, (b) *yz*- and (c) *zx*-planes.

5.2.3 Behaviors of constituent materials

It is of vital importance to understand the behaviors of the constituent soil and geotextile of GWS in deriving the stress-strain solutions for GWS. The prediction of volumetric change in the wrapped soil underpins the straining of geotextile fabrics, which in return provides the soil with greater confinement and interlocking. As a result, stress paths of distinctive features are experienced by the GWS. In addition to the soil behavior, this section attempts to relate the tensile response of geotextile to the GWS bearing strength. A variety of tensile stiffnesses are thus considered to investigate their effects on the constitutive behavior of the wrapped soil and the bearing capacity of the GWS under uniaxial compression.

Constitutive relation of soil

Fig. 5.6a–b summarize the respective e-p' relations and stress paths of the reinforced soils wrapped with PE, 0.5PP, PP, 2PP, 3PP and 4PP geotextiles. It is interesting to note that the evolutions of void ratios in all cases initially follow the same compression line before dilation manifests as shown in Fig. 5.6a. One can observe that this compression line for GWS under uniaxial compression is of a similar shape as the normal compression line for sand [O'Sullivan, 2011]. Fig. 5.6b verifies that the GWS stress paths consistently approach to the nonlinear failure state line (FSL) of the Toyoura sand ($e_0 = 0.68$) independent of the tensile stiffness of the geotextile, which elucidates all the e-p' curves initially following the

compression line in Fig. 5.6a. The failure principal stress ratio M_f on the FSL can be obtained from triaxial compression tests on the inside material [Sun et al., 2007]. Fig. 5.6c presents the ratio between deviatoric stress q and mean effective stress p' evolving towards the failure state in a semi-log scale. Once the failure state is attained, each p'-q/p' curve tends to align with the tangential direction along the FSL until the geotextile reinforcement starts to fail. The evolutions of the distances from the FSL to the p'-q/p' curves, in the following termed the near-failure states, are a family of parallel lines in the p'–$(M_f - q/p')$ plane. By replacing p' with the total deviatoric strain ε_d as the state variable, the near-failure state points in all cases collapse to a unique hyperbola as shown in Fig. 5.7. Therefore, as far as uniaxial or triaxial compression is concerned, the predictions of q/p' can be obtained from the near-failure state line (NFSL) and the FSL without reference to the tensile stiffness of geotextile.

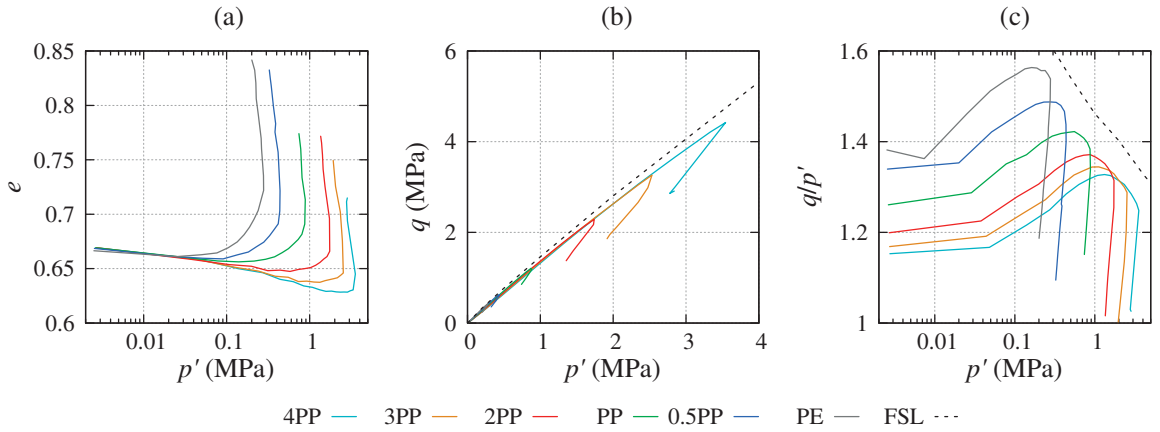

Fig. 5.6 Constitutive behaviors of wrapped soil in (a) p'-e and (b) p'-q planes, and (c) evolution of stress ratio q/p' versus mean stress p'.

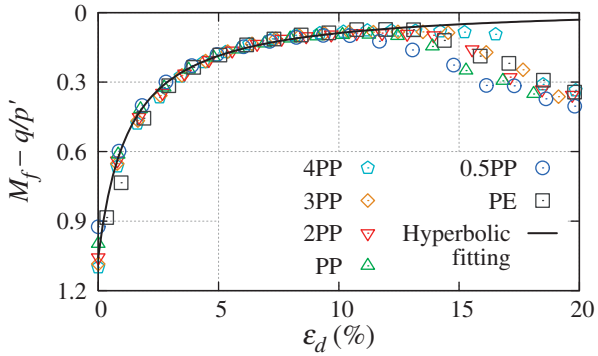

Fig. 5.7 Unique near-failure state line in ε_d-$(M_f - q/p')$ plane for GWS simulations with different geotextiles.

Tensile response of geotextile fabrics

The effects of the physical properties (tensile stiffness and interface friction, etc.) and the forms of geosynthetic reinforcements on soil behavior have been demonstrated experimentally [Indraratna et al., 2014; Lajevardi et al., 2015; Latha and Murthy, 2007; Palmeira, 2009; Tafreshi and Dawson, 2010], but their relationships are seldom discussed because of the versatility of geosynthetic reinforcements. As this work focuses on the closed cellular form of geosynthetic reinforcement, the relationships between surcharge loads and geotextile tensile stresses during compression are investigated considering the aforementioned range of geotextile tensile stiffnesses. Fig. 5.8 shows the relationships between surcharge loads Q versus the tensile stresses averaged along two sets of geotextile hoops, i.e. t_{hr} (dashed lines) and t_{ha} (solid lines). *hr* and *ha* represent respectively the hoops in the vertical and horizontal planes perpendicular to the lateral and vertical axes, as shown in Fig. 5.9. To better illustrate the tension-load relations, both the loads and the average tensile stresses are scaled with reference to the respective maximums of Q, t_{hr} and t_{ha} obtained in the PP case.

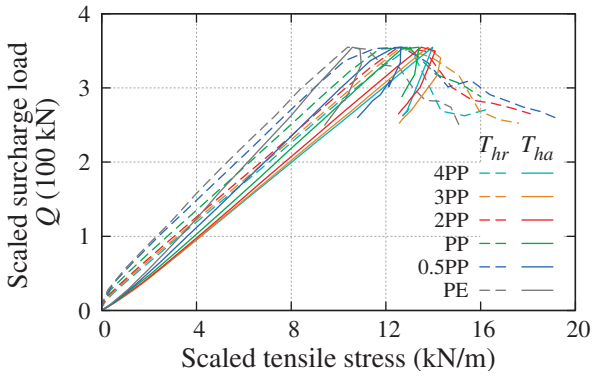

Fig. 5.8 Tensile stress-axial load relationships scaled to the PP case.

Fig. 5.8 reveals linear relationships between the tensile stresses and the surcharge loads before the geotextile fabrics are strained to failure. The evolutions of the scaled Q with respect to the scaled t_{hr} and t_{ha} lie very close to each other despite the difference in the geotextile tensile stiffness and the hoop directions. The above findings together with the principal stress ratio in the wrapped soil as a function of ε_d and p' suggest that the tensile stiffness of the wrapping geotextile has no impact on the relative values for the stresses within the soil and the geotextile under compression. Because the confinement from the geotextile encapsulation

is the only external load on the soil, the ratio between the additional vertical and lateral confining pressures is deemed independent of the tensile stiffness as well. Nevertheless, the stress magnitudes and ultimate bearing capacity during compression is apparently affected by the geotextile tensile stiffness, as demonstrated in Fig. 5.6b. It seems that the influence of such factor can be accounted for by a reasonable value for the Young's modulus of GWS.

5.3 An analytical model for geotextile-wrapped soil

As observed in both experiments and DEM simulations of uniaxial/triaxial compression, the sand-filled square geotextile container (length $B = 400$ mm and height $H = 80$ mm after initial compaction) does not have severely bulged lateral surfaces until the geotextile fabrics start to fail. Therefore, there is no need for a rigorous description of the container shape as in [Guo et al., 2015]. A cuboid should work properly as the assumed geometry for the analytical model of the wrapped soil and the geotextile encapsulation. Fig. 5.9 illustrates the external stresses σ_{as} and σ_{rs} applied from the vertical and lateral directions on the geotextile encapsulation, and those produced within the wrapped soil σ_a and σ_r. The equilibrium condition is satisfied by the tensile stresses, the external and internal confining stresses that are drawn on a quarter of the AN-GWS model, as shown in Fig. 5.9. With the new insights obtained from the DEM analysis in Section 5.2.3, the following fundamental assumptions are taken into account to facilitate the development of the analytical solution for GWS under compression:

(1) Stress state and boundary condition:

   a. The principal directions of the internal stresses within the wrapped soil are aligned with the vertical and lateral axes, neglecting the corner effect and interface friction.

   b. The internal stresses produced in the wrapped soil are uniformly distributed on all faces of the cuboidal analytical model.

(2) Soil behavior:

a. The initial contraction of the wrapped soil follows the compression line in the semi-log p'–e plane regardless of the tensile stiffness of the geotextile.

b. The principal stress ratio is predicted by a unique near-failure state line which describes the princial stress ratio converging to the failure state with respect to deviatoric strain.

c. The plastic behavior of the wrapped soil is governed by the Mohr-Coulomb yield criterion with an evolving dilation rate related with the principal stress ratio.

(3) Geotextile behavior:

a. The evolutions of the average tensile stresses and strains are the same along the hoops in the horizontal and vertical planes.

b. The geotextile behaves as a perfectly elastic material with the same tensile stiffness for every constituent hoop of the geotextile container.

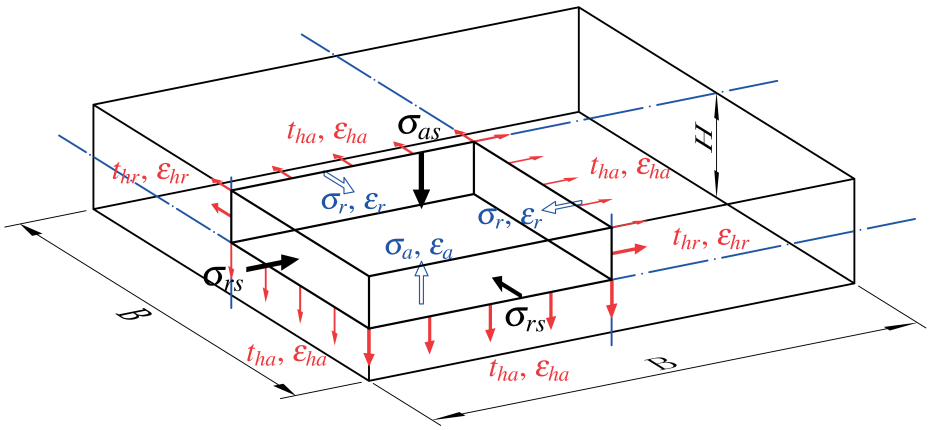

Fig. 5.9 Schematic illustration of stresses and strains in the analytical model of geotextile-wrapped soil.

5.3.1 A general framework for stress-strain relation under compression

In the case of geosynthetic-encased stone columns, additional lateral confinements are provided from the circumferential hoops in the horizontal plane. The equilibrium condition for the surrounding soil, stone columns and encasement is satisfied at the soil–column interfaces where the radial stress difference is taken by the geosynthetic encasement accordingly. In addition to the confinements from circumferential hoops, the GWS-type cellular reinforcement

introduces two additional sets of hoops in the lateral planes. As a result, both the vertical and lateral confinements are largely enhanced by the additional planar reinforcements [Cheng and Yamamto, 2016]. It is worth noting that the analytical solutions for the stone columns [Balaam and Booker, 1985; Pulko et al., 2011] require the same fundamental assumptions as the present analytical model, e.g. triaxial stress state and negligible interfacial shear. Analogous to the encased stone columns, the equilibrium equations of the wrapped soil can be expressed considering all the stresses and strains depicted schematically in Fig. 5.9. It follows:

$$\sigma_{as}B^2(1-\varepsilon_r)^2+4Bt_{hr}(1-\varepsilon_{ha})=\sigma_aB^2(1-\varepsilon_r)^2 \tag{5.1}$$

$$\sigma_{rs}BH(1-\varepsilon_r)(1-\varepsilon_a)+t_{ha}(2B+2H)(1-\varepsilon_{hr})=\sigma_rBH(1-\varepsilon_r)(1-\varepsilon_a) \tag{5.2}$$

where the average tensile strains ε_{ha} and ε_{hr} are linearly related to their respective stresses via the geotextile tensile stiffness J. The initial length B and height H of the cuboidal model are assumed to be 400 mm and 80 mm respectively, due to the negligible bulged lateral surfaces. In light of assumption 3(a) pertaining to the tensile stress distribution along the hoops, the subscripts *ha* and *hr* are reduced to *h* which denotes the tensile stress/strain along any hoop direction. Note as well that the relative movement at the soil–geotextile interfaces are allowed because of the approximation of the shape of the container using a cuboid. Hence, the elongation of the hoops ε_{ha} and ε_{hr} are assumed to be independent of the vertical and lateral strains ε_a and ε_r.

The expression for the surcharge σ_{as} as a function of the internal stresses and strains within the wrapped soil under uniaxial/triaxial compression reads

$$\sigma_{as}=K\sigma_r-\frac{2(\sigma_r-\sigma_{rs})(H/B)(1-\varepsilon_a)}{(H/B+1)(1-\varepsilon_r)} \tag{5.3}$$

where $K=\sigma_a/\sigma_r$ is the principal stress ratio within the wrapped soil domain which can be derived from q/p'. As stated in Section 5.2.3, q/p' can be calculated as the failure stress ratio M_f subtracted from the corresponding near-failure state variable M_f-q/p' at the same p' and ε_d,. The unique correlation between this new state variable M_f-q/p' and ε_d, as shown

Table 5.2 Parameters of the proposed analytical solution for geotextile-wrapped soil.

Compression line	Failure state line (FSL)	Near-failure state line (NFSL)	Stress-dilatancy relation	Young's modulus estimation
$C_t = 1.372$ $m = 0.3$ $p_a = 0.1$ MPa, $p_0 = 2.6$ kPa	$M = 1.35$ $n = 0.0723$ $p_c = 3.255$ MPa	$\kappa = 1.386$ $\lambda = 1.27$ $\xi = 0.035$	$p_1 = 1.68$ $p_2 = 0.344$	$\alpha = 26.1$ $\beta = 0.74$

in Fig. 5.7, can be formulated in a hyperbolic equation such as

$$M_f - q/p' = \frac{\kappa}{\varepsilon_d + \lambda} - \xi \tag{5.4}$$

with the corresponding parameters κ, λ and ξ listed in Table 5.2. The FSL, that the stress paths in Fig. 5.6b are approaching, is identical to the FSL of Toyoura sand ($e_0 = 0.68$). Hence, the following equations obtained from triaxial compression tests on Toyoura sand specimens [Wu et al., 2013; Yao et al., 2008] can as well be employed in the current analytical model of GWS:

$$M_f = q_f/p' = M(p'/p_c)^{-n} \tag{5.5}$$

where the parameters M, n and p_c used by Yao et al. [2008] are listed in Table 5.2.

Eq. 5.3 gives the general framework of the analytical solution for GWS under compression. It is not surprising to note that the terms involved with tensile stresses/strains are canceled out in Eq. 5.3. This is considered reasonable because the tensile stiffness of geotextile J has a marginal effect on the ratios amongst σ_a, σ_r, and σ_{as}, as shown in Fig. 5.6b and Fig. 5.8. In order to solve ε_a, ε_r and ε_h for a given surcharge history with Eq. 5.3, a suitable analytical model is needed to express the strains in terms of the internal stresses produced by the wrapped soil. Hence, the total strain tensor $\boldsymbol{\varepsilon}$ is decomposed into an elastic and a plastic part, i.e., $\boldsymbol{\varepsilon} = \boldsymbol{\varepsilon}^e + \boldsymbol{\varepsilon}^p$. Each part is calculated with the respective stress-strain relation that characterizes the contractive or dilative behavior of GWS respectively.

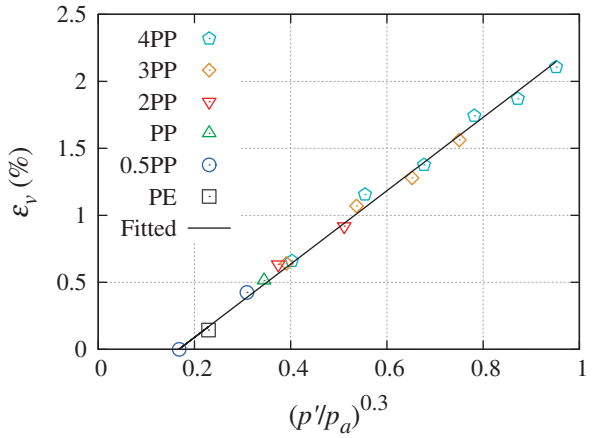

Fig. 5.10 Evolution of volumetric strain versus $(p'/p_a)^{0.3}$ before dilation occurs and the fitted compression line.

5.3.2 Initial elastic response

The evolution of void ratio initially following the compression line in Fig. 5.6a provides a basis for predicting the volumetric strain ε_v of GWS. Fig. 5.10 is produced by replotting the data in Fig. 5.6a on the ε_v–$(p'/p_a)^{0.3}$ plane, as was done by Nakai [1989] for sand in normal compression. The dilation parts are left out in particular to better illustrate the correlation. A unique straight line is thereby identified, to which the state points of all the six simulations collapse. This linear relationship facilitates the prediction of initial ε_v without special consideration given to the tensile stiffness of the geotextile. The contractive ε_v produced in GWS under the compression is assumed to be elastic/elastoplastic, as in most constitutive models of sand. The remaining plastic part is considered within the incremental stress-strain relationship for Mohr-Coulomb elastoplastic material. Though deviatoric strain is usually assumed to occur only in the plastic deformation regime, the current AN-GWS model allows elastic deviatoric strain ε_d^e to be produced during compression. Hence, using the same expression of normal compression line for sand Nakai [1989]; Wu et al. [2013]; Yao et al. [2008], the elastic volumetric and deviatoric strains ε_v^e and ε_d^e can be directly predicted from p' by

$$\varepsilon_v^e = C_t[(p'/p_a)^m - (p_0'/p_a)^m] \tag{5.6}$$

where m is a material constant which equals 0.3 for sand, p_a is the atmospheric pressure ($p_a = 0.1$ MPa), and the values of the compression index C_t and the initial mean stress p_0' are

obtained from the slope and intercept of the straight line in Fig. 5.10.

$$\varepsilon_d^e = \frac{2q(1+\upsilon)}{9p'(1-2\upsilon)}\varepsilon_v^e \tag{5.7}$$

where υ is the Poisson's ratio of the wrapped soil, and q/p' is predicted from p' on the FSL and NFSL which is the newly recognized state line for GWS-type reinforced sands. It is worth noting that the fitted value for p'_0, 2.6 kPa in the case of GWS, is very close to the mean effective stress in the unreinforced sand at the passive failure condition ($K_p = 5.25$) under a $\sigma_{as,0} = 5.635$ kPa surcharge. The same level of surcharge was applied as the initial compaction on the sand-filled geotextile container in the DEM and experimental uniaxial compression tests [Cheng et al., 2016b]. Therefore, it is postulated that the additional confining pressure from the geotextile encapsulation is negligible at the initial loading stage. It should be noted that the value of C_t given in Table 5.2 for the GWS is larger than 0.84 for Toyoura sand obtained from isotropic compression tests [Nakai, 1989]. Such difference could be possibly caused by the initial anisotropic stress and fabric states in the wrapped soil.

5.3.3 Incremental plastic response

With the elastic strains predicted by Eq. 5.6 and 5.7, the plastic stress-strain behavior of GWS remains to be solved by an analytical model that can consider the dilatancy of soil. According to Balaam and Booker [1985] and Pulko et al. [2011], a simplified solution can be obtained by assuming the stone columns kept at triaxial stress states during compression. It can be understood from the previous DEM analysis (Section 5.2.3) that the behavior of GWS satisfies the same assumptions applied in the analytical solution for the stone columns with geosynthetic encasement. Under uniaxial and triaxial compression, these two geomaterials are expected to undergo significant plastic dilation, which in return facilitates the confinement effect. The wrapped/encased geomaterials can be considered as perfectly elastoplastic solids satisfying the Mohr-Coulomb yield criterion. The plastic stress-strain relationship is written

incrementally as

$$\begin{Bmatrix} \mathrm{d}\sigma_a^p \\ \mathrm{d}\sigma_r^p \end{Bmatrix} = D \begin{bmatrix} K_\psi K' & 2K' \\ K_\psi & 2 \end{bmatrix} \begin{Bmatrix} \mathrm{d}\varepsilon_a^p \\ \mathrm{d}\varepsilon_r^p \end{Bmatrix} \tag{5.8}$$

where $\mathrm{d}\sigma_a^p$ and $\mathrm{d}\sigma_r^p$ are the vertical and lateral stress increments that produce the corresponding strain increments denoted as $\mathrm{d}\varepsilon_a^p$ and $\mathrm{d}\varepsilon_r^p$ respectively. The incremental stresses and strains are correlated via the material parameter D, the stress increment ratio K' and the strain increment ratio K_ψ which are defined respectively by

$$D = \frac{E}{2 + K_\psi K' - 2\upsilon(1 + K_\psi + K')} \tag{5.9}$$

$$K' = \frac{\mathrm{d}\sigma_a^p}{\mathrm{d}\sigma_r^p} = \frac{1+\sin\varphi}{1-\sin\varphi} = \frac{2\,\mathrm{d}q/\mathrm{d}p' + 3}{-\mathrm{d}q/\mathrm{d}p' + 3} \tag{5.10}$$

$$K_\psi = \frac{\mathrm{d}\varepsilon_r^p}{\mathrm{d}\varepsilon_a^p} = \frac{1+\sin\psi}{1-\sin\psi} = \frac{2\,\mathrm{d}\varepsilon_v^p/\mathrm{d}\varepsilon_d^p - 3}{2\,\mathrm{d}\varepsilon_v^p/\mathrm{d}\varepsilon_d^p + 6} \tag{5.11}$$

where φ is the peak friction angle, ψ is the dilation angle, and E is the Young's modulus of the reinforced geomaterial. In the original work of Balaam and Booker [1985], φ and ψ are assumed to be constant, which is not necessarily true for reinforced geomaterials due to their nonlinear nature, e.g. a nonlinear failure state line.

Prediction of principal stress and strain ratios

In the case of the geotextile-wrapped Toyoura sand, K' is calculated as the tangent of the nonlinear stress path like those in Fig. 5.6b. It has been demonstrated in Section 5.2.3 that the principal stress ratio of GWS under uniaxial compression can be obtained from the near-failure and failure states associated with the total deviatoric strain and the mean stress. Therefore, K' can be readily derived from the ratio of principal stress increments $\mathrm{d}q/\mathrm{d}p'$ via Eq. 5.10, regardless of the tensile stiffness of the geotextile.

The prediction of K_ψ or the dilation rate $-\mathrm{d}\varepsilon_v^p/\mathrm{d}\varepsilon_d^p$ requires an appropriate stress-dilatancy rule as in most soil models. The validated discrete element model [Cheng et al., 2016b] allows for thorough measures of key variables that are otherwise difficult to acquire in conventional laboratory testing, such as q/p' and $\mathrm{d}\varepsilon_v^p/\mathrm{d}\varepsilon_d^p$ in wrapped soil. Fig. 5.11

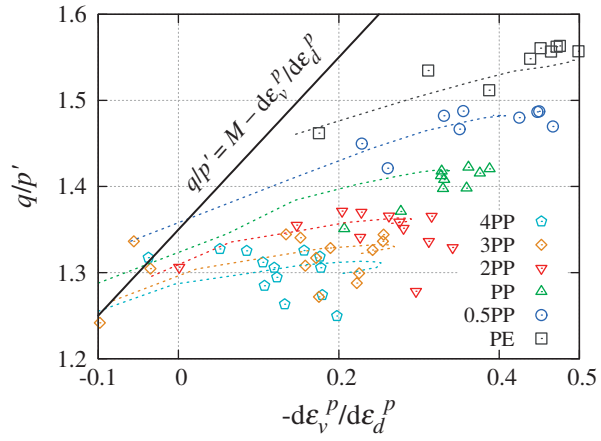

Fig. 5.11 Stress-dilatancy relationships for granular soil wrapped with different geotextiles measured in the DEM simulations (markers) and predicted by the analytical model (dashed lines).

plots the relationships between q/p' and $-\mathrm{d}\varepsilon_v^p/\mathrm{d}\varepsilon_d^p$ obtained from the six DEM simulations with various geotextile tensile stiffnesses. The post–failure parts are excluded in Fig. 5.11 to better illustrate the stress-dilatancy relations. It can be observed that the origins of all the $-\mathrm{d}\varepsilon_v^p/\mathrm{d}\varepsilon_d^p$-$q/p'$ curves are seemingly aligned along a unique straight line (solid black line). As $-\mathrm{d}\varepsilon_v^p/\mathrm{d}\varepsilon_d^p$ increases, the rates of increase for q/p' reduce in all the six simulations, approaching to their respective plateaus. Considering the straight line described by $q/p' = M - \mathrm{d}\varepsilon_v^p/\mathrm{d}\varepsilon_d^p$ as in the original Cam-clay model, the reference states can be defined for the stress-dilatancy relation of GWS with the stress ratio at failure $M_f = q_f/p'$ and the corresponding dilation rate $D_f^p = (-\mathrm{d}\varepsilon_v^p/\mathrm{d}\varepsilon_d^p)_f = M_f - M$. Similar to the way that near-failure stress states are defined in Fig. 5.7, both the stress ratios and dilation rates in each simulation case are regulated with respect to the reference states M_f and D_f^p produced at the same ε_d and p' as shown in Fig. 5.12. It seems that all the regulated state points are located near a straight line in the $(D_f^p + \mathrm{d}\varepsilon_v^p/\mathrm{d}\varepsilon_d^p)$–$(M_f - q/p')$ plane. Therefore, the dilation rate $-\mathrm{d}\varepsilon_v^p/\mathrm{d}\varepsilon_d^p$ can be predicted using $M_f - q/p'$ (Eq. 5.4) through a linear correlation:

$$-\mathrm{d}\varepsilon_v^p/\mathrm{d}\varepsilon_d^p = D_f^p - [p_1(M_f - q/p') - p_2] \tag{5.12}$$

with the parameters p_1 and p_2 given in Table 5.2. As can be seen in Fig. 5.11, good agreement is obtained between the predicted stress-dilatancy relationships and the measurements obtained from the DEM simulations of GWS considering different geotextile tensile stiffnesses.

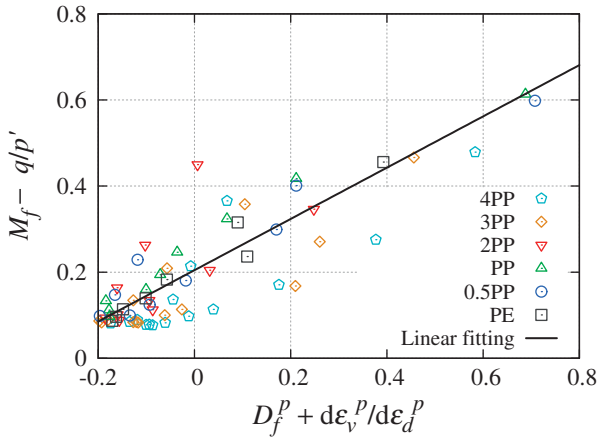

Fig. 5.12 Unique relationship between the relative states of principal stress ratio and dilation rate with respect to their failure values.

Relationship between tensile stiffness of geotextile and Young's modulus of wrapped soil

As discussed in Section 5.2.3, the tensile stiffness of the geotextile seems to only affect the magnitude of the stresses, but not the ratios among them. Hence, it is reasonable to take into account the influence of the tensile stiffness of the geotextile within the Young's modulus of the wrapped soil. Writing the stress increments in terms of $\mathrm{d}p'$ and K' and substituting Eq. 5.9 for D in Eq. 5.8 results in the plastic stress-strain relation as follows:

$$\mathrm{d}\varepsilon_a^p = \frac{\mathrm{d}\varepsilon_r^p}{K_\psi} = \frac{1}{E}\mathrm{d}p^* \tag{5.13}$$

with

$$\mathrm{d}p^* = \frac{2 + K_\psi K' - 2\upsilon(1 + K_\psi + K')}{K_\psi(K' + 2)}\mathrm{d}p' \tag{5.14}$$

where the material parameters K' and K_ψ are calculated from $\mathrm{d}q/\mathrm{d}p'$ and $\mathrm{d}\varepsilon_v^p/\mathrm{d}\varepsilon_d^p$ via Eqs. 5.10–5.11. Plotting $\mathrm{d}\varepsilon_a^p$ against the generalized mean stress increment $\mathrm{d}p^*$ defined by Eq. 5.14 presents a group of linear relationships, as shown in Fig. 5.13. These measurements

obtained from the DEM simulations in Fig. 5.13 further confirm the validity of applying Eq. 5.13 for the dilative behavior of GWS-type reinforced geomaterials. Fig. 5.14 plots the slope of the straight line in each simulation case against the corresponding geotextile tensile stiffness. A clear power-law relation $E = \alpha J^{\beta}$ is identified between the tensile stiffness of geotextile (10^3 kN/m) and the Young's modulus of wrapped soil (MPa). The material constants α and β are listed in Table 5.2.

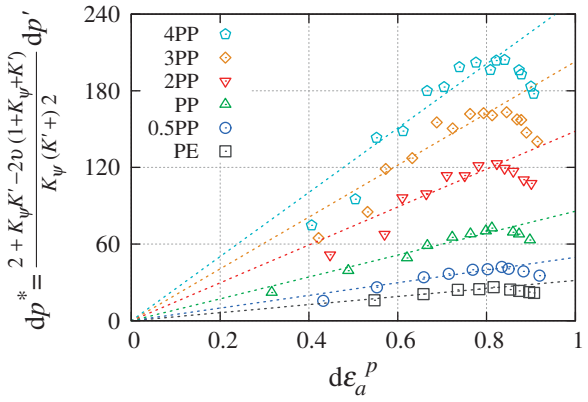

Fig. 5.13 Relationships between plastic vertical strain increment and generalized mean stress increment measured in the DEM simulations (markers) and predicted by the analytical model (dashed lines).

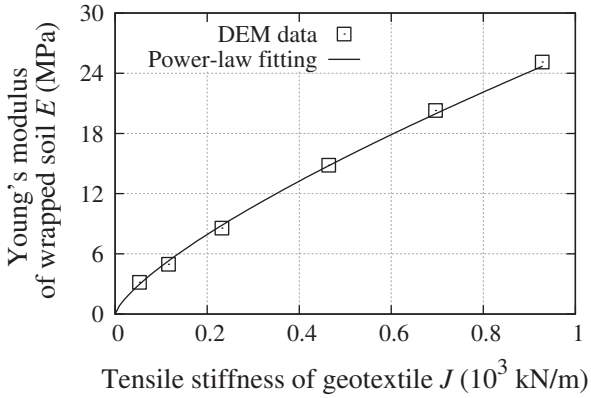

Fig. 5.14 Empirical relationship between tensile stiffness of geotextile and Young's modulus of wrapped soil.

5.3.4 Complete elastoplastic solution for geotextile-wrapped soil

The complete stress-strain response of the GWS under compression loading conditions is obtained with its contractive and dilative parts computed in Eqs. 5.6, 5.7 and 5.13. The

contractive volumetric strain of GWS ε_v^e is assumed elastic, and thus can be predicted from the compression line upon a given mean stress (Eq. 5.6). The elastic deviatoric strain ε_d^e is introduced (Eq. 5.7) in addition to ε_v^e, which differs from the assumption for deviatoric strain in some constitutive models. Nevertheless, the measurements of plastic strain increments, having ε_d^e excluded, show linear correlation with the generalized mean stress (see Fig. 5.13) as suggested in Eq. 5.13. This verifies the validity of assuming deviatoric strain in the elastic deformation regime. Thereby, the feasibility of adapting the plastic solution for the encased stones to the wrapped soil is confirmed.

For the sake of completeness, Eq. 5.15 is rewritten below from Eq. 5.3 with the strains split into the elastic and plastic parts. It should be noted that by substituting the respective equations for elastic vertical strain ε_a^e, elastic lateral strain ε_r^e, plastic vertical strain increment $\mathrm{d}\varepsilon_a^p$ and plastic lateral strain increment $\mathrm{d}\varepsilon_r^p$ into Eq. 5.15, the analytical solution for GWS under a given vertical surcharge history is simplified into a problem of solving the nonlinear equation $f(p', \mathrm{d}p', \varepsilon_d) - \sigma_{as} = 0$.

$$\sigma_{as} = K\sigma_r - \frac{2(\sigma_r - \sigma_{rs})(H/B)(1 - \varepsilon_a^e - \int \mathrm{d}\varepsilon_a^p)}{(H/B+1)(1 - \varepsilon_r^e - \int \mathrm{d}\varepsilon_r^p)} \tag{5.15}$$

$$\varepsilon_h = \frac{(\sigma_r - \sigma_{rs})(H/B)(1 - \varepsilon_a^e - \int \mathrm{d}\varepsilon_r^p)(1 - \varepsilon_r^e - \int \mathrm{d}\varepsilon_r^p)}{2J(H/B+1)} \tag{5.16}$$

ε_d is involved in the calculation of $M_f - q/p'$ which is given by Eq. 5.4 and later used for predicting K_ψ. The integrations of the plastic strain increments $\mathrm{d}\varepsilon_a^p$ and $\mathrm{d}\varepsilon_r^p$ have to be performed numerically, assuming p' and ε_d unchanged at an infinitesimally small increment of σ_{as}. Thence, all the incremental stress and strain variables as well as the above material parameters can be expressed in terms of $\mathrm{d}p'$ at an infinitesimal surcharge increment. By doing so, the nonlinear equation with $\mathrm{d}p'$ as the only variable can be solved numerically by an appropriate root finding algorithm. The predicted $\mathrm{d}p'$ and p' are then returned into Eqs. 5.6, 5.7 and 5.13 to update the elastic and plastic strains. Prior to solving $\mathrm{d}p'$ at each increment of σ_{as}, the material parameters, K, K' and K_ψ, need to be revised from the preceding stress and strain levels. To obtain the evolution of the tensile strain ε_h along the geotextile hoops, Eq. 5.1 is rewritten as Eq. 5.16 considering $t_h = J\varepsilon_h$. As the surcharge level rises, the tensile

stress t_h can be computed from the stresses and strains in the wrapped soil until ε_h reaches the maximum value as illustrated in Fig. 5.2. The integration will then stop, having the ultimate bearing capacity and the final settlement predicted for the Toyoura sand-filled geotextile container.

5.4 Model validity

In the engineering applications of GWS, initial compaction is usually conducted on the assemblies of sand-filled containers to attain an initial compressive strength [Matsuoka and Liu, 2006]. Gaps between neighboring containers are either left empty or filled with loose sands to facilitate the compaction process. Instead of empirically evaluated from the compactness, the initial strength can be predicted by the proposed analytical solution for GWS considering the designated initial settlement and lateral spreading of the sand-filled containers. To test the validity of the proposed analytical solution for GWS, the macroscopic responses of the DE-GWS model and the AN-GWS model under uniaxial compression loading conditions are compared considering the aforementioned geotextiles (denoted as PE, 0.5PP, PP, 2PP, 3PP, 4PP). The tensile behavior of geotextile is assumed purely elastic in the analytical model with the secant stiffness taken as J, whereas the nonlinearity in the tensile behavior is rigorously considered in the DEM simulations. It should be noted that the tensile stiffness of woven geotextiles in engineering applications does not usually exceed 1000 kN/m (4PP). The above range of tensile stiffnesses should be sufficient for demonstrating the applicability of the proposed analytical model in the engineering design of GWS-reinforced foundations. In the DEM simulations, the average tensile stress in the geotextile fabrics at the global failure of the GWS reached approximately half of the tensile strength, owing to the drawbacks of discretizing the thin geotextile (0.39 mm) with relatively large spherical particles in the diameter of 5 mm [Cheng et al., 2016b], as illustrated in Fig. 5.1c .To better compare with the DEM simulation results, the tensile strengths are therefore scaled by 0.5 in the analytical model.

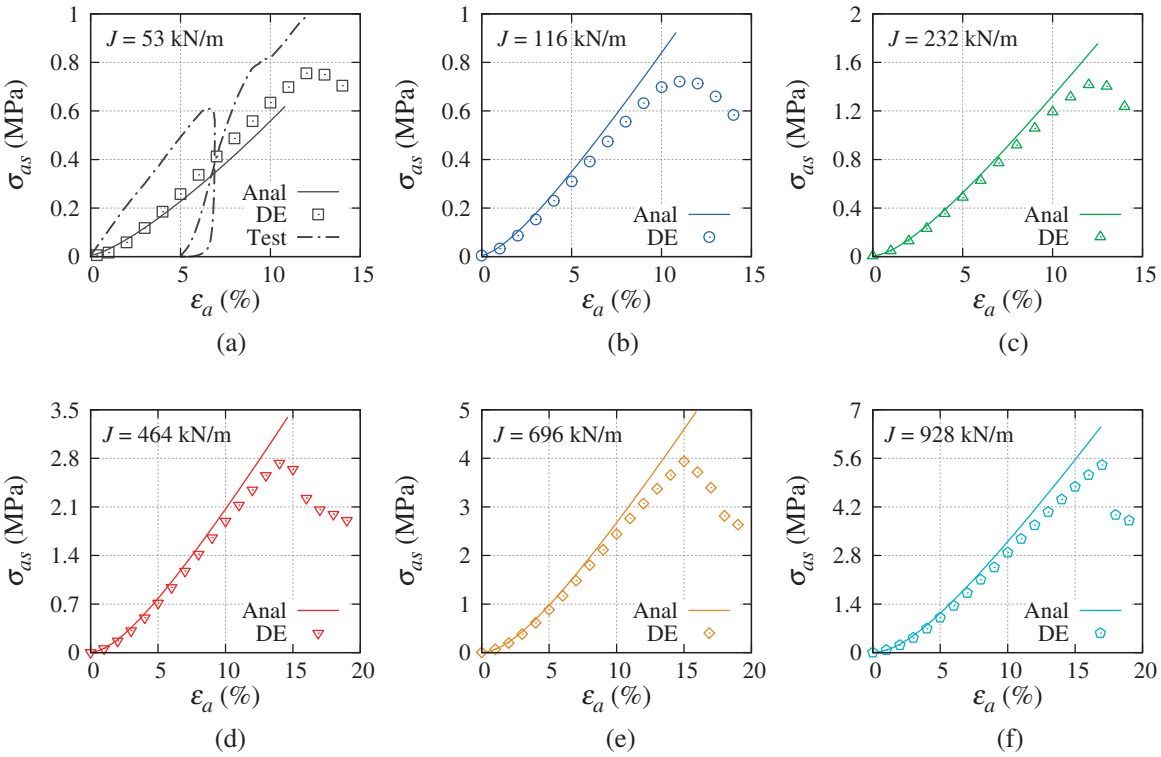

Fig. 5.15 Comparison of vertical surcharge-strain relationships predicted by the analytical and DEM model of granular soil wrapped by (a) PE, (b) 0.5PP, (c) PP, (d) 2PP, (e) 3PP and (f) 4PP geotextiles.

Fig. 5.15 shows the relationships between vertical surcharge pressure on the sand-filled container σ_{as} and total vertical strain ε_a obtained from the analytical and DEM models of GWS, considering different values for the geotextile tensile stiffness. An additional experimental response of the surcharge load on a sand-filled PE geotextile container is provided in Fig. 5.15a to demonstrate the validity of the analytical model. Because the area of the top surface was enlarged during the experiments, stresses in Fig. 5.15a are calculated as the load Q divided by the reference area $A = 0.16$. The proposed analytical solutions are in very good agreement with the DEM simulation results, regardless of the tensile stiffness. Notably, the hardening of the wrapped soil is well reproduced by the proposed analytical model, as can bee seen from all the stress-strain responses in Fig. 5.15. Because the nonlinearity of the geotextile tensile behavior is ignored in the AN-GWS model, the ultimate bearing capacities obtained from the two approaches are not exactly the same. Nevertheless, both the analytical model and the DEM model produce the same final settlements which are found to increase as the wrapping geotextile becomes stronger.

5.4.1 Stress-strain relation of wrapped soil

The internal stress-strain behavior of the wrapped soil and its relation to the tensile strain in the geotextile are of particular interest to the soil–geotextile interaction problems. The previous DEM simulations measured the additional confining pressure applied on the wrapped soil, and found that the confinement is evolving towards a more isotropic state during uniaxial compression. Based upon the new insights obtained from the DEM analysis in Section 5.2, the proposed analytical model is capable of accurately predicting the evolutions of the internal stresses as shown in Fig. 5.16. Similar to σ_{as} in Fig. 5.15, both the responses of σ_a and σ_r exhibit obvious hardening behavior before behaving linearly with respect to ε_a. Comparing the stress levels in Fig. 5.15 and 5.16a, one can confirm the presence of the additional vertical confinement contributed by the geotextile hoops in the lateral planes. Similarly, the additional lateral confinement produced by the hoops in both the lateral and horizontal planes can be understood from Fig 5.16b. Though good agreement is reached between the analytical and DEM solutions for the internal stresses, it is found that the DEM solutions tend to slightly surpass the corresponding analytical solutions in the cases where the strong geotextiles are considered.

5.4.2 Relationship between tensile behavior of geotextile and surcharge pressure on wrapped soil

Analogous to Fig. 5.8 which displays a unique correlation between tensile stresses and surcharge load regardless of the tensile stiffness of the geotextile, Fig. 5.16c presents a family of straight lines for the analytically obtained relations between tensile strain ε_h and the scaled surcharge pressure σ_{as}/J. J takes the respective geotextile tensile stiffness corresponding to each ε_h-σ_{as} curve. Because a universal tensile stress-strain law is considered for tensile stress along any hoop direction in the analytical model, the DEM solutions for the two tensile strains ε_{ha} and ε_{hr} are averaged to compare with the analytical solution for ε_h. The analytical model assumes elastic tensile behavior of the geotextile, resulting in linear relationships between ε_h and σ_{as}/J. The DEM model, on the other hand, thoroughly considers the nonlinearity

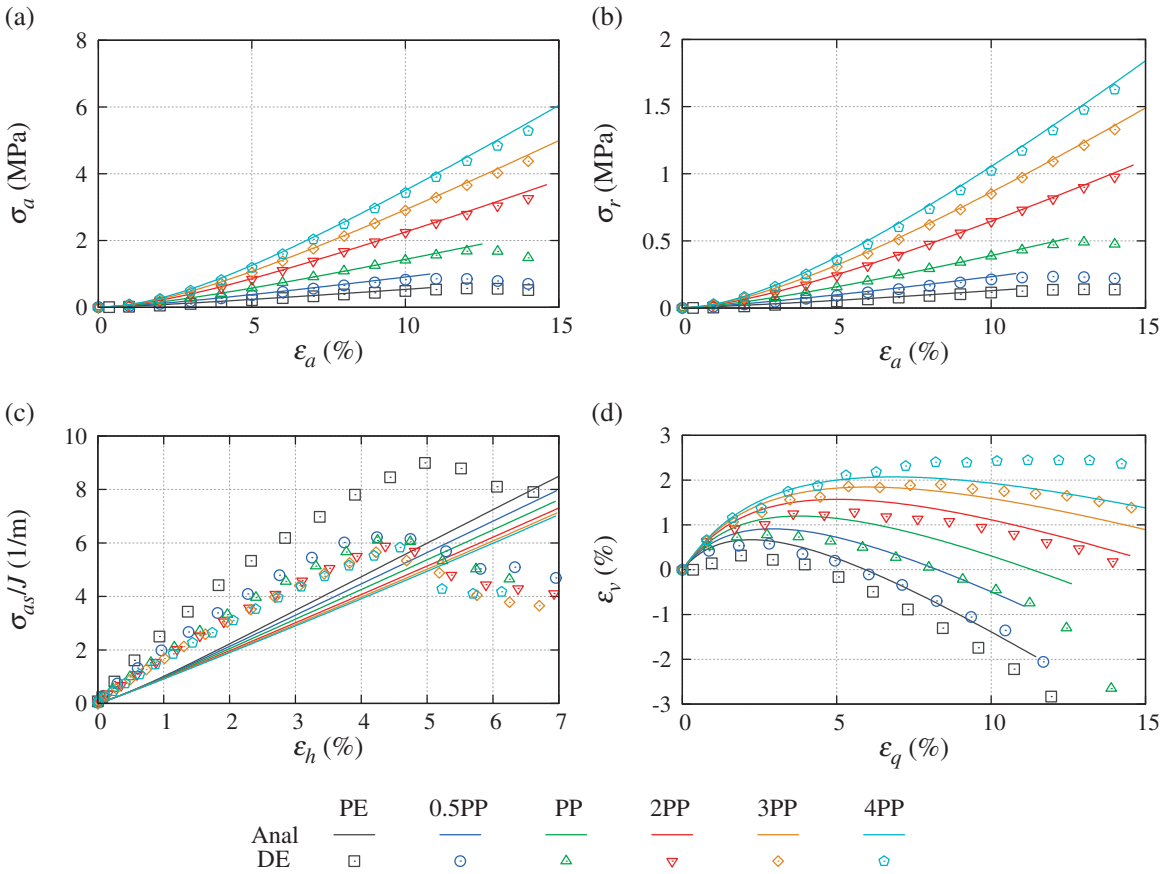

Fig. 5.16 Comparison of evolutions of internal (a) vertical and (b) lateral stresses versus vertical strain, (c) vertical surcharge pressure scaled with tensile stiffness of geotextile versus tensile strain, and (d) volumetric strain versus deviatoric strain.

of the tensile behavior and thus yields a family of nonlinear ε_h-(σ_{as}/J) curves which lie slightly above the analytical solutions. It is found that the slope of the curve in Fig. 5.16c either produced by the DEM model or the analytical model reduces with the increase of the geotextile tensile stiffness. It seems that the slope of the σ_{as}/J-ε_h curves will ultimately converge to a constant after the geotextile tensile stiffness exceeds a sufficiently large value. This trend suggests that wrapping soils with weak geotextiles results in higher efficiency on the reinforcement effect σ_{as}/J than with the strong ones, as long as the geotextile fabrics remain intact. From the perspective of sustainable design of GWS-reinforced foundations, it is vitally important to balance the reinforcing efficiency, the allowable settlement and the cost for high strength geotextiles. This comprehensive work could be accomplished with the help of the proposed analytical solution for GWS-like reinforced geomaterials.

5.4.3 Volumetric deformation

The best agreement between the analytical and DEM solutions for the volumetric response is obtained for the PE case, as shown in Fig. 5.16d. With the increase of the tensile stiffness of the geotextile, the volumetric behavior of the AN-GWS model is predicted to be more increasingly dilative than that in the DEM simulations (see 3PP and 4PP cases in particular). This is because the assumption of correlating the generalized mean stress $\mathrm{d}p^*$ with the plastic strain increment $\mathrm{d}\varepsilon_a^p$ or $\mathrm{d}\varepsilon_r^p$ via the Young's modulus E (Eq. 5.13) does not hold for the strong geotextile cases, as shown in Fig. 5.13. For the granular soil wrapped within the 2PP, 3PP and 4PP geotextile containers, intercepts could be introduced to fit the DEM simulation data with some linear equations. However, it seems more reasonable to avoid these intercepts by introducing an additional plastic deviatoric strain ε_d^p in the contractive deformation regime and excluding the increments of this ε_d^p from the plastic strain increments used in Fig. 5.13.

5.5 Analytical solution for geotextile-wrapped soil in triaxial loading condition

The assemblies of sand-filled containers are subjected to lateral earth pressures, when applied in the constructions of retaining walls [Tatsuoka et al., 2007], roads [Matsuoka et al., 2010] and channel slope [Liu et al., 2015]. To examine the predictive capacity of the proposed analytical solution in such loading scenarios, triaxial compression conditions are employed on the AN-GWS model. Though the analytical solution is derived based on a wide range of geotextile tensile stiffnesses, it is still needed to examine the analytical solution by additional GWS cases in which the geotextile tensile stiffnesses are beyond the above-mentioned range.Therefore, three types of geotextiles are taken into account: the most commonly used PE and PP geotextiles, and a strong geotextile with five times tensile stiffness of the PP geotextile (denoted as 5PP). The DEM simulations of triaxial loading on GWS are performed by enclosing the DE-GWS model within a periodic cell as explained in Section 5.2 and illustrated schematically in Fig. 5.1b. Three lateral confining pressures applied from the

exterior of the DE-GWS model (σ_{rs} = 10, 50 and 100 kPa) are considered for the triaxial compression tests. In the DEM simulations, it is straight forward to apply initial isotropic confining pressure before triaxial shearing. In the analytical model, however, p'_0 is assumed to develop from the same initial value as in the uniaxial compression tests ($p'_0 = 2.6$ kPa), instead of starting with the isotropic stress σ_{rs}. This shortcoming is due to the fact that the assumptions for the proposed analytical solution are derived based on the stress-strain responses under uniaxial compression. Those assumptions as stated in Section 5.3 may not remain valid for triaxial compression conditions. Notably, the assumption of principal stress ratio governed by the NFSL and FSL, though being largely valid during triaxial shearing, cannot consider isotropic stress states [Cheng and Yamamto, 2016]. Despite the fundamental difference in the evolution of stress states, the proposed analytical model is employed herein without any assumption pertaining to the triaxial stress-strain behavior of GWS.

5.5.1 Surcharge pressure

Despite the aforementioned difference in the initial stress states, the analytical solutions for surcharge pressure on GWS under triaxial compression generally agree with the DEM simulation results as shown in Fig. 5.17. The agreement is found to be improving with the increase of geotextile tensile stiffness, because the relations between ε_a and σ_{as} in the cases of stronger geotextiles exhibit more linearity and are less sensitive to confining pressure σ_{rs} as shown in Fig. 5.17b–c. It should be noted that this σ_{rs}-sensitive characteristic of GWS can be reproduced by the analytical model, though not as significant as in the DEM simulations (see Fig. 5.18a). As the confining pressure increases, both the analytical and DEM solutions give greater ultimate bearing capacities and final settlements for each GWS. By reducing the tensile strength of each geotextile by two, i.e. using half the strength, good agreement is obtained between the analytical and DEM solutions for the final settlements. The ultimate bearing capacity, however, seems to be increasingly overestimated by the analytical model with the increase of the geotextile tensile stiffness. This is because σ_{as} in the DEM simulations is averaged in the periodic cells which contain both the enclosed GWS and the surrounding soil particles, whereas the analytical model does not take the surrounding soil into account.

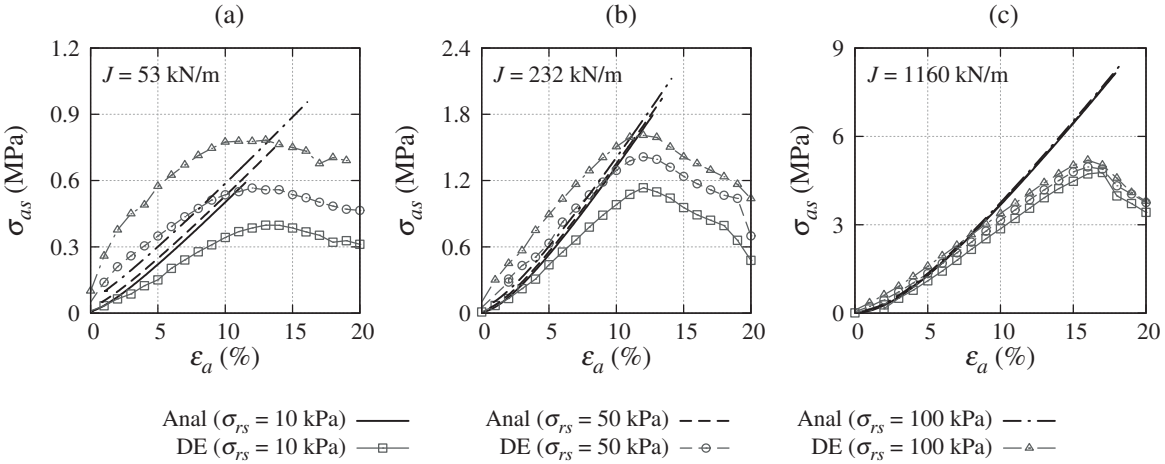

Fig. 5.17 Comparison of evolutions of vertical surcharge predicted by the analytical and DEM model of granular soil wrapped with (a) PE, (b) PP and (c) 5PP geotextiles.

5.5.2 Internal stresses

The responses of the internal stresses σ_a and σ_r appear to be influenced by confining pressure and geotextile tensile stiffness in similar manner as the responses of σ_{as}. The initial values for the analytical predictions of σ_r are underestimated because p'_0 is assumed to start from 2.6 kPa, which is most distinct in the PE case with 100 KPa confining pressure. With the increase of geotextile tensile stiffness, better agreement is observed between the analytical and DEM solutions for the σ_r responses (see Fig. 5.19b–c). Because σ_a is several times larger than σ_r, the initial difference between the σ_a responses predicted by the two solution methods are less significant compared with the σ_r responses, as shown in Fig. 5.18a and Fig. 5.19a. Nevertheless, the initial nonlinearity of the σ_a responses in the DEM simulations is not reproduced by the analytical model as shown in Fig. 5.18a. It is known that the stress in wrapped soil under triaxial compression starts from a drained triaxial loading path ($q/p' = 3$) and as the stress level increases, the principal stress ratio gradually evolves towards the values at failure states [Cheng and Yamamto, 2016]. The aforementioned initial nonlinearity of the σ_a responses is a direct result of the evolution of stress ratio with the increase of mean stress. Because the initial stress path is not considered in the proposed analytical model, good agreement with the DEM simulation results cannot be obtained for the soils wrapped by weak geotextile under triaxial compression. Comparing all the stress-strain responses in Figs. 5.17, 5.18 and 5.19, one can observe the best agreement between the analytical and DEM solutions

for the 5PP case. The assumption of principal stress ratios in Section 5.3 are sufficiently satisfied for the granular soil wrapped by strong geotextiles. In fact, the additional confining stresses $\sigma_a - \sigma_{as}$ and $\sigma_r - \sigma_{rs}$ in the PE case is only marginal, and the stress state requires more vertical strain to reach the FSL compared with those in the other cases. Despite the initial difference, the responses of σ_a and σ_r obtained from both solution methods are found to attain similar maximums eventually. Compared with the predictions of ultimate bearing capacities, the differences are less pronounced between the analytical and DEM solutions for the internal stress maximums in Fig. 5.18 and 5.19. As the geotextile tensile stiffness increases, it is found that the analytically predicted maximums of σ_a and σ_r increasingly surpass those in the DEM simulations. This is mainly attributed to less dilation produced in the analytical model than in the DEM model under triaxial compression, as can be observed in Fig. 5.20.

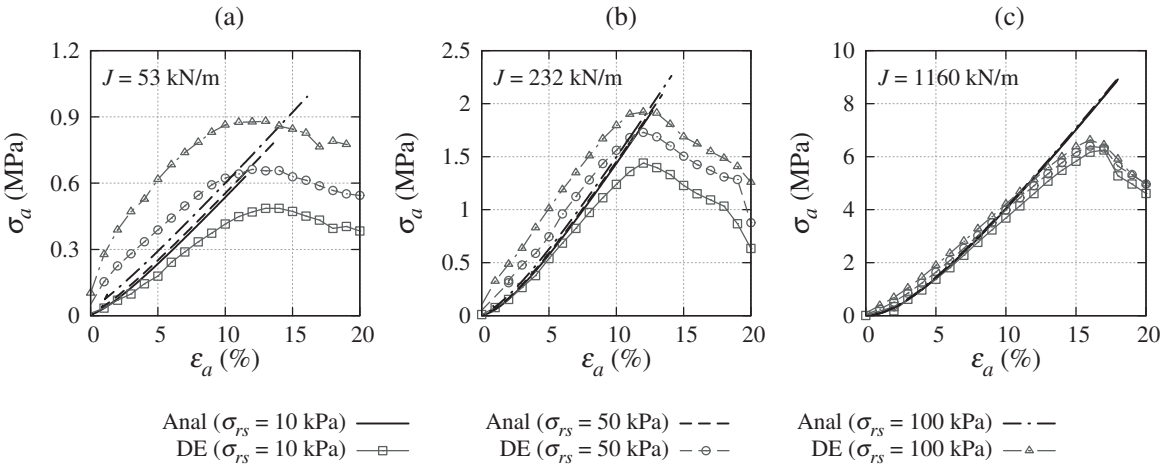

Fig. 5.18 Evolutions of internal vertical stress predicted by the analytical and DEM model of granular soil wrapped with (a) PE, (b) PP and (c) 5PP geotextiles.

5.5.3 Volumetric behavior

The volumetric behaviors of the GWS considering PE, PP and 5PP geotextiles under three confining pressures are given in Fig. 5.20. The analytical solutions for the volumetric response in the PE case match well with the DEM simulation results. With the increase of geotextile tensile stiffness, the proposed analytical solution predicts more contraction than the DEM modeling approach. Regardless of the solution methods, the volumetric behavior tends

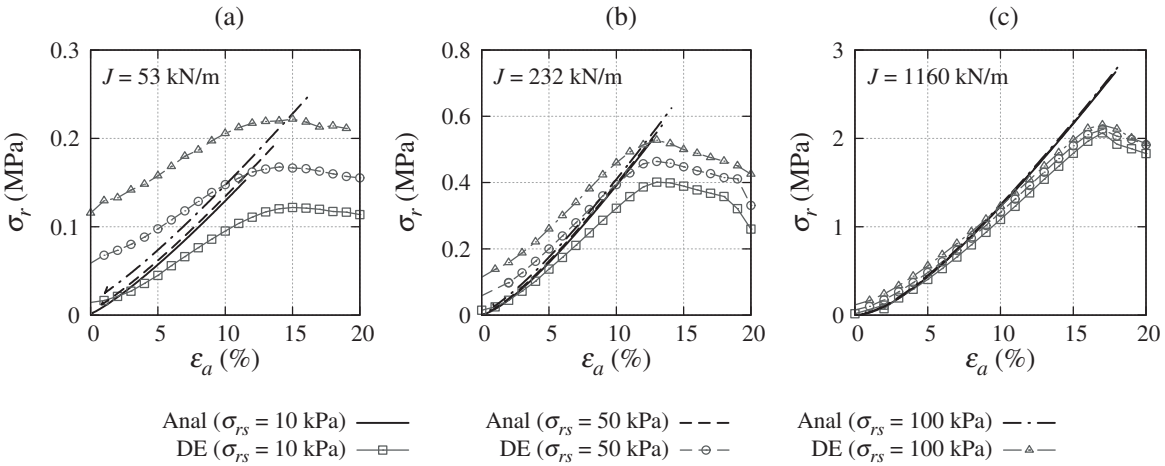

Fig. 5.19 Comparison of evolutions of internal lateral stress predicted by the analytical and DEM model of granular soil wrapped with (a) PE, (b) PP and (c) 5PP geotextiles.

to become more contractive with the increase of both confining pressure and geotextile tensile stiffness. The dilation rates of the volumetric responses seem to be unchanged with respect to confining pressure and geotextile tensile stiffness in the DEM simulations under triaxial compression. The analytical predictions of the volumetric behavior, however, shows a tendency of decreasing dilation rate with the increase of geotextile tensile stiffness. The reason for this tendency is that the proposed analytical solution assumes the dilation rate to be related with the principal stress ratio which is expected to reduce with increasing mean stress level. To attain good prediction accuracy in the volumetric behavior, future works are needed to unify the assumptions on the stress states and the stress-dilatancy relations of GWS for both uniaxial and triaxal compression loading conditions.

5.6 Conclusions

This chapter presents a novel analytical solution for geotextile-wrapped soil in compression loading conditions, with the assumptions facilitated by the new findings obtained from the DEM modeling of a sand-filled container. The analytical model considers the tensile behavior of geotextile to be purely elastic, and the wrapped soil as a Mohr-Coulomb elastoplastic solid with evolving principal stress ratio and dilation rate. To examine the boundary and interface assumption for the proposed analytical model, principal stress distribution and interface

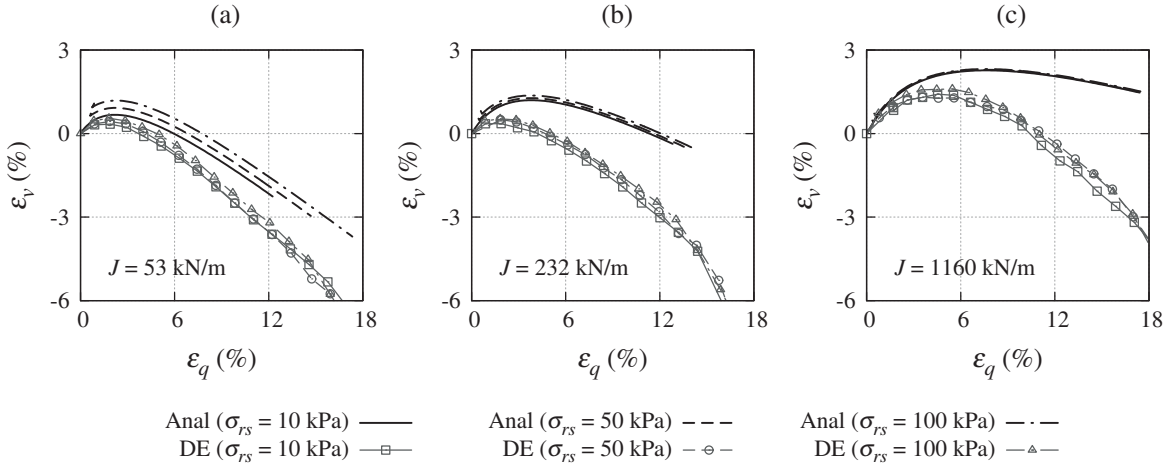

Fig. 5.20 Comparison of relationships between deviatoric strain and volumetric strain predicted by the analytical and DEM model of granular soil wrapped with (a) PE, (b) PP and (c) 5PP geotextiles.

friction are investigated in a DEM analysis of geotextile-wrapped soil under uniaxial and triaxial compression. For better understanding of the stress-strain behavior of the reinforced soil and its relation to tension in the geotextile fabrics, four additional cases are considered for the uniaxial compression simulations with the tensile stiffnesses half, two, three and four times that of a PP geotextile. The assumptions for the analytical model are made based upon the following findings from the DEM analysis:

- *Boundary conditions:* The major principal stress directions stay paralleled to the axis of the uniaxial loading. The medium and minor principal stress directions are slightly inclined towards the corners.

- *Contractive behavior of soil:* The initial contraction of wrapped soil follows the compression line in the semi-log mean stress–void ratio plane without reference to geotextile tensile stiffness.

- *Dilative behavior of soil:* The plastic deformation of the wrapped soil is governed by the Mohr-Coulomb yield criterion with evolving dilation rate and principal stress ratio.

- *Stress ratio:* A unique relationship is identified between deviatoric strain and the relative principal stress ratio with respect to the maximum value at failure state. The failure state lines for soils with or without cellular form of reinforcement are identical.

- *Dilation rate:* The principal stress ratio and its maximum on the failure line are related to dilation rate through a linear correlation irrespective of geotextile tensile stiffness.

- *Tensile behavior of geotextile:* The geotextile behaves as a perfectly elastic material with the same amount of tension developed in every constituent hoop of the geotextile reinforcement.

Because the material parameters need to be updated during compression loading, the analytical solution for geotextile-wrapped soil is solved numerically. By imposing an empirical power-law relation between the geotextile tensile stiffness and the Young's modulus of the wrapped soil, good agreement is obtained between the analytical and DEM solutions for geotextile-wrapped soil in uniaxial loading condition. The predictive capacity of the proposed analytical solution is further examined in triaxial compression conditions, varying the confining pressure and geotextile tensile stiffness at three different levels. Based on the analytical solutions and comparative DEM simulations the following conclusions are made:

- The analytical solutions for the internal stresses within the reinforced soil and the vertical surcharge applied on the geotextile are in excellent agreement with the DEM solutions regardless of geotextile tensile stiffness.

- The strain hardening of the geotextile-wrapped soil in the responses of the internal stress and the external surcharge pressure is well reproduced by the analytical model.

- The slope of the straight line that displays the linear relationship between the surcharge pressure and the tensile stress tends to reduce to a constant value with the increase of the geotextile tensile stiffness. This trend suggests higher reinforcing efficiency in the cases of weak geotextiles. It is recommended that the reinforcing efficiency, the allowable settlements and the costs for high strength geotextiles should be balanced in the sustainable design of geotextile-wrapped soil with the help of the proposed analytical solution.

- The analytical solutions for the surcharge pressure on geotextile-wrapped soil under triaxial compression generally agree with the DEM solutions. The agreement is found to be improving increasing geotextile tensile stiffness.

- As the confining pressure increases, both the analytical and DEM solutions give greater ultimate bearing capacities and larger final settlements.

- Though the analytically predicted internal lateral stresses are lower than the DEM simulation results at the beginning, similar maximums of the internal stresses are produced by the analytical and DEM models.

- From the fact that the agreement between the two solutions becomes better with the increase of geotextile tensile stiffness, it is concluded that the assumptions of principal stress ratios still hold for triaxial loading conditions as long as strong geotextiles are considered.

- As the geotextile tensile stiffness increases, the analytical solutions for the volumetric response become less dilative, and larger contraction is predicted compared with the DEM simulation results. Further improvements could be accomplished with unified assumptions on the principal stress ratio and dilation rate for geotextile-wrapped soil under both uniaxial and triaxal loading conditions.

The current analytical solutions are derived specifically for the uniaxial and triaxial compression loading conditions, based on the relevant macroscopic stress-strain responses homogenized from the DEM analyses. The future works will include similar DEM analyses conducted for the loading conditions with predominant shearing between soil–geotextile interface, such as monotonic and cyclic shear. With an advanced understanding of the collective behaviors of geotextile-wrapped soil gained from these DEM analyses, it is envisaged that a unified constitutive law for a single sand-filled geotextile container in general loading conditions will be developed. Once validated with laboratory test data, the continuum-based model could be implemented for the deformable discrete element [Effeindzourou et al., 2016] which solves the stress-strain response of one sand-filled geotextile container. The contact

algorithm and contact laws of the DEM can then efficiently deal with complex interfacial behavior between the deformable discrete elements, which explicitly handles the interactions within the assembly of sand-filled geotextile containers. Benefited from the author's recent development of the coupled FEM/DEM methods Cheng et al. [2016a], the above-mentioned coupling strategy could be easily implemented to solve large-scale engineering problems such as the retaining walls constructed with gravel-filled containers stacked up as the facing and the soft ground reinforced with sand-filled containers.

References

Balaam, N. and Booker, J. (1985). Effect of stone column yield on settlement of rigid foundations in stabilized clay. *International Journal of Numerical Methods in Engineering*, 9(4):331–351. pages 95, 96, 108, 111, 112

Chen, C., McDowell, G., and Thom, N. (2012). Discrete element modelling of cyclic loads of geogrid-reinforced ballast under confined and unconfined conditions. *Geotextiles and Geomembranes*, 35:76–86. pages 98

Cheng, H. and Yamamoto, H. (2015a). Discrete modeling of geotextile-wrapped soil under simple shear. In *PARTICLE-BASED METHODS IV Fundamentals and Applications*, pages 485–496, Barcelona, Spain. pages 98, 102

Cheng, H. and Yamamoto, H. (2015b). Modeling microscopic behavior of geotextile-wrapped soil by discrete element method. In *Proceedings of the 15th Asian Regional Conference on Soil Mechanics and Geotechnical Engineering*, volume 2, pages 2215–2220, Fukuoka. The Japanese Geotechnical Society. pages 98

Cheng, H. and Yamamoto, H. (2016). A multiscale approach for modeling soil-geosynthetic interaction. In *Proceedings of annual research meeting Chugoku Chapter, Architectural Institute of Japan (AIJ)*, volume 39, pages 365–368. Architectural Institute of Japan. pages 98

Cheng, H., Yamamoto, H., Guo, N., and Huang, H. (2016a). A simple multiscale model for granular soils with geosynthetic inclusion. In *Proceedings of 7th International Conference on Discrete Element Methods (DEM7)*, Dalian, China. pages 129

Cheng, H., Yamamoto, H., and Thoeni, K. (2016b). Numerical study on stress states and fabric anisotropies in soilbags using the DEM. *Computers and Geotechnics*, 76:170–183. pages 97, 98, 100, 101, 102, 111, 112, 117

Cheng, H. and Yamamto, H. (2016). Evaluating the performance of geotextile wrapped/layered Soil: a comparative study using the DEM. In *Proceedings of 4th GeoChina International Conference*, Jinan, China. pages 99, 101, 108, 122, 123

Effeindzourou, A., Chareyre, B., Thoeni, K., Giacomini, A., and Kneib, F. (2016). Modelling of deformable structures in the general framework of the discrete element method. *Geotextiles and Geomembranes*, 44(2):143–156. pages 128

Giroud, J. P. and Han, J. (2004a). Design method for geogrid-reinforced unpaved roads. I. development of design method. *Journal of Geotechnical and Geoenvironmental Engineering*, 130(8):775–786. pages 95

Giroud, J. P. and Han, J. (2004b). Design method for geogrid-reinforced unpaved Roads. II. calibration and applications. *Journal of Geotechnical and Geoenvironmental Engineering*, 130(8):787–797. pages 95

Guo, N. and Zhao, J. (2013). The signature of shear-induced anisotropy in granular media. *Computers and Geotechnics*, 47:1–15. pages 97

Guo, W., Chu, J., and Yan, S. (2011). Effect of subgrade soil stiffness on the design of geosynthetic tube. *Geotextiles and Geomembranes*, 29(3):277–284. pages 96

Guo, W., Chu, J., and Yan, S. (2015). Simplified analytical solution for geosynthetic tube resting on deformable foundation soil. *Geotextiles and Geomembranes*, 43(5):432–439. pages 96, 106

Han, J., Bhandari, A., and Wang, F. (2012). DEM analysis of stresses and deformations of geogrid-reinforced embankments over piles. *International Journal of Geomechanics*, 12(4):340–350. pages 98

Hussein, M. and Meguid, M. (2016). A three-dimensional finite element approach for modeling biaxial geogrid with application to geogrid-reinforced soils. *Geotextiles and Geomembranes*, 44(3):295–307. pages 97

Indraratna, B. and Nimbalkar, S. (2013). Stress-strain degradation response of railway ballast stabilized with geosynthetics. *Journal of Geotechnical and Geoenvironmental Engineering*, 139(5):684–700. pages 97

Indraratna, B., Nimbalkar, S., and Rujikiatkamjorn, C. (2014). From theory to practice in track geomechanics – Australian perspective for synthetic inclusions. *Transportation Geotechnics*, 1(4):171–187. pages 105

Kerry Rowe, R. and Skinner, G. D. (2001). Numerical analysis of geosynthetic reinforced retaining wall constructed on a layered soil foundation. *Geotextiles and Geomembranes*, 19(7):387–412. pages 95

Lajevardi, S. H., Dias, D., and Briançon, L. (2015). Experimental studies of the behaviour of geosynthetic wrap around anchorage. *Geosynthetics International*, 22(3):249–256. pages 96, 105

Latha, G. M. and Murthy, V. S. (2007). Effects of reinforcement form on the behavior of geosynthetic reinforced sand. *Geotextiles and Geomembranes*, 25(1):23–32. pages 96, 105

Li, X. and Yu, H.-S. (2013). On the stress–force–fabric relationship for granular materials. *International Journal of Solids and Structures*, 50(9):1285–1302. pages 97

Liu, S., Gao, J., Wang, Y., and Weng, L. (2014). Experimental study on vibration reduction by using soilbags. *Geotextiles and Geomembranes*, 42(1):52–62. pages 96

Liu, S., Lu, Y., Weng, L., and Bai, F. (2015). Field study of treatment for expansive soil/rock channel slope with soilbags. *Geotextiles and Geomembranes*, 43(4):283–292. pages 121

Matsuoka, H. and Liu, S. (2003). New earth reinforcement method by soilbags ("Donow"). *Soils and Foundations*, 43(6)(6):173–188. pages 95

Matsuoka, H. and Liu, S. (2006). *A new earth reinforcement method using soilbags*. Taylor & Francis/Balkema, The Netherlands (2006). pages 96, 117

Matsuoka, H., Liu, S., Hasebe, T., and Shimao, R. (2004). Deformation-strength properties and design methods of soilbag assembly. *Doboku Gakkai Ronbunshu*, 764(III-67):169–181. pages 96

Matsuoka, H., Yamamoto, H., and Nomoto, F. (2010). D·Box method as modern soilbag technology and its local consolidation and vibration reduction effects. *Geosynthetics Engineering Journal*, 25:19–26. pages 96, 121

Muramatsu, D., Bin, Y., and Zhang, F. (2009). Numerical simulation of vibration damping effect of soilbag. *Japanese Geotechnical Journal*, 4(1):71–80. pages 96

Nakai, T. (1989). An isotropic hardening elastoplastic model for sand considering the stress path dependency in three-dimensional stresses. *Soils and foundations*, 29(1):119–137. pages 110, 111

Ngo, N. T., Indraratna, B., Rujikiatkamjorn, C., Biabani, M. M., and Mahdi Biabani, M. (2015). Experimental and discrete element modeling of geocell-stabilized subballast subjected to cyclic loading. *Journal of Geotechnical and Geoenvironmental Engineering*, page 04015100. pages 98

O'Sullivan, C. (2011). *Particulate discrete element modelling: a geomechanics perspective*. Taylor & Francis, Hoboken, NJ. pages 103

Palmeira, E. M. (2009). Soil–geosynthetic interaction: Modelling and analysis. *Geotextiles and Geomembranes*, 27(5):368–390. pages 105

Pulko, B., Majes, B., and Logar, J. (2011). Geosynthetic-encased stone columns: Analytical calculation model. *Geotextiles and Geomembranes*, 29(1):29–39. pages 95, 96, 108, 111

Šmilauer, V., Chareyre, B., Duriez, J., Eulitz, A., Gladky, A., Guo, N., Jakob, C., and Kozicki, J. (2015). Using and Programming. In Project, T. Y., editor, *Yade Documentation*. 2 edition. pages 101

Sun, D., Huang, W., Sheng, D., and Yamamoto, H. (2007). An elastoplastic model for granular materials exhibiting particle crushing. *Key Eng. Mater.*, 340-341:1273–1278. pages 104

Tafreshi, S. M. and Dawson, A. (2010). Comparison of bearing capacity of a strip footing on sand with geocell and with planar forms of geotextile reinforcement. *Geotextiles and Geomembranes*, 28(1):72–84. pages 96, 105

Tatsuoka, F., Tateyama, M., Mohri, Y., and Matsushima, K. (2007). Remedial treatment of soil structures using geosynthetic-reinforcing technology. *Geotextiles and Geomembranes*, 25(4-5):204–220. pages 95, 121

Thoeni, K., Lambert, C., Giacomini, A., and Sloan, S. W. (2013). Discrete modelling of hexagonal wire meshes with a stochastically distorted contact model. *Computers and Geotechnics*, 49:158–169. pages 98, 101

Thornton, C., Cummins, S. J., and Cleary, P. W. (2011). An investigation of the comparative behaviour of alternative contact force models during elastic collisions. *Powder Technology*, 210(3):189–197. pages 99

Wang, L.-J., Liu, S.-H., and Zhou, B. (2015). Experimental study on the inclusion of soilbags in retaining walls constructed in expansive soils. *Geotextiles and Geomembranes*, 43(1):89–96. pages 95

Wang, Z., Jacobs, F., and Ziegler, M. (2016). Experimental and DEM investigation of geogrid–soil interaction under pullout loads. *Geotextiles and Geomembranes*, 44(3):230–246. pages 98

Wu, C.-S. and Hong, Y.-S. (2014). A simplified approach for evaluating the bearing performance of encased granular columns. *Geotextiles and Geomembranes*, 42(4):339–347. pages 95, 96

Wu, Y., Yamamoto, H., and Yao, Y. (2013). Numerical study on bearing behavior of pile considering sand particle crushing. *Geomechanics and Engineering*, 5(3):241–261. pages 109, 110

Xu, Y., Huang, J., Du, Y., and Sun, D. (2008). Earth reinforcement using soilbags. *Geotextiles and Geomembranes*, 26(3):279–289. pages 96

Yao, Y.-p., Yamamoto, H., and Wang, N.-D. (2008). Constitutive model considering sand crushing. *Soils and foundations*, 48(4):603–608. pages 109, 110

Yoo, C. and Kim, S. (2008). Performance of a two-tier geosynthetic reinforced segmental retaining wall under a surcharge load: Full-scale load test and 3D finite element analysis. *Geotextiles and Geomembranes*, 26(6):460–472. pages 97

Zhao, J. and Guo, N. (2013). Unique critical state characteristics in granular media considering fabric anisotropy. *Géotechnique*, 8(8):695–704. pages 97

Chapter 6

A Simple Multiscale Model for Granular Soils with Geosynthetic Inclusion

6.1 Introduction

Geosynthetics are widely applied as a sustainable reinforcement material for geotechnical structures. To date, laboratory tests remain as the primary approach to study the behavior of geosynthetic-reinforced soil (GRS). Scaled model tests of geosynthetic-reinforced geostructures (e.g. road ballast and embankments) and elementary tests of GRS in designed loading conditions (e.g. pull-out and biaxial/triaxial compression) are usually conducted to facilitate the constitutive modeling of GRS. Some elastoplastic models of soil are modified to describe the stress-strain behavior of GRS. However, these models are highly phenomenological, and thus can provide neither a complete description of mechanical behavior nor insights into reinforcement mechanism in conventional finite element method (FEM) analyses. The discrete element method (DEM) is naturally suitable for heterogeneous and discontinuous materials like GRS. A realistic geometrical representation of geosynthetics can be done with bonded particles and chained deformable DEs [Bourrier et al., 2013; Effeindzourou et al., 2016]. With the tensile behavior of geosynthetics and the interfacial friction properly calibrated, a discrete GRS model can reproduce a variety of fundamental behaviors such as confinement,

interlocking, fiber breakage and fabric rupture, among others. Furthermore, unlike the FEM, discrete modeling of GRS in different forms, e.g. planar sheet, radial encasement, closed container, can be conveniently handled.

Because granular structures and mechanics are rigorously considered in DEM, it takes extremely high computational cost to solve large-scale boundary value problems (BVPs). On the contrary, FEM can handle BVPs efficiently, but the continuum-based constitutive models that are derived from elementary tests of GRS cannot be adapted to the GRS in diverse forms and loading conditions. To solve large-scale BVPs with complex material behavior, the Hierarchical Multiscale (HM) approach which takes the advantages of both FEM and DEM seems to be a promising tool [Guo and Zhao, 2014, 2016a,b; Guo et al., 2016]. Because the constitutive relations and stresses are numerically acquired from contact mechanics of discrete particles, non-coaxially, anisotropy and non-associated flow are naturally obtained, which makes this approach well suited for modeling GRS that usually undergoes complex stress history and localized deformation.

The so-called Concurrent Multiscale (CM) approach takes a different modeling strategy. DEM is exclusively used for the domains subjected to large deformation or located at interfaces, whereas FEM is considered for the homogeneous part. Regardless of the bridging schemes adopted, the FE and DE domains coexist and are modeled separately, except for a small overlap of volume/surface where the kinematics and forces are shared. Applications of the CM approach can be found in the modeling of near-tunnel soil loss, pile penetration and soil–geosynthetic interaction, etc.

This chapter presents a multiscale model for GRS, taking advantage of recent breakthroughs of multiscale approaches. The main objective is to adapt the existing multiscale frameworks to soil–geosynthetic interaction problems, such that the material behaviors are self-adaptive to complex loading history and geometrical configurations of GRS. In the meantime, the computational efficiency is preserved. Section 6.2 presents the formulations and the FEM/DEM coupling strategies. Section 6.3 introduces two numerical examples of soil–geosynthetic interaction in which different mesh density, boundary and loading conditions are

considered. Section 6.4 and 6.5 discuss the multiscale responses, showcasing the predictive capacity of the multiscale model.

6.2 Formulation and coupling strategy

The current multiscale model is developed within the HM framework proposed by Guo [2014]. The macroscopic responses of a soil domain is solved as a BVP by FEM, while the Representative Volume Elements (RVEs) that consist of circular particles return stress field at the Gauss points in a hierarchically homogenized manner. The interactions between soil and geosynthetic inclusion are modeled concurrently with DEM, by which the force boundary condition of the BVP is returned. After solving the kinematics within the soil domain by numerical integration, each RVE is loaded with the macro deformation and rotation at the specific Gauss point for the material response in the next time step. Meanwhile, the boundary velocity field is collected to advance the kinematics of the geosynthetic inclusion and update the boundary forces in the concurrent DE domain. This multiscale model is implemented with Escript [Gross, 2011] and Yade [Šmilauer et al., 2015].

The motion of a continuous domain is governed by

$$\boldsymbol{M}\ddot{\boldsymbol{u}} + \boldsymbol{f}^{int} - \boldsymbol{f}^{ext} = 0 \tag{6.1}$$

where $\boldsymbol{M}$ is the consistent mass matrix, $\ddot{\boldsymbol{u}}$ is the FEM nodal acceleration vector, and $\boldsymbol{f}^{int}$ and $\boldsymbol{f}^{ext}$ are the internal and external force vectors computed from the Cauchy stress $\boldsymbol{\sigma}$ and the applied boundary surface traction $\bar{\boldsymbol{t}}$. The kinematics of rigid particles are governed by Newton's equations of motion. Once an overlap between two adjoining particles are detected, the contact forces are computed using a specific contact law. In the present work a linear force-displacement law is used in conjunction with the Mohr-Coulomb plastic criterion [Cundall and Strack, 1979].

The solutions of the governing equations in FEM and DEM are approximated in the explicit central difference time integration scheme. For numerical stability, the time steps are limited

considering the maximum eigenvalues λ_m, ($\Delta t_{FE} < 2/\sqrt{\lambda_m}$). To lower the computational cost, a lumped diagonal mass matrix is applied. A viscous damping coefficient $c = 0.2$ is considered in the FEs at the macro scale, while background damping is applied in the RVEs and the concurrent DE domain to attain stable micro responses. With $\ddot{\boldsymbol{u}}$ solved in Eq. 6.1, the velocity $\dot{\boldsymbol{u}}$ and displacement $\boldsymbol{u}$ can be readily advanced by Eqs. 6.2 and 6.3.

$$\dot{\boldsymbol{u}}^{(n+1/2)} = \frac{2 - c\Delta t_{FE}}{2 + c\Delta t_{FE}} \dot{\boldsymbol{u}}^{(n-1/2)} + \frac{2\Delta t_{FE}}{2 + c\Delta t_{FE}} \ddot{\boldsymbol{u}}^{(n)} \tag{6.2}$$

$$\boldsymbol{u}^{(n+1)} = \boldsymbol{u}^{(n)} + \Delta t_{FE} \dot{\boldsymbol{u}}^{(n+1/2)} \tag{6.3}$$

The present work seeks the transient responses of the multiscale GRS model. Because $\boldsymbol{u}$ is calculated explicitly, only $\boldsymbol{\sigma}$ and $\bar{\boldsymbol{t}}$ are needed for the FE solver. The Love-Webber formula homogenizes $\boldsymbol{\sigma}$ from the contact forces and branches within a granular material. Though initially derived for static contacts, the formula still holds when dynamics are involved as long as circular/spherical particles are concerned [Nicot et al., 2013; Smith and Wensrich, 2014]. In such cases, the symmetric part of the Love-Webber product is all that is needed for $\boldsymbol{\sigma}$. Once $\boldsymbol{u}^{(n+1)}$ is predicted, the displacement gradient $\nabla \boldsymbol{u}$ at the Gauss points is enforced onto the RVEs. Note that $\nabla \boldsymbol{u}$ includes a skew-symmetric part. In addition to strain, it applies a coarse scale rotation on the RVEs to empower large deformation in the continuous domain.

The geosynthetic inclusion constructed with the discrete bar elements (DBEs) are initially aligned with the boundary interface DBEs. The velocities of the interface nodes are kept in accordance with the FE boundary nodes to mobilize and strain the geosynthetic DBEs. A set of tensile/compressive, shear and rolling springs are mounted at the DE nodes to govern the internal behavior of the DBEs. Where a potential contact is identified between an interface and a geosynthetic DBE a pair of virtual disks will be introduced within each DBE, so that the same contact laws for interactions of circular particles can be reused therein. The kinematics of each disk are interpolated linearly from the nodal values. The nodal forces are obtained in a similar manner and then applied to the FE solver. After the FE solver predicts new positions

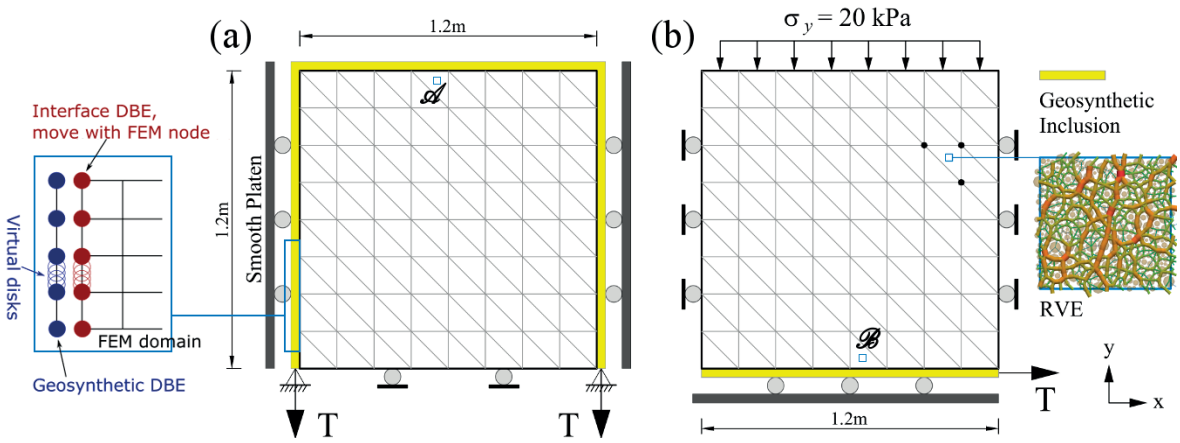

Fig. 6.1 Numerical examples of soil–geosynthetic interactions: (a) shape-forming and (b) pull-out tests.

for the boundary nodes, the same displacement increments are prescribed to the interface DBE nodes to ensure geometrical compatibility. Taking into account the time step Δt_{DE} in the concurrent DE domain ($\Delta t_{FE} = n\Delta t_{DE}$), the new velocity boundary can be readily obtained.

The hierarchical multiscale approach, which is applied for modeling the granular soil domain, is computationally efficient compared with the paralleled pure DEM approach, because the multiscale simulations do not need to partition the domain and to handle the interfacial communication among the sub-domains as required in the parallelization of pure DEM simulations. In the case of pure DEM simulations, the parallelization requires the particles at the interfaces of neighboring subdomains to be tracked and the relevant kinematics and contact forces to be communicated between the adjacent subdomains. In the multiscale simulations, however, the deformation is assigned hierarchically from the macro scale FEM solver to local RVEs, which avoids a large computational cost for communicating information among subdomains in the pure DEM simulations. In order to reasonably allocate computational resources for the computations of the soil domain and soil–geosynthetic interaction (the former is much slower than the latter), the DEM simulation of geosynthetic-boundary interactions is designed to run simultaneously alongside the simulations of the local RVEs in the soil domain. To this end, the parallelization of DEM simulations is implemented asynchronously, so that one simulation can be executed before the completion of another.

6.3 Numerical Examples of Soil-geosynthetic Interaction

In this section, two numerical examples are presented for examining the predicative capacity of the current multiscale GRS model. Because forces and kinematics are linearly interpolated within the DBEs, meshes constructed with high-order FE elements (e.g., eight-node quadrilateral element) are very likely to result in the boundary kinematics inconsistent with the movement of geosynthetic inclusion, i.e. gaps between the DE geosynthetic inclusion and the soil domain at the top boundary in the shape-forming simulations. Therefore, in both examples, the soil domain is discretized using linear triangle elements. Each triangle is assigned with one RVE at the Gauss point. The RVE contains circular particles with radii of 3, 5, and 10 mm (ratio of 4:13:3), as shown in Fig. 1(b). The process of selecting RVEs in Guo and Zhao [2014] is followed to obtain an isotropic particle assembly, except that a negligible level of confining pressure is applied instead ($p_0 = 10$ kPa). Because the macroscopic responses should be compared with the experimental responses of aluminum rods with the same particle size distribution, the micro parameters are derived from the elastic solution of two contacting cylinders [Matsuoka and Yamamoto, 1994].

Table 6.1 gives the micro-parameters for interactions within the RVEs, as well as the parameters that govern the internal and contact behavior of the DBEs. The Poisson's ratio υ_c and friction angle φ of a DBE itself introduces shear stiffness and shear strength for the beam-like DBE, and thus are set to zero for modeling a flexible geotextile. The Young's modulus E_c of the geosynthetic DBE was obtained from the results of tensile tests on a polypropylene geotextile, whereas the friction angle that limits the tangential force between the interface and geosynthetic DBEs was determined from shear box test data [Cheng et al., 2016]. In the shape-forming example, the friction between soil (interface) and geosynthetic is excluded so that confinement is the only contributor to the geosynthetic reinforcement.

Fig. 6.1a and b illustrate the boundary conditions and the layouts of the geosynthetic inclusions in the shape-forming and pull-out multiscale simulations. In the latter case, the RVEs are loaded to a vertical stress of 20 kPa under K_0 condition before imported to the multiscale simulation. The interest of the negligible initial stress level in the shape-forming

Table 6.1 Parameters for interactions within the RVE and internal/external behavior of DBEs.

Element/contact type	Density (kg/m^3)	E_c (MPa)	υ_c	φ	Damping ratio	Tensile stiffness σ_T^l (MPa)
RVE	2650	750	0.016	16	0.2	n/a
Interface DBE	2650	0	0	0	0.4	Inf.
Geosynthetic DBE	444	2.84	0	0	0.4	0.41
Interface-geosynthetic	n/a	2.84	0.33	21	0.4	0.41

example is to have a complete evolution of multiscale responses that depend entirely on the geosynthetic inclusion. In what follows, the dependence on mesh density is examined by three different meshes, i.e. coarse, medium and fine (72, 128, and 200 elements), with the pulling speed v= 1cm/s. The effect of pulling speed is then checked using the medium mesh (v = 1, 0.5, and 0.25 cm/s), followed by the multiscale analyses of both examples.

6.4 Global responses

Despite the difference in pulling speed and mesh density, the multiscale simulations of all shape-forming cases produce similar global responses of σ_y at the boundary, as shown in Fig. 6.2a. It is noted that the finer meshes slightly postpone the onset of hardening, whereas the influence of pulling speed is marginal. On the contrary, the pulling speed in the pull-out cases is found to be proportional to the initial rate of increase for the global friction angle at the boundary. Further increase of mesh resolution appears to have no effect on the rate of increase. To acquire a cross-scale knowledge of soil–geosynthetic interaction, the global and local responses produced with the medium mesh and the medium pulling speed are presented below.

Fig. 6.3 and 6.4 give respectively the distribution of stress, strain and rotation at the final state of the shape-forming and the pull-out simulations. In the shape-forming case, both the mean stress p and u distribute asymmetrically across the domain that is not in contact with the geosynthetic inclusion. Close to the inclusion at the top boundary, rotation $\bar{\theta}$ also asymmetrically distributed, with u and shear strain ε_q much greater than the rest of the domain. The horizontal pullout of geosynthetic inclusion results in large deviatoric stress q in the

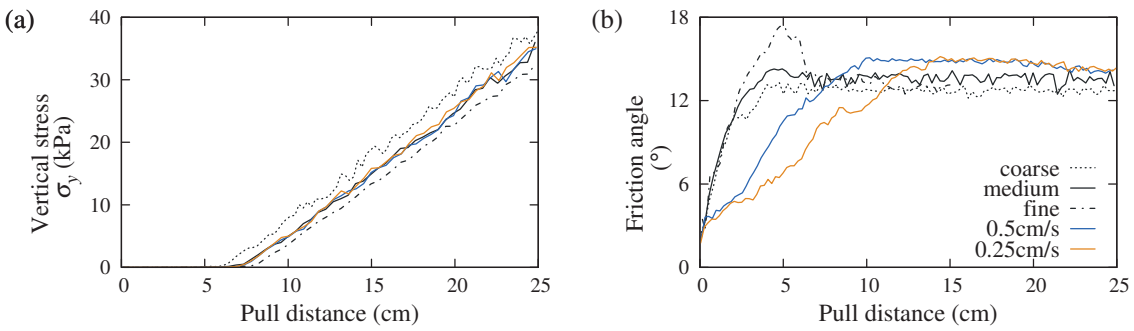

Fig. 6.2 Global response of vertical stress at the bottom in (a) shape-forming and (b) pull-out examples.

vicinity, the intensity of which coincides with the magnitude of straining (σ_T/σ_T^l) within the inclusion. As the pullout proceeds, vortex-like pattern is observed similar to the lid-driven cavity flow: soil settling down on the left and heaving on the right. This is because the horizontal shear exerted by the inclusion causes the dilation of soil on the pulling direction. The rotation field further confirms the vortex-like pattern abovementioned.

6.5 Local responses

The local responses at Gauss point $\mathscr{A}$ and $\mathscr{B}$ located close to the geosynthetic inclusion as shown in Fig. 6.1 are investigated. Fig. 6.5a–c plot the evolutions of q/p, volumetric strain ε_v and fabric anisotropy F_a [Guo and Zhao, 2016b] versus deviatoric strain ε_q at point $\mathscr{A}$ in the shape-forming simulation. As would be expected, the volume of this RVE expands initially when the confinement from the inclusion is insufficient to overcome the soil pushed

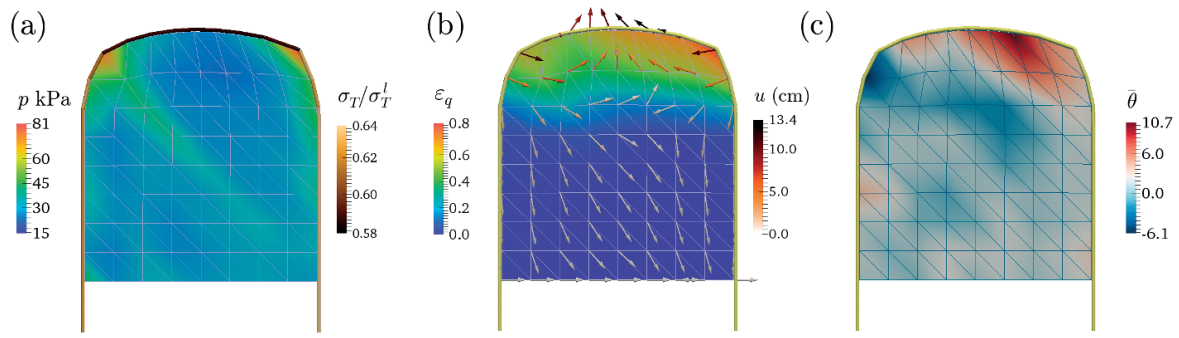

Fig. 6.3 Global responses of (a) stress, (b) strain and (c) rotation in the shape-forming simulation.

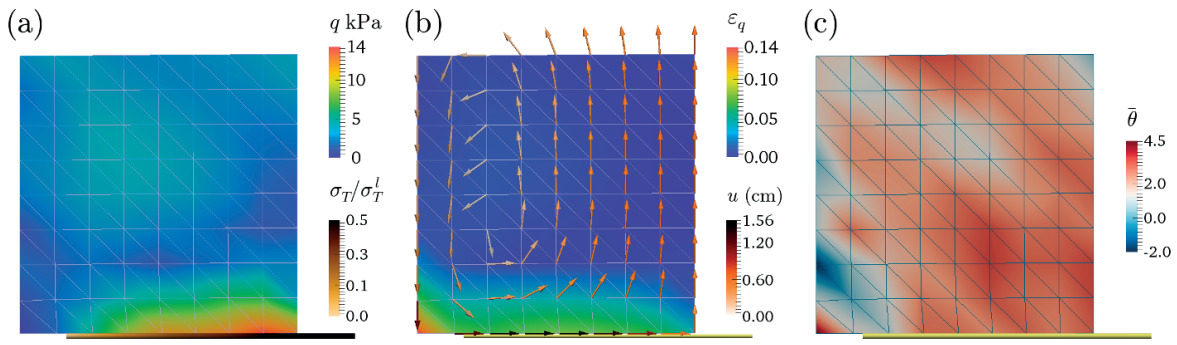

Fig. 6.4 Global responses of (a) stress, (b) strain and (c) rotation in the pull-out simulation.

upward from below. The stress state at point $\mathscr{A}$ evolves from the failure state, which can be understood from the large initial values of q/p and the stress path in Fig. 6.5b. After the onset of hardening at about 7 cm pull distance, the RVE starts to contract, while both q and p increase with reducing q/p (see 6.5a). Similarly, F_a gradually drops to almost zero, which suggests the geosynthetic confinement becoming more isotropic as the top boundary being curved.

6.6a–c show the local responses at point $\mathscr{B}$ in the pull-out simulation. As discussed before, dilation occurs in the elements that are sheared directly by the geosynthetic inclusion. The local response of ε_v at point $\mathscr{B}$ further confirms this global behavior. The constitutive behavior herein is similar to that of medium dense sand in undrained triaxial tests as shown in Fig. 6.6a and b, except the volume dilates marginally after passing its initial stagnated stage. Both q and F_a increase from zero to their maximums as shown in Fig. 6.6a and c. After reaching the maximums, the local states of stress, strain and fabric at this point cease to change. This could be contributed to the shear resistance of the RVE at point $\mathscr{B}$ reaching its full strength, which means a steady state is attained for point $\mathscr{B}$ and the inclusion can be pulled out without any effects on the local mechanical and geometrical states.

6.6 Conclusions

A multiscale model is presented in the hierarchical multiscale framework for studying soil–geosynthetic interaction problems. With the geosynthetic inclusion considered concurrently, both the internal and external forces can be given by local DEM solvers. FEM then solves

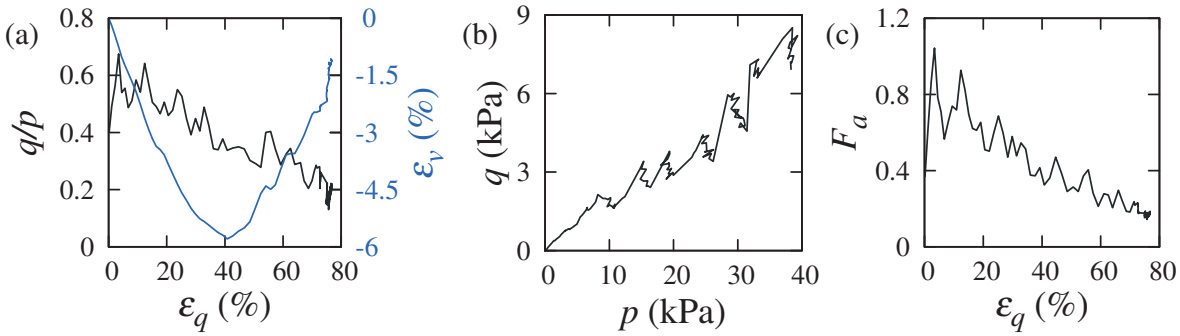

Fig. 6.5 (a) Local responses of deviatoric stress and volumetric strain, (b) stress path, and (c) fabric anisotropy at the Gauss point $\mathscr{A}$ in the shape-forming simulation.

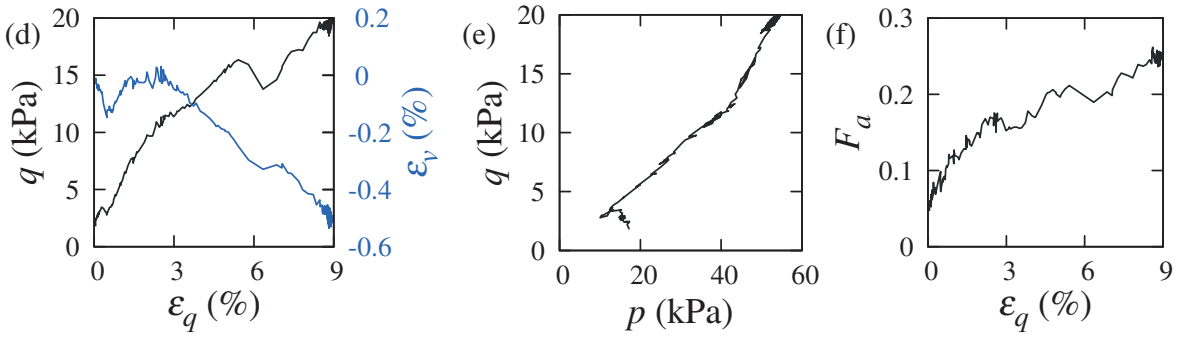

Fig. 6.6 (a) Local responses of deviatoric stress and volumetric strain, (b) stress path, and (c) fabric anisotropy at the Gauss point $\mathscr{B}$ in the pull-out simulation.

displacement field in an explicit time integration scheme. Two simple numerical examples are demonstrated to examine the predicative capacity of the multiscale model in different loading and boundary conditions. The initial rate of increase for vertical stress at the boundary in the pull-out case is found sensitive to the pulling speed. The shape-forming simulation shows increasing stress level and decreasing anisotropy at the local point near the top boundary where shear strain is bigger than the rest of the domain. In the pull-out simulation, vortex-like displacement field is observed with the origin close to the left end of the inclusion. Such pattern is further confirmed by the dilative volumetric response at the local Gauss point above the inclusion. The RVE therein behaves similarly to medium dense soil in undrained triaxial compression condition.

References

Bourrier, F., Kneib, F., Chareyre, B., and Fourcaud, T. (2013). Discrete modeling of granular soils reinforcement by plant roots. *Ecological Engineering*, 61:646–657. pages 136

Cheng, H., Yamamoto, H., and Thoeni, K. (2016). Numerical study on stress states and fabric anisotropies in soilbags using the DEM. *Computers and Geotechnics*, 76:170–183. pages 141

Cundall, P. A. and Strack, O. D. L. (1979). A discrete numerical model for granular assemblies. *Géotechnique*, 29(1):47–65. pages 138

Effeindzourou, A., Chareyre, B., Thoeni, K., Giacomini, A., and Kneib, F. (2016). Modelling of deformable structures in the general framework of the discrete element method. *Geotextiles and Geomembranes*, 44(2):143–156. pages 136

Gross, L. (2011). esys-Escript user ' s guide : solving partial differential equations with Escript and Finley. *Manual*, 1:144. pages 138

Guo, N. (2014). *Multiscale characterization of the shear behavior of granulr media*. PhD thesis, Hong Kong University of Science and Technology. pages 138

Guo, N. and Zhao, J. (2014). A coupled FEM/DEM approach for hierarchical multiscale modelling of granular media. *International Journal for Numerical Methods in Engineering*, 99(11):789–818. pages 137, 141

Guo, N. and Zhao, J. (2016a). 3D multiscale modeling of strain localization in granular media. *Computers and Geotechnics*. pages 137

Guo, N. and Zhao, J. (2016b). Multiscale insights into classical geomechanics problems. *International Journal for Numerical and Analytical Methods in Geomechanics*, 40(3):367–390. pages 137, 143

Guo, N., Zhao, J., and Sun, W. (2016). Multiscale analysis of shear failure of thick-walled hollow cylinder in dry sand. *Géotechnique Letters*, 6:1–18. pages 137

Matsuoka, H. and Yamamoto, S. (1994). A microscopic study on shear mechanism of granular materials by DEM. *Doboku Gakkai Ronbunshu*, 487:167–175. pages 141

Nicot, F., Hadda, N., Guessasma, M., Fortin, J., and Millet, O. (2013). On the definition of the stress tensor in granular media. *International Journal of Solids and Structures*, 50(14-15):2508–2517. pages 139

Šmilauer, V., Chareyre, B., Duriez, J., Eulitz, A., Gladky, A., Guo, N., Jakob, C., and Kozicki, J. (2015). Using and Programming. In Project, T. Y., editor, *Yade Documentation*. 2 edition. pages 138

Smith, A. and Wensrich, C. (2014). The effects of particle dynamics on the calculation of bulk stress in granular media. *International Journal of Solids and Structures*, 51(25-26):4414–4418. pages 139

Chapter 7

Conclusions

This thesis explores the multiscale mechanics of geosynthetic-reinforced soils that come in various forms with two alternative modeling approaches. To obtain qualitative agreement between numerical predictions and experimental results, the macroscopic response of the DEM model of Toyoura sand is calibrated with a data assimilation technique, i.e. the particle filter (Chapter 2). Chapter 3 investigates the geosynthetic-wrapped granular soil in unconfined compression and simple shear through pure DEM modeling. Linear stress paths and decreasing fabric anisotropies are observed during both loading courses, which demonstrates greater and more isotropic confinement with the increase of shear deformation in the wrapped soil. The global and local stress paths are found to be similar in both geotextile-wrapped and -layered granular soils subjected to triaxial compression, though the wrapped soil can sustain greater load than the layered soil (Chapter 4). Chapter 5 presents an analytical model of geotextile-wrapped soil, based on the assumptions of stress path and stress-dilatancy relationship developed from the new insights obtained in Chapter 3 and 4. In Chapter 6, a multiscale framework for modeling general soil-geosynthetic interaction problems is proposed by integrating the concurrent multiscale approach within the hierarchical multiscale framework.

The main contributions and findings on multiscale understanding and modeling of geosynthetic-reinforced soils are summarized as follows:

Parameter identification A sequential data assimilation technique, i.e. the particle filter, is applied in conjunction with Monte Carlo simulation to identify contact law parameters for DEM models of granular soil. True values for the micro parameters of Cundall's linear and Hertz-Mindlin contact laws are identified with high accuracy compared with experimental observation. Though the identified values for the contact parameters vary with respect to confining stresses, the identification process is successful and the weight-averaged parameters converge to constant values eventually. The numbers of particles are found to have marginal effect on the identified values, which suggests that granular behavior depends largely on the micrcostructures of a granular packing instead of particle sizes. The relationships between micro-macro parameters are identified: the variation of the micro parameters with respect to confining stress is similar to that of the macro parameters.

Discrete element modeling of geosynthetic-wrapped granular soil A novel DEM model of geosynthetic-wrapped granular soil is presented. The wrapped granular soil is generated in a 3D–assembling–filtering–expanding process. This DEM model is validated with experimental responses of sand-filled geotextile containers subjected to unconfined compression and simple shear. Under unconfined compression, both global and local stress paths are linear at the pre-failure state with greater p and q values in the middle of the wrapped soil. At the post-failure stage, the lateral confining stress remains nearly constant, which leads to a gentle decline in the bearing capacity. The soil–geotextile interfacial shear stresses are found to be higher on the lateral sides than on the top and bottom sides, but each of them is greatly below the maximum for mobilizing the interface. The global stress path in simple shear approaches the critical state line of the wrapped soil first and then heads away with lower q and greater p. Partial loading–reloading paths are experienced in the middle of the wrapped soil, which explains the high damping of the soilbag. As the vertical dead load rises, the slope of the critical state line decreases, indicating a better control on the dilatancy of the wrapped soil. The soilbag constrains dilatancy differently depending on the tensile stiffness of the geotextile. For the soil wrapped by the strong geotextile, the numerical predictions show that the critical state is never reached during compression and the volume does not dilate until the geotextile starts

to fail. For the weak geotextile, the soil reaches the critical state with sufficiently developed shear bands and dilatancy. However, the stress path progresses along the critical state line due to the sustained confinement on the wrapped soil. The decreasing mechanical fabric anisotropies in either loading course suggest that confinement is the primary mechanism of the soilbag reinforcement method. A stronger geotextile enables more isotropic confinement. The results on interfacial shear indicate that the interlocking effect takes a secondary role in prolonging the effective lateral confinement, particularly during the post-failure stage of compression. Under simple shear, the confinement of the wrapped soil grows increasingly isotropic with greater shear deformation and a higher level of vertical dead load.

Relative performance of geotextile-wrapped and -layered granular soil A comparative study on geotextile-wrapped and -layered soils is conducted using the discrete element method. The geotextile-layered soil is derived from the validated DEM model of geotextile-wrapped soil. Both models are loaded in triaxial compression condition. The geotextile-wrapped soil gives greater stress response than the layered soil in the reinforced and global domains. The horizontal stress residue in the former is also larger than the vertical one in the latter. Global volumetric strain changes similarly in two cases, with the layered soil contracted more than the other. The simulations produce linear stress paths in the global and local domains with the same slope, regardless of the reinforcement forms, i.e. container and sheet. Nevertheless, stress is concentrated more in the center of the reinforced zone in the case of the layered soil. With the increase of the geotextile tensile stiffness, both the slopes of the global and local stress paths reduce increasingly. The simulation shows that the reinforced zone is contracted more in the case of the wrapped soil than the layered soil. After 20% axial compression, the void ratio in the reinforced zone of the layered case is 1.5 times that of the global void ratio, causing severe strain localization. The wrapped soil, however, has similar void ratio across the whole domain, with less localized strain in the reinforced zone.

Analytical modeling of geotextile-wrapped soil A new analytical solution for geotextile-wrapped soil is developed with the assumptions facilitated by the findings obtained from the

DEM modeling of a sand-filled container. The analytical model considers the tensile behavior of geotextile to be purely elastic, and the wrapped soil as a Mohr-Coulomb elastoplastic solid with evolving principal stress ratio and dilation rate. Because the material parameters need to be updated during compression loading, the analytical solution for geotextile-wrapped soil is solved numerically. By imposing an empirical power-law relation between the geotextile tensile stiffness and the Young's modulus of the wrapped soil, good agreement is obtained between the analytical and DEM solutions for geotextile-wrapped soil in uniaxial loading condition. The slopes of the straight lines that display the linear relationships between the surcharge pressures and the tensile stresses tend to reduce towards a constant value with the increase of geotextile tensile stiffness. This trend suggests higher reinforcing efficiency in the cases of weak geotextiles. It is recommended that reinforcing efficiency, allowable settlement and the cost for high strength geotextiles should be balanced in the sustainable design of geotextile-wrapped soil with the help of the proposed analytical solution. The predictive capacity of the proposed analytical solution is further examined in triaxial compression conditions, considering different confining pressures and geotextile tensile stiffnesses. Though the analytically predicted internal lateral stresses are lower than the DEM simulation results initially, similar maximums of the internal stresses are produced by the analytical and DEM models. The agreement between the two solutions becomes better with the rise of geotextile tensile stiffness, which suggests that the assumption of principal stress ratio still holds for triaxial loading conditions as long as strong geotextiles are concerned. As the geotextile tensile stiffness increases, the analytical solutions for the volumetric response become less dilative, and larger contraction is predicted compared with the DEM simulation results. Further improvements could be accomplished with unified assumptions on the principal stress ratio and dilation rate for geotextile-wrapped soil under both uniaxial and triaxal loading conditions.

Multiscale characterization of granular soils with geosynthetic inclusion A multiscale model is presented in the hierarchical multiscale framework for studying soil–geosynthetic interaction problems. With the geosynthetic inclusion modeled concurrently, the internal

and external forces are respectively upscaled from contact forces within the local DEM particle packing and soil–geosynthetic interaction. Two simple numerical examples, i.e. shape-forming and pull-out tests, are demonstrated to examine the predicative capacity of the multiscale model in different loading and boundary conditions. The initial rate of increase for vertical stress at the boundary in the pull-out case is found sensitive to the pulling speed, whereas the vertical stress in the shape-forming case rises independently of the pulling speed. The shape-forming simulation shows increasing stress level and decreasing anisotropy at the local Gauss point near the top boundary where shear strain is bigger than the rest of the domain. In the pull-out simulation, vortex-like displacement field is observed with the origin close to the left end of the inclusion. Such pattern is further confirmed by the dilative volumetric response at the local Gauss point that lies above the inclusion. The representative volume element therein behaves similarly to medium dense soil in undrained triaxial compression condition.